Dissertation zur Erlangung des Doktorgrades
der Fakultät für Chemie und Pharmazie
der Ludwig-Maximilians-Universität München

Quantitative Solid State Nuclear Magnetic Resonance Methods For Inorganic Materials

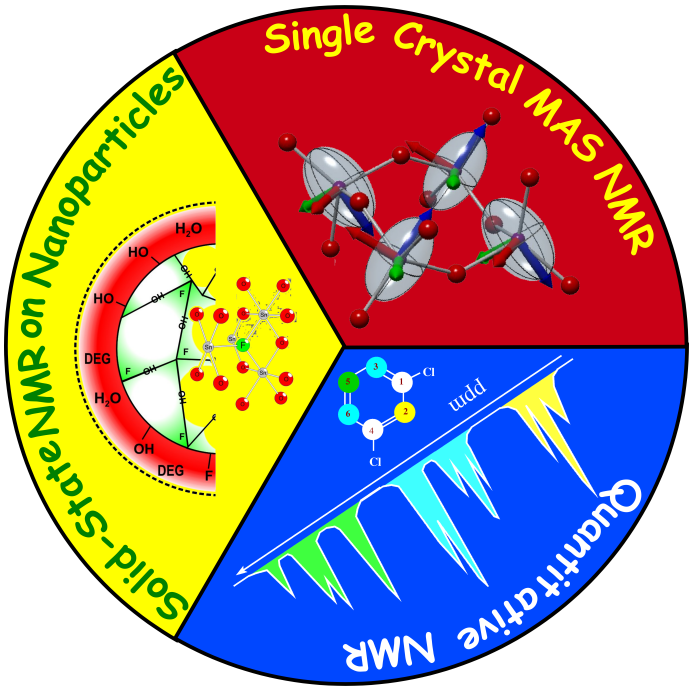

Yamini Sudhakar Avadhut
aus
Nagpur, Indien

2012

Dissertation zur Erlangung des Doktorgrades
der Fakultät für Chemie und Pharmazie
der Ludwig-Maximilians-Universität München

Quantitative Solid State Nuclear Magnetic Resonance Methods For Inorganic Materials

Yamini Sudhakar Avadhut
aus
Nagpur, Indien

2012

Erklärung:

Diese Dissertation wurde im Sinne von § 7 der Promotionsordnung vom 28. November 2011 von Herrn Dr. Jörn Schmedt auf der Günne betreut.

Eidesstattliche Versicherung:

Diese Dissertation wurde eigenständig und ohne unerlaubte Hilfe erarbeitet.

München, den

_____

Yamini Sudhakar Avadhut

Dissertation eingereicht am

1. Gutachter	Dr. Jörn Schmedt auf der Günne
2. Gutachter	Prof. Dr. Leo van Wüllen
Mündliche Prüfung am	26.03.2012

Dedicated to my parents
Mr. Sudhakar Avadhut
&
Mrs. Sushila Avadhut

Acknowledgment

My Ph.D. years at the "Ludwig-Maximilians-Universität" and this thesis has had mentorship from numerous outstanding individuals. My heartfelt gratitude and thanks go to these individuals and without their help, this thesis would not have seen the successful end.

First of all, I would like to express my gratitude to Dr. Jörn Schmedt auf der Günne for giving me the opportunity to work in his research group. I am grateful for his encouragement, guidance and support from the initial to the final level which enabled me to develop an understanding of the subject. His valuable advises guided me towards fruitful outcome during my Ph.D. studies.

I am grateful to Prof. Dr. Wolfgang Schnick for being available as examiner in my *viva-voce*, and providing me all necessary facilities and equipment in the department to carry out my experiments. I express special gratitude to Prof. Wolfgang Schnick for kindly arranging my funding in the last phase of my thesis.

I would like to thank Prof. Dr. Leo van Wüllen from the Institut für Physik, Universität Augsburg for being my second referee.

I am thankful to Prof. Dr. Konstantin Karaghiosoff, Prof. Dr. Dirk Johrendt and Prof. Dr. Christina Scheu for being available as examiners in my *viva-voce*.

I gratefully acknowledge Prof. Dr. Claus Feldmann, Dr. Elin Hammarberg and Dr. Marcus Roming from the Institute for Inorganic Chemistry, Karlsruhe Institute of Technology, for providing all nanoparticles samples and introducing me to the nanoparticle world.

I would like to thank Dr. Johannes Weber for numerous inspiring discussions about quantum chemistry, our friend and foe, "the computer", and for teaching me Linux secrets. His deep understanding of the subject, valuable suggestions and constructive discussions, at different stages of my Ph.D. improved the quality of this thesis.

I am much indebted to Prof. Dr. Oliver Michael Oeckler for his great help concerning all kinds of crystallography questions. A special thanks goes to Dr. Denis Schneider who allowed me to do some experiments at Bruker, Karlsruhe.

A special thanks to our campus mechanical workshop, without them it would not have been possible to finish my hardware task.

I have had great fun as well as support from all members of our small NMR group:

Dr. Johannes Weber and Dr. Jörn Schmedt auf der Günne - for helping me in the beginning of my studies both with the NMR and computer; Christian Minke- for his help with NMR spectrometer and being motivation to become a punctual personality; Vinicius Ribeiro Celinski (Vicoooool/Vico/Voco...)- for many things as well as for Chemistry; Martin Mangstl (Morton)- for always helping me with Chemistry related problems; Dr. Sabarinathan Venkatachalam- helping me with all kind of problems. Discussions about NMR with each and every person in the group have been very useful and educating for me. -thank you!

I am grateful to all people who are proofreading my thesis and giving me valuable suggestions: especially, Dr. Jörn Schmedt auf der Günne as a scientific mentor as well as for his powerful English grammar feedback; Dr. Johannes Weber, Vico, Martin, and Christian. It must have been a tough job and was great help.

I would like to thank Marius Schulte for writing a program to visualize tensors in three-dimensions. Further, I would like to express my gratitude to all the students, who participated in projects related to my Ph.D. work.

I very much appreciate the help of all people who helped me in a lab and gave very useful advises: Dr. Andreas Sattler, Dr. Sandro Pagano, Dr. Martin Zeuner, Dr. Rebecca Römer, Dr. Stefan Sedlmaier, Dr. Matthias Schneider, Sophia Makowski, Eva Wirnhier, Nicole Braml and Florian Pucher .

A special thanks to Christian Minke, Thomas Miller and Wolfgang Wünschheim for all kind of help.

Rebecca, Steffi, Sophia, Eva, Nicole and Veronika, it was very nice having you girls around me, to chat and sometimes to have a coffee with you- thanks for everything, it was fun. Chitchat with Vico, Matrin, Johannes, Christian and Daniel was great fun, too. I am sure we will find one bright sunny day to go on a lakeside and discuss our NMR. I wish you all a bright and successful future !

I would also like to thank all my past and present colleagues, who were not mentioned above, and everybody I may have forgotten.

A special thanks to Prof. Dr. Sadgopal Date, Mrs. Jayashree Date and Prof. Satish Dande - for the love and constant support that I have from them all my life.

I am infinitely grateful to my husband Mr. Kedar Kolharkar, who supported me throughout my thesis with all his love, survived all my moods while writing this thesis and took care.

I am deeply indebted to my parents- Mr. Sudhakar Avadhut, Mrs. Sushila

Avadhut and my two sisters-Saroj tai and Yashashree tai, who always supported me. You are among the most important people in my life ! I cannot finish without saying how grateful I am to my new family: Mr. Subhash Kolharkar and Mrs. Sheela Kolharkar- as my new parents; Mr. Rushikesh Kolharkar and Mrs. Anuradha Kolharkar and my niece Gargi.

न चोरहार्यं न च राजहार्यं न भ्रातृभ्राज्यं न च भारकारि ।

व्यये कृते वर्धत एव नित्यं विद्याधनं सर्वधनप्रधानम्॥

The wealth of knowledge cannot be stolen by a thief.
It cannot taken away by a King.
It cannot be divided among brothers.
It does not cause load. It always increases when spent.
The wealth of knowledge is the greatest of all wealths.

Publications

This thesis is based upon the following first six papers which are included in the Results and Discussion chapter. Published or to be published as a part of this thesis.

Paper I

"Accurate determination of chemical shift tensor orientations of single-crystals by solid-state magic angle spinning NMR."
Y. S. Avadhut, J. Weber, and J. Schmedt auf der Günne, (manuscript).

Paper II

"A method for improved quantification of ^{1}H NMR signals under low-resolution conditions for solids."
Y. S. Avadhut, D. Schneider, and J. Schmedt auf der Günne, *J. Magn. Reson.*, **2009**, *201*, 1-6.

Paper III

"N-o-vanillylidene-L-histidine: Experimental charge density analysis of a double zwitterionic amino acid schiff-base compound."
B. Drašković, G. Bogdanović, M. Neelakantan, A.-C. Chamayou, S. Thalamuthu, Y. S. Avadhut, J. Schmedt auf der Günne, S. Banerjee, and C. Janiak, *Crystal Growth & Design*, **2010**, *10*, 1665-1676.

Paper IV

"Characterization of non-crystalline nanomaterials: NMR of zinc phosphate as a case study."
M. Roming, C. Feldmann, Y. S. Avadhut, and J. Schmedt auf der Günne, *Chem. Mater.*, **2008**, *20*, 5787-5795.

Paper V

"Study on the defect structure of SnO_2:F nanoparticles by high resolution solid state NMR."
Y. S. Avadhut, J. Weber, E. Hammarberg, C. Feldmann, I. Schellenberg, R. Pöttgen, and J. Schmedt auf der Günne, *Chem. Mater.* **2011**, *23*, 1526-1538.

Paper VI

"A structural investigation of aluminum doped ZnO nanoparticles by solid-state NMR spectroscopy."
Y. S. Avadhut, J. Weber, E. Hammarberg, C. Feldmann, and J. Schmedt auf der Günne, *Phys. Chem. Chem. Phys.* **2012**, *14*, 11610-11625.

Other Publication

"Characterization of covalent linkages in organically functionalized MCM-41 mesoporous materials by solid-state NMR and theoretical calculations."
J. W. Wiench, Y. S. Avadhut, N. Maity, S. Bhaduri, G. K. Lahiri, M. Pruski, and S. Ganapathy, *J. Phys. Chem. B.*, **2007**, *111*, 3877-3885.

Contents

Chapter 1

Introduction

Solid-state Nuclear Magnetic Resonance (NMR) has proven to be an indispensable tool for the analysis of structure and dynamics in solid materials [1–9]. It is often used in parallel with other techniques like X-ray crystallography, powder X-ray diffraction and ab intio calculation in order to link NMR parameters with structure [10, 11]. Solid-state NMR techniques are sensitive to the local environment of nuclei and capable of detecting any small changes in angles, bond lengths, and molecular symmetry which results in significant effects on solid-state NMR spectra [12–14]. Solid-state NMR is useful for structural characterization of disordered solids e.g. amorphous solids [15–17], nanoparticles [9, 18–22], glasses [23–26], biological samples [27–30], and polymers [31–34].

In solution NMR, sharp, well resolved peaks are normally observed, due to the averaging of anisotropic NMR interactions by the rapid random molecular tumbling [35–38]. In solids, anisotropic NMR interactions generally lead to broad powder patterns that reduce both resolution and sensitivity. However, these broad spectra often contain more valuable information about the chemistry of the sample.

In solid-state NMR, many techniques have been developed that make the acquisition and interpretation easier. Some of the most prominent techniques are magic angle spinning [8, 39–44], cross-polarization [45, 46] and multiple pulse-sequences [8, 42, 47–54].

Solid-state NMR can help to characterize particles in a matrix which can be oriented by external forces. This can be applicable in the case of stretched polymers [31, 55–62] which have interesting materials properties or for analytical reasons, since it can be treated as a single-crystal (see Fig 1.1). Different means of orienting particles in a matrix can be found in literature [63–72]. The case of nanoparticles being oriented in a matrix is shown in Fig 1.1. Nanoparticles have high-surface areas which allow solid-state NMR to study the bonding situation at the surface. These oriented nanoparticles may help to provide information about anisotropic properties. Solid-state NMR could contribute to structural investigation of oriented particles/crystals in several ways which I want to detail

in the following.

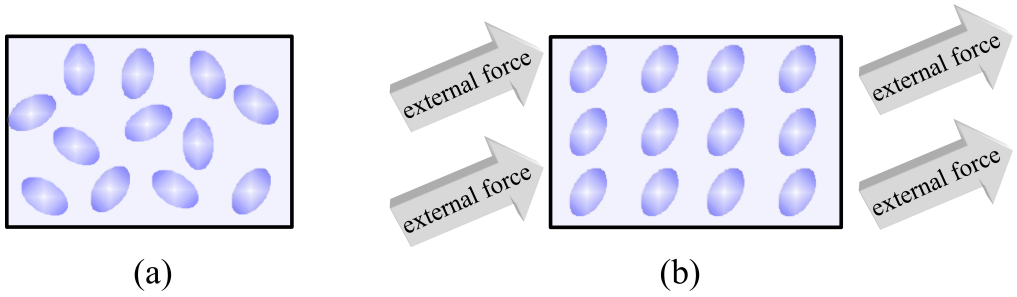

Figure 1.1: (a) Randomly embedded nanoparticles in a polymer matrix are shown as ellipses and (b) resultant oriented nanoparticles embedded in the matrix due to application of an external force.

The goal of this thesis is to develop and apply solid-state NMR methods which are related to (nano-)particles embedded in a matrix either oriented or non-oriented. In this thesis I will focus on three aspects of this situation: 1) methods for oriented particles, which can from an NMR point of view be treated as single-crystals, 2) how can quantitative peak area information be sought in situations where the spectral resolution is rather limited, as in the case of nanoparticles, and 3) methods which give access to the core-shell structure and the dopant environment in nanoparticles.

Single-crystal NMR

The orientation of the chemical shift tensor follows point-group symmetry rules [73,74] and is strongly influenced by the first coordination sphere of the observed atom. Its accurate determination is beneficial to understand valuable structural information about bond angles and the local chemical surrounding if combined with dipolar NMR methods. In solid-state NMR of proteins, several routine methods are based on the directional information of the chemical shift tensor [75–77]. This structural information is not only available for crystalline but also for amorphous solids for which standard X-ray diffraction techniques cannot be used. Despite of their usefulness, chemical shift tensor orientations as shown in Fig. 1.2 are rarely reported in experimental work, because their determination is cumbersome. Moreover, it requires special, expensive equipment, "goniometer probes" [78] and often suffers from line-broadening through dipolar couplings. Examples of such full investigations are given for various nuclei e.g. ^{13}C [78–80], ^{14}N [81], ^{19}F [82], ^{31}P [83–86], ^{59}Co complexes [87], and ^{207}Pb [88], some of which have gained tremendous importance both for the development of NMR methodology [89–93] and in applications [86, 94–97].

Alternatively, chemical shift tensor orientations can be obtained from quantum chemical calculations [75, 98–100]. Such calculations are attractive because

they do not require preparation of huge single-crystals, however they are difficult to perform in case of static or dynamic disorder [100]. Nevertheless, to evaluate the precision of these calculations experimental data are essential.

Another promising way was introduced by Kunath-Fandrei *et al.* [101] using rotorsynchronized magic angle spinning NMR which encode the orientation of the chemical shift tensor with the help of the non-absorptive lineshape of the spinning sideband. Unfortunately, many essential aspects of this method were not discussed, such as error analysis, how an arbitrary crystal can be mounted inside a rotor, a complete protocol, formula for data analysis, etc. The potential advantages of this method are better spectral resolution, considerable time-savings, line narrowing, etc. This to be developed method has a potential to become a routine tool in the field of chemistry e.g. for the characterization of the oriented particles (Fig 1.1).

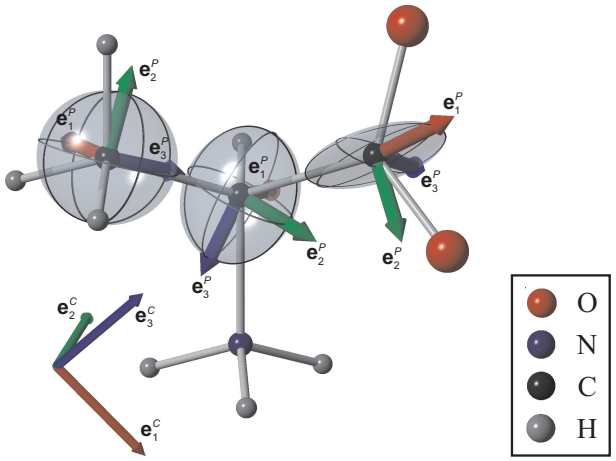

Figure 1.2: ^{13}C chemical shift tensors of L-alanine obtained by static single-crystal NMR [79] for the symmetry operation x, y, z. Tensors are shown in ellipsoid representation [102] with eigenvectors $\mathbf{e}_i^P$ $(i = 1, 2, 3)$. The crystal coordinate system is shown for comparison.

In this work, an improved way of obtaining the chemical shift tensor orientations by single-crystal magic angle spinning NMR is proposed, including the missing factors. It makes the determination of the full tensor information significantly more attractive, as shown in paper-I (see section 3.1).

Quantitative NMR

NMR allows to determine not only the total amount of an NMR active isotope, but also its amount in different chemical environments. Since quantitative analysis by NMR (qNMR) is well established in solution NMR [103, 104], here the focus is on quantification of solid-state NMR spectra. Applications of solid-state

qNMR are wide spread too, covering different areas, e.g. pharmaceutical formulation [105,106], cement base materials [107,108], amorphous materials [109] and for different nuclei like ^{13}C [105,110–113], ^{29}Si [112], ^{119}Sn [112] and ^{23}Na [114].

Quantitative analysis of hydrogen containing samples is interesting where combustion analysis fails, e.g. ceramics (Si_3N_4, AlN, BN), glasses, and polymers. ^{1}H qNMR even complements X-ray diffraction, because NH and O fragments can sometimes be difficult to distinguish from one another. While hydrogen in hydrogen-bonds often results in exceptional chemical shift values (10–18 ppm [115–118]) which helps spectral resolution and its assignment. Systematic studies in solid-state qNMR have highlighted different sources of errors namely repetition delays [105, 110], spectrometer stability [114], pulse-length effects [110], internal/external reference [45,105,113,114] and packing effects [113,114], which may lead to false intensities. An exhaustive protocol for solid-state qNMR has been published [110].

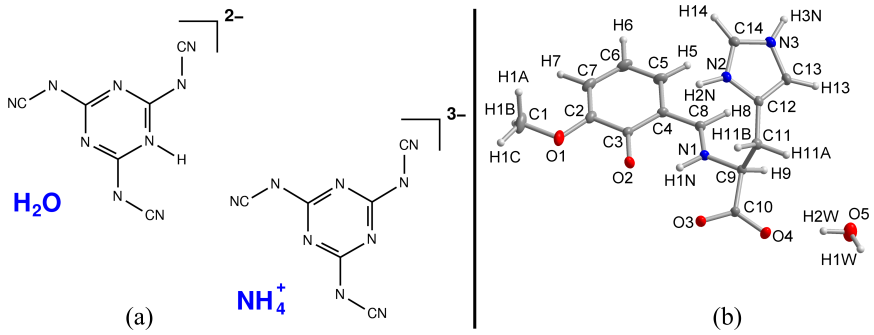

Figure 1.3: (a) Chemically different structures which may be difficult to distinguish by X-ray diffraction [116]. (b) An accurate determination of H signal intensity can tell about the total number of protons in the molecule [117].

Despite all these efforts, quantification of the hydrogen content is still challenging for poorly resolved spectra. Solid-state qNMR of low-resolution spectra can contribute to chemical structure solution and the total number of H atoms in a molecule as shown in Fig 1.3. This approach is also applicable to the oriented particles (Fig 1.1). qNMR can also indicate physisorption and chemisorption on the surface coverage of the nanoparticles.

In this work, I try to identify other error sources which hinder quantification of poorly resolved ^{1}H NMR spectra. This led me to develop an improved protocol which reduces errors to a tolerable level and is supported by an analytical expression for the phase induced intensity errors (see paper-II in section 3.2). This method is used in the case of N-o-Vanillylidene-L-histidine to confirm the zwitterionic structure described in paper-III (see section 3.2).

Solid-state NMR on Nanoparticles

In the past years, nanoparticles have been studied intensively [119–122]. Their properties are closely linked to structure, that is why there is an increasing need for their characterization [123–126]. Solid-state NMR holds the promise for probing spatial variations in nanoparticle composition, interfacial structure, and other features on the nanometer scale [9, 18–22, 127].

Solid-state NMR methods can be used to gain a detailed insight of quantitative internuclear distance constraints and defect structure of nanoparticles. In many cases, point defects are essential for electrical and optical imperfections. Understanding how, why, and where they appear, and, as epitome, revealing their atomic nature, would be advantageous. In order to understand the properties, one needs an accurate knowledge of their microscopic structure, e.g. material homogeneity, chemical composition, core-shell model or core-free model with homogeneous composition as shown in Fig 1.4.

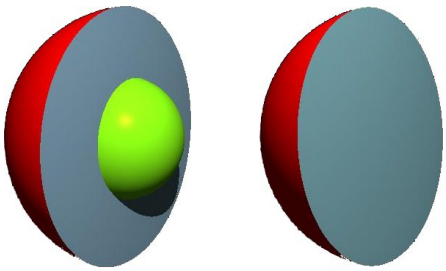

Figure 1.4: Nanoparticle models as an example: (a) core-shell model and (b) core-free model with homogeneous composition.

Recently, Schmidt-Rohr *et al.* published an NMR method for characterizing the thickness of nanoparticles in organic-inorganic nanocomposites called heteronuclear recoupling with dephasing by strong homonuclear interactions of protons (HARDSHIP) [127]. This method helps to eliminate dephasing by protons in the inorganic phase. Alternatively, quantitative heteronuclear distances can be achieved with a variant of rotational echo double resonance (REDOR) experiment [128] called C-REDOR [129, 130]. Here, for the first time, comparison of experimental C-REDOR curves with core-shell models of nanoparticles is described, and numerical analysis of C-REDOR curves for various topologies is explained.

Many commercial NMR probes have significant background signals. Background suppression is necessary when probing the homogeneity of point defects and its dynamics in doped nanoparticles. Whether the dopant is homogeneously distributed into the sample or forms cluster around specific atoms is an important issue and allows a deeper understanding of structure. For this purpose, I present a modified two-dimensional sequence with dipolarly mediated exchange

derived from the symmetry based pulse sequence $SR6_6^2$ (2D-$SR6_6^2$) [131], which helps to suppress background signals. Further, to investigate dopant dynamics, background compensation is achieved by a modified two-dimensional exchange spectroscopy (2D-EXSY) [132].

To understand point defects in detail, the heteronuclear connectivity pattern over less than a nanometer is necessary. For isotopes with large anisotropic interactions, such as half-integer quadrupolar nuclei, heteronuclear correlation experiments, based on ramped cross-polarization (HETCOR) [133,134] are difficult, since the Hartmann-Hahn condition is hard to achieve. There is a good alternative technique, relying on symmetry-based recoupling sequences namely Phase-shifted Recoupling Effects a Smooth Transfer of Order (PRESTO) [135]. However, its implementation in two-dimensions has not been done. To prove heteronuclear connectivity, a modified two-dimensional PRESTO-III (2D-PRESTO-III) is presented.

In this work, on the basis of existing solid-state NMR techniques [128, 133, 134, 136–140], combined with the newly modified solid-state NMR techniques, I propose different structural models of various cases. The combined approach of solid-state NMR techniques served as a guide to the analysis of nanoparticles which are applied independently and/or as a group of methods for i) zinc phosphate nanoparticles with its wide range of applications [141–147] as shown in the paper-IV (see section 3.3); and ii) Transparent Conductive Oxides (TCOs) [148–150], namely fluorine doped tin oxide and aluminum doped zinc oxide nanoparticles which are the most commonly employed TCOs in energy efficient windows [151–155], in paper-V and in paper-VI, respectively (see section 3.3).

Overview of the Thesis

In chapter 2, I will selectively review theory and methods which are helpful to understand the presented methodological achievements. The results are presented in detail in the manuscripts and articles which are part of this thesis in Chapter 3. The conclusions and a short summary (chapters 4 and 5) finalize this document and try to elucidate the results from a general perspective. Appendix A contains relevant tensor components and their relationships for different spin interactions under high-field approximation. The appendices further include an implementation of a double resonance frequency splitter, used for $^{19}F\{^1H\}$ C-REDOR experiments (Appendix B), a hardware-assembly for single-crystal MAS NMR (Appendix C), simpson input file with an add-on to the simpson [156, 157] program (Appendix D), mathematica modules (Appendix E), and relevant pulse programs (Appendix F).

Chapter 2

NMR: Basics, Theory, and Techniques

Nuclear Magnetic Resonance (NMR) is a spectroscopic tool for examining molecular motions and structures, and may be applied to a larger variety of systems in the liquid, solid, and gaseous state. This chapter will review the fundamentals of NMR spectroscopy from the solid-state point of view. In the following, a brief overview of the basic principles of NMR spectroscopy and the topics addressed in this thesis will be given.

2.1 Basic Principles of NMR Spectroscopy

Matter is made of *atoms* which are composed of *electrons* and *nuclei*. The nucleus has four important physical properties: *mass*, *electric charge*, *magnetism*, and *spin*. The nucleus interacts with magnetic fields through its magnetic moment. This property is called nuclear magnetism. The nucleus has intrinsic angular momentum, which is known as spin. Although nuclear magnetism and spin have very little effect on the chemical and physical behavior of the material, they do provide the essential ingredients enabling NMR to be a useful tool.

2.1.1 Spin Angular Momentum

A rotating object possesses *angular momentum*. The spin is also a form of angular momentum, which is not produced by a rotation of the particle but is an intrinsic property of the particle itself. According to quantum mechanics, the *spin angular momentum* is quantized taking values of the form $\hbar\sqrt{I(I+1)}$, where I is the *spin quantum number*. Each elementary particle has an associated spin quantum number that is an integer or half-integer, $(0, 1/2, 1, 3/2, ...)$. For instance, electrons have spin-1/2, whereas photons have spin-1.

The nuclear spin depends on the spin of their constituents: *nucleons* (protons

and neutrons), which are made of elementary particles called *quarks* held together by *gluons* [158]. NMR spectroscopy can only be performed on nuclei with a spin not equals to zero. Table 2.1 contains properties for a few nuclei commonly used in NMR.

The nuclei with spin $I \neq 0$ have an *associated magnetic moment* that is proportional to the spin angular momentum [159, 160]:

$$\hat{\mu} = \gamma \hat{I} \tag{2.1}$$

where γ is the gyromagnetic ratio in units of rad/s/T [158]. The gyromagnetic ratio has a positive or negative sign depending on the relative orientation between the spin angular momentum and the magnetic moment vector.

Table 2.1: A Selection of nuclear spin and their properties [158].

Isotope	Spin[a]	Natural Abundance (%)	Gyromagnetic Ratio γ/(rad/s/T)	Larmor Frequency at $B_0 = 11.74$ T $\omega_0/2\pi$/(MHz)
^{1}H	1/2	∼100	267.522×10^6	-500.000
^{13}C	1/2	1.1	67.283×10^6	-125.725
^{15}N	1/2	0.37	-27.126×10^6	50.684
^{27}Al	5/2	100	69.763×10^6	-130.285
^{31}P	1/2	100	108.394×10^6	-202.606

[a] nuclear spin in ground state

2.1.2 Spin Precession and Larmor Frequency

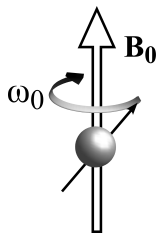

Figure 2.1: A single spin in an external magnetic field $\mathbf{B}_0$ indicates negative spin precession as $\gamma > 0$.

If an external field is applied to the sample, the magnetic moments of the nuclei start precessing around the axis of the external magnetic field. As the nuclei possess spin angular momentum, the nuclear magnetic moments do not align with the external field. The direction of the spin angular momentum is known

as the *spin polarization axis*. The frequency at which the spin polarization axis precesses around the external magnetic field is called the *Larmor frequency*, as given by:

$$\omega_0 = -\gamma B_0 \tag{2.2}$$

where B_0 is the magnitude of the magnetic field at the nuclear site considered. The sign of the Larmor frequency indicates the direction of the spin precession around the external magnetic field which depends on the gyromagnetic ratio.

Fig. 2.1 shows the precession of the spin polarization axis for a single spin with $\gamma > 0$. The frequency ω_0 is an angular frequency and therefore given in units of rad/s. The frequency $\omega_0/2\pi$ is specified in Hz. Table 2.1 contains the Larmor frequencies of selected isotopes in an external magnetic field with $B_0 = 11.74$ T.

2.1.3 The Bloch Equations and Relaxation

In the absence of an external magnetic field, the individual nuclear magnetic moments have random orientations so that there is no net magnetization. In order to describe NMR experiments, macroscopic behavior of samples of spins is important. A theoretical concept so called an *ensemble* of spins is used which can be explained as- a large collection of identical and independent spin systems. At the thermal equilibrium, an ensemble of non-interacting spins can be represented by a *magnetization vector* [13,54,161]. The magnetization vector, $\mathbf{M}$, is an averaged nuclear magnetic moment of the ensemble and oriented along the direction of the external magnetic field as shown in Fig. 2.2 (a).

In classical physics, the magnetization vector is a macroscopic quantity. Using the Bloch equations, a motion of the magnetization vector ($\mathbf{M}$) in the external magnetic field is described. In terms of individual components of the magnetization, the Bloch equations are [161]:

$$\frac{dM_z}{dt} = \gamma(\mathbf{M} \times \mathbf{B}_0)_z - \left(\frac{1}{T_1}\right)(M_z - M_z^{eq}) = \left(\frac{1}{T_1}\right)(M_z - M_z^{eq}) \tag{2.3}$$

$$\frac{dM_x}{dt} = \gamma(\mathbf{M} \times \mathbf{B}_0)_x - \frac{M_x}{T_2} = \gamma M_y B_0 - \frac{M_x}{T_2} \tag{2.4}$$

$$\frac{dM_y}{dt} = \gamma(\mathbf{M} \times \mathbf{B}_0)_y - \frac{M_y}{T_2} = -\gamma M_x B_0 - \frac{M_y}{T_2} \tag{2.5}$$

where γ is the gyromagnetic ratio and $\mathbf{B_0}$ is the external magnetic field. These Bloch equations provide a simple description of the observed NMR phenomenon. Moreover, they take into consideration the nuclear spin relaxation.

Equation 2.3 represents the time variation of the longitudinal component of the magnetization vector along the external magnetic field. The equation shows the exponential behavior and predicts magnetization component along B_0 to relax its equilibrium value, M_z^{eq}. The time constant for this process is known as *longitudinal* or *spin-lattice* relaxation time. It is denoted by T_1. Similarly, the

motion of the transverse components of the magnetization vector is described by equations 2.4 and 2.5. The x and y components of the magnetization vector ($\mathbf{M}$) are detected in a frame rotating around z with an angular frequency $\omega_0 = \gamma B_0$ as shown in Fig. 2.2 (b). In a rotating frame, the decay of M_x and M_y, with time rate constant T_2^{-1}, is easily observed. The rate of the relaxation of these components is characterized by a time constant T_2, called the *transverse* or *spin-spin* relaxation time. It describes the exponential decay of the xy-magnetization to its equilibrium value of zero.

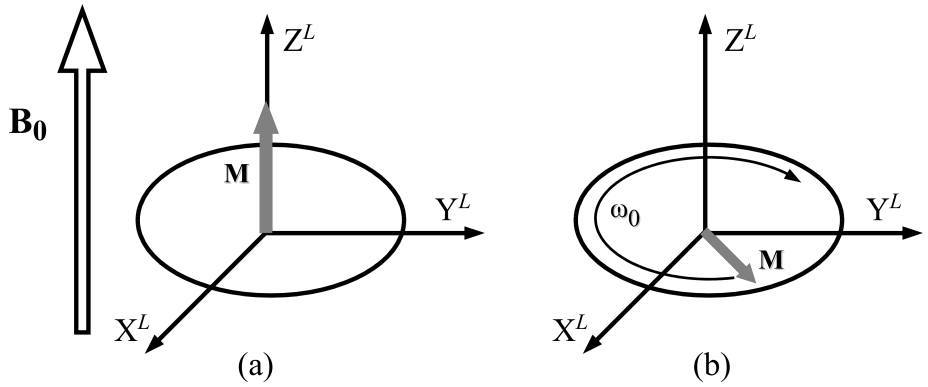

Figure 2.2: Macroscopic magnetization of a spin system shown in a laboratory reference frame L, the z^L-axis points to the direction of an external magnetic field $\mathbf{B}_0$: (a) Longitudinal magnetization after the thermal equilibrium has been reached in the external magnetic field. (b) Transverse magnetization precesses around the external magnetic field with the Larmor frequency ω_0.

2.1.4 NMR Signal

After an rf pulse, the precessing transverse magnetization is very small but detectable, since it oscillates at a well defined frequency. A rotating magnetic moment generates a rotating magnetic field. A changing magnetic field is associated with an electric field. If a wire-coil is placed near the sample, this electric field induces a voltage which causes an oscillating electric current in the wire. This oscillating current can be detected using a radiofrequency detector. The oscillating electric current induced by the precessing nuclear transverse magnetization is called the *NMR signal* or *free induction decay* (FID). It is plotted in terms of amplitude as function of time. This may be converted into the frequency domain, the *spectrum*, by a mathematical procedure called a *Fourier Transformation* (FT) [162]. It is represented by amplitude as function of frequency.

In Fig. 2.3, the relationship is shown between the signals in time and frequency domains. For an extensive description of the NMR spectrometer and Fourier Transformation (FT) method see [158, 163, 164].

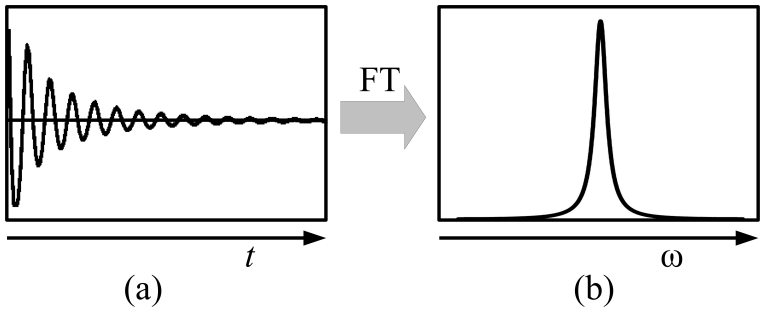

Figure 2.3: The NMR signal in the time and frequency domain is shown in (a) and (b), respectively. These are converted into each other by a Fourier Transformation (FT) or an inverse FT.

2.2 Solid-State NMR Theory

To understand the basics of the *dynamics* of nuclear spins [158], it is necessary to solve the *time-dependent Schrödinger equation* for the time evolution, which describes the evolution of the wave function of a physical system:

$$\frac{d}{dt}|\Psi_{full}(t)\rangle = -i\hat{\mathcal{H}}_{full}|\Psi_{full}(t)\rangle \tag{2.6}$$

where $\hat{\mathcal{H}}_{full}$ is a *Hermitian operator*, called the *Hamiltonian* associated with the total energy of the system and $|\Psi_{full}(t)\rangle$ is the wave function that describes the quantum state of the system. In this thesis the Hamiltonian, $\hat{\mathcal{H}}$, is defined in natural units, which means that spin becomes a dimensionless property and the Hamiltonian is not given in units of Joule (J) but in 1/s or Hz. Both quantities may be converted to SI units by multiplication with $\hbar$.

In NMR, it is possible to work with a much simpler equation, in which only the nuclear spin states appear:

$$\frac{d}{dt}|\Psi_{spin}(t)\rangle = -i\hat{\mathcal{H}}_{spin}|\Psi_{spin}(t)\rangle \tag{2.7}$$

In this equation $|\Psi_{spin}(t)\rangle$ is the spin state of the nuclei and $\hat{\mathcal{H}}_{spin}$ is the nuclear spin Hamiltonian. This Hamiltonian only includes terms dependent on the nuclear spin, while the other contributions to the full Hamiltonian occur in form of different interactions described below.

For a system of spins, the total spin Hamiltonian $\hat{\mathcal{H}}^{total}$ can be represented as a sum of interaction Hamiltonian terms:

$$\hat{\mathcal{H}}^{total}_{spin} = \hat{\mathcal{H}}_Z + \hat{\mathcal{H}}_{RF} + \hat{\mathcal{H}}_{CS} + \hat{\mathcal{H}}_J + \hat{\mathcal{H}}_{DD} + \hat{\mathcal{H}}_Q + ... \tag{2.8}$$

The main interactions are [158, 165, 166]:

- $\hat{\mathcal{H}}_Z$, the Zeeman Hamiltonian that describes the interaction of the nuclear spins with the external static magnetic field, $\mathbf{B}_0$
- $\hat{\mathcal{H}}_{RF}$, the RF Hamiltonian is a time-dependent Hamiltonian. It describes the interaction of the spins with the external time-dependent field of a rf pulse, $\mathbf{B}_{RF}(t)$
- $\hat{\mathcal{H}}_{CS}$, the chemical shift Hamiltonian that describes the effect of electronic shielding of $\mathbf{B}_0$
- $\hat{\mathcal{H}}_J$, the J-coupling Hamiltonian, that describes the internuclear, indirect magnetic dipole-dipole interaction that is mediated by electrons
- $\hat{\mathcal{H}}_{DD}$, the direct dipole-dipole coupling Hamiltonian that describes a through-space spin-spin interaction
- $\hat{\mathcal{H}}_Q$, the quadrupole coupling Hamiltonian that describes the interaction of nuclei having $I > \frac{1}{2}$ and therefore a quadrupole moment with an electric field gradient

The external and the internal spin interactions are explained in details in section 2.7 and 2.8, respectively.

2.3 Spin Angular Momentum Operators

As per the quantum description of the *spin angular momentum operator*, its three components along the three axes, x, y, and z are denoted by $\hat{I}_x$, $\hat{I}_y$, and $\hat{I}_z$. These three components of the spin angular momentum operator follow *cyclic commutation relationships* [158, 167–169]:

$$[\hat{I}_x, \hat{I}_y] = i\hat{I}_z\,; \quad [\hat{I}_y, \hat{I}_z] = i\hat{I}_x\,; \quad [\hat{I}_z, \hat{I}_x] = i\hat{I}_y \tag{2.9}$$

and the *total square spin angular momentum operator* is defined as:

$$\hat{I}^2 = \hat{I}_x^2 + \hat{I}_y^2 + \hat{I}_z^2 \tag{2.10}$$

Since $\hat{I}^2$ commutes with $\hat{I}_z$ as well as these operators are hermitian, a common set of *eigenfunctions* $|I, m\rangle$ can be chosen for the both operators. The *eigenequations* of $\hat{I}^2$ are defined below:

$$\hat{I}^2|I, m\rangle = I(I+1)|I, m\rangle \tag{2.11}$$

Here, the *eigenvalues* of the $\hat{I}^2$ are given by $I(I+1)$ with $I = 0, 1/2, 1, 3/2, ...$ The eigenvalues of $\hat{I}_z$ for the same eigenfunction are given by:

$$\hat{I}_z|I, m\rangle = m|I, m\rangle \tag{2.12}$$

where the eigenvalues are given by m with $m = -I, -I+1, ..., I-1, I$.

2.4 Zeeman Eigenbasis

For a spin-1/2 nucleus with $I = 1/2$, the two possible eigenvalues of the spin quantum number I are $m = \pm 1/2$. The eigenstates of the angular momentum along the z-axis are called *Zeeman eigenstates*. They are denoted in bra-ket notation where the first number refers to the spin quantum number I and the second to the magnetic quantum number m:

$$|\alpha\rangle = |\frac{1}{2}, +\frac{1}{2}\rangle; \quad |\beta\rangle = |\frac{1}{2}, -\frac{1}{2}\rangle \tag{2.13}$$

The eigenstates $|\alpha\rangle$ and $|\beta\rangle$ follow the eigenequations:

$$\hat{I}_z|\alpha\rangle = \frac{1}{2}|\alpha\rangle; \quad \hat{I}_z|\beta\rangle = -\frac{1}{2}|\beta\rangle \tag{2.14}$$

In the *Zeeman eigenbasis*, the three components of the spin angular momentum operator are given in the matrix representations as below:

$$\hat{I}_z = \frac{1}{2}\begin{pmatrix} 1 & 0 \\ 0 & -1 \end{pmatrix}; \quad \hat{I}_x = \frac{1}{2}\begin{pmatrix} 0 & 1 \\ 1 & 0 \end{pmatrix}; \quad \hat{I}_y = \frac{1}{2i}\begin{pmatrix} 0 & 1 \\ -1 & 0 \end{pmatrix} \tag{2.15}$$

and the *shift operators* of the spin angular momentum:

$$\hat{I}^+ = \hat{I}_x + i\,\hat{I}_y; \quad \hat{I}^- = \hat{I}_x - i\,\hat{I}_y \tag{2.16}$$

The matrix representations of the shift operators in the Zeeman eigenbasis are as follows:

$$\hat{I}^+ = \begin{pmatrix} 0 & 1 \\ 0 & 0 \end{pmatrix}; \quad \hat{I}^- = \begin{pmatrix} 0 & 0 \\ 1 & 0 \end{pmatrix} \tag{2.17}$$

2.5 Tensors

In NMR, different measurable properties can be described as tensors of rank-0, rank-1, or rank-2. A tensor of rank-0 is a scalar quantity and can be described by a number. Examples of tensors of rank-0 are the electric monopole charge, the isotropic chemical shift or the mass of a particle. A tensor of rank-1 is a vector and has magnitude and direction. Examples of rank-1 tensors are physical properties such as magnetic or electric fields. Tensors of rank-2 can be represented in matrix form to describe physical properties which behave different in different directions. Properties such as conductivity, magnetic susceptibility and dipole-dipole interaction are tensors of rank-2.

The chemical shift interaction can be described as a rank-2 tensor. It is the basis of my contribution to single-crystal MAS NMR. The mathematical tools to describe how a chemical shift tensor changes when being subjected to a series of rotations, are introduced in this chapter.

2.5.1 Rotation of Rank-2 Cartesian Tensor According to the Rose Convention

The passive rotation of a tensor can be described by the rotation of the coordinate system, e.g. for a rank-2 tensor, A, the rotation from the Cartesian system B to the Cartesian system D is described by three Euler angles $\Omega_{BD} = (\alpha_{BD}, \beta_{BD}, \gamma_{BD})$. Unfortunately there are many ways to define the rotation with three Euler angles. Here I follow the convention by Rose the so called "Z-Y-Z" convention [170] which is defined as *passive rotations* by Schmidt-Rohr and Spiess [31]. Two right-handed coordinate systems are defined through their three orthogonal unit vectors X, Y and Z. The Euler angles α, β, and γ in the Rose convention describe the rotation in the mathematically positive sense around three well defined axes as shown in Fig 2.4 (a) and can be expressed as:

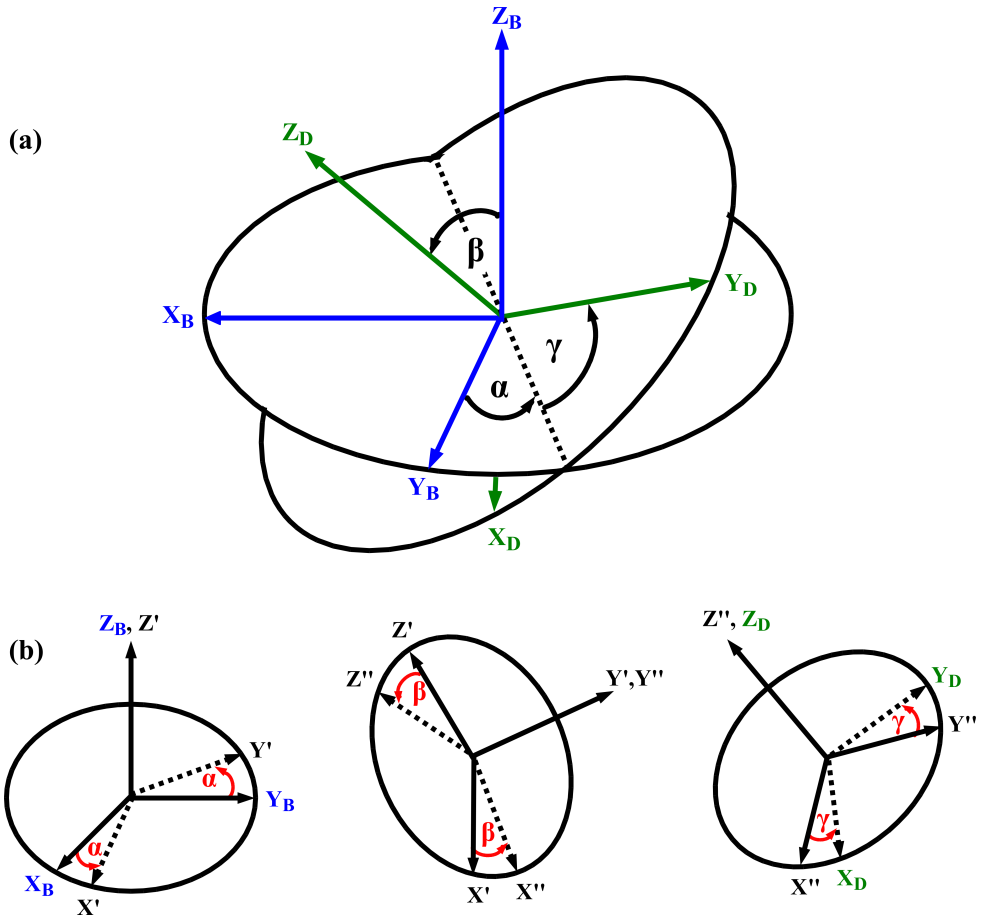

Figure 2.4: (a) Definition of the Euler angles, $\Omega_{BD} = \alpha, \beta, \gamma$, according to the Rose convention [31,170]. (b) How to find the Euler angles (α, β, γ) relating two coordinate systems (X_B, Y_B, Z_B) and (X_D, Y_D, Z_D) using "Z-Y-Z" convention [170].

- $\boldsymbol{\alpha} = \alpha_{BD}$: The initial or original coordinate system (X_B, Y_B, Z_B) is rotated by an angle α about its Z_B-axis to give a new coordinate system (X', Y', Z') (Fig 2.4 (b, left)).
- $\boldsymbol{\beta} = \beta_{BD}$: The new coordinate system (X', Y', Z') is then rotated by an angle β about its Y'-axis to give an another new coordinate system (X'', Y'', Z'') (Fig 2.4 (b, middle)).
- $\boldsymbol{\gamma} = \gamma_{BD}$: The coordinate system (X'', Y'', Z'') is finally rotated by an angle γ about its Z''-axis to give the required coordinate system (X_D, Y_D, Z_D) (Fig 2.4 (b, right)).

Mathematically, the combined effect of these rotations can be expressed by a set of Euler angles, the so-called an *Euler rotation matrix*, $\mathbf{R}(\alpha,\beta,\gamma)$. The valid ranges of the angles have to be respected ($\alpha \in [0,360), \beta \in [0,180], \gamma \in [0,360)$).

A vector $\vec{r}$ that is expressed in a coordinate system B can be transformed to coordinate system D as follows:

$$\vec{r}_D = \mathbf{R}^{-1}(\alpha_{BD},\beta_{BD},\gamma_{BD}) \cdot \vec{r}_B \tag{2.18}$$

where $\mathbf{R}^{-1}(\alpha_{BD},\beta_{BD},\gamma_{BD})$ is called a "pseudo active" rotation matrix or Euler rotation matrix, but does really perform a passive rotation, i.e. the vector $\vec{r}$ stays in place while the coordinate system changes from B to D. $\widetilde{\mathbf{R}} = \mathbf{R}^{-1}(\alpha_{BD},\beta_{BD},\gamma_{BD})$ is defined as:

$$\begin{aligned}
\widetilde{\mathbf{R}} &= \mathbf{R}_z^{-1}(\gamma)\mathbf{R}_y^{-1}(\beta)\mathbf{R}_z^{-1}(\alpha) \\
\widetilde{\mathbf{R}} &= \begin{pmatrix} c\alpha \cdot c\beta \cdot c\gamma - s\alpha \cdot s\gamma & s\alpha \cdot c\beta \cdot c\gamma + c\alpha \cdot s\gamma & -s\beta \cdot c\gamma \\ -c\alpha \cdot c\beta \cdot s\gamma - s\alpha \cdot c\gamma & -s\alpha \cdot c\beta \cdot s\gamma + c\alpha \cdot c\gamma & s\beta \cdot s\gamma \\ c\alpha \cdot s\beta & s\alpha \cdot s\beta & c\beta \end{pmatrix}
\end{aligned} \tag{2.19}$$

The following abbreviations are used, $c\alpha = \cos\alpha_{BD}$, $s\alpha = \sin\alpha_{BD}$, *etc.*

A tensor T_B can be transformed between the coordinate systems B and D using following transformation:

$$T_D = \widetilde{\mathbf{R}}(\alpha_{BD},\beta_{BD},\gamma_{BD}) \cdot T_B \cdot \widetilde{\mathbf{R}}^{-1}(\alpha_{BD},\beta_{BD},\gamma_{BD}) \tag{2.20}$$

2.5.2 Irreducible Spherical Tensors and Wigner Rotation Matrices

For the description of NMR theory and NMR interactions, spherical tensors play an important role. In order to understand the different Hamiltonian terms in NMR, it is convenient to use the Cartesian tensors. However, the Cartesian representation of a tensor is reducible and does not correspond to definite projection of quantum number, therefore from a mathematical point of view it complicates the transformation under a rotation operation [170].

To simplify the transformation, a second rank Cartesian tensor (A) can be decomposed into three irreducible tensors, with a total of nine components (a_{ij}). A tensor of rank-0 with a single component representing the trace of the tensor, an antisymmetric tensor of rank-1 with three components, and a symmetric tensor of rank-2 having five components. Each irreducible spherical tensor ($\mathcal{A}_2$) of rank-2 is made up of a set of elements $\mathcal{A}_{2m}$ $(-2 \leq m \leq 2)$ which can be constructed from a symmetric Cartesian 3×3 matrix, A, according to the relations given in Table 2.2 [31].

Table 2.2: A relation between the irreducible spherical tensor and the Cartesian tensor of second rank [31, 171].

$\mathcal{A}_{0,0} = \frac{1}{3}(A_{xx} + A_{yy} + A_{zz})$	
$\mathcal{A}_{1,0} = \frac{-i}{\sqrt{2}}(A_{xy} - A_{yx})$	$\mathcal{A}_{1,\pm1} = -\frac{1}{2}\{(A_{zx} - A_{xz}) \pm i(A_{zy} - A_{yz})\}$
$\mathcal{A}_{2,0} = \sqrt{\frac{3}{2}}(A_{zz} - \mathcal{A}_{0,0})$	$\mathcal{A}_{2,\pm1} = \mp\frac{1}{2}\{(A_{zx} + A_{xz}) \pm i(A_{zy} + A_{yz})\}$
	$\mathcal{A}_{2,\pm2} = \frac{1}{2}\{(A_{xx} - A_{yy}) \pm i(A_{xy} + A_{yx})\}$

If a general rotation $\hat{R}(\alpha, \beta, \gamma)$ (α, β, γ are the Euler angles, discussed in section 2.5.1) is applied to an object, A_{lm}, of certain rank l with m components, this rotation leads to a transformation into another object, $A_{lm'}$, with the same rank l [13, 31]:

$$\hat{R}(\Omega) A_{lm} \hat{R}^{-1}(\Omega) = \sum_{m'=-l}^{+l} D^l_{mm'}(\Omega) A_{lm'} \tag{2.21}$$

where $\hat{R}$ is the rotation operator. The coefficients $D^l_{mm'}(\Omega)$ are the *Wigner rotation matrices*, with the Euler angles $\Omega = \alpha, \beta, \gamma$, which specify the coordinate transformation. The Wigner matrix elements can be decomposed into three separate factors, each depending on one of the Euler angles:

$$D^l_{mm'}(\Omega) = e^{-im\alpha}\, d^l_{mm'}(\beta)\, e^{-im'\gamma} \tag{2.22}$$

The term $d^l_{mm'}(\beta)$ is called a *reduced rotation matrix element*. The reduced rotation matrix element depends on the value of l.

For example, two reference frames, namely K and K', are considered which are related by a rotation operation. A set of Euler angles $\Omega_{KK'} = (\alpha_{KK'}, \beta_{KK'}, \gamma_{KK'})$ is used to describe the rotation from the frame K to the frame K'. An *irreducible spherical tensor* with a rank l has $m = 2l + 1$ components where m takes integer values from $-l$ to l. The transformation of K to K' is then given by:

$$[A_{lm}]^{K'} = \sum_{m'=-l}^{l} D^l_{mm'}(\Omega_{KK'}) [A_{lm'}]^K \tag{2.23}$$

An *irreducible spherical tensor operator* (ISTO) may be defined as a basis set representation of $2l+1$ operators, $\mathcal{A}_{lm}$, where $m = (-l, -l+1, ..., l)$, with analogous rotational properties to those of irreducible spherical tensors:

$$[\hat{\mathcal{A}}_{lm}]^{K'} = \sum_{m'=-l}^{l} D^{l}_{mm'}(\Omega_{KK'})[\hat{\mathcal{A}}_{lm'}]^{K} \tag{2.24}$$

A useful relation of the Wigner matrices is given by their *addition* theorem. If the rotation between K and K' occurs via an intermediate frame F, the Wigner matrix elements $D^{l}_{mm'}(\Omega_{KK'})$ are given by [31]:

$$D^{l}_{mm'}(\Omega_{KK'}) = \sum_{m''=-l}^{l} D^{l}_{mm''}(\Omega_{KF}) \cdot D^{l}_{m''m'}(\Omega_{FK'}) \tag{2.25}$$

Here, the Euler angles have been combined into $\Omega_{KK'} = (\alpha_{KK'}, \beta_{KK'}, \gamma_{KK'})$.

2.5.3 Spin Hamiltonian in an ISTO Representation

A nuclear *spin Hamiltonian* can be written as a summation of different spins interactions Λ:

$$\hat{\mathcal{H}}_{spin} = \sum_{\Lambda} \hat{\mathcal{H}}^{\Lambda}_{spin} \tag{2.26}$$

The spin Hamiltonian for an interaction Λ can be represented in the Cartesian basis as follows [165]:

$$\hat{\mathcal{H}}^{\Lambda}_{spin} = C^{\Lambda}\, \mathbf{U} \cdot \mathrm{A}^{\Lambda} \cdot \mathbf{V} \tag{2.27}$$

Here, C^{Λ} is a coefficient which depends on the spin interactions, $\mathbf{U}$ and $\mathbf{V}$ are vector operators, and A^{Λ} is a second-rank Cartesian tensor which depends on the interaction Λ as well as on spatial orientation.

The spherical tensor representation of the spin Hamiltonian of an interaction Λ can be expressed as a scalar product of two irreducible spherical tensor operators [172, 173]:

$$\hat{\mathcal{H}}^{\Lambda}_{spin} = C^{\Lambda} \sum_{l} \sum_{m=-l}^{l} (-1)^{m} [\mathcal{A}^{\Lambda}_{lm}]^{K} [\mathcal{T}^{\Lambda}_{l-m}]^{K} \tag{2.28}$$

This separates the *spatial tensor* $[\mathcal{A}^{\Lambda}_{l}]$ and the *spin-field tensor* $[\mathcal{T}^{\Lambda}_{l}]$. The spatial and the spin-field form of each spin interaction is given in Table 2.3. The spin-field tensor has a spin and a field part where the field is a static external magnetic field and the spin part can be rotated by external radio frequency (rf) fields. As a consequence, the internal Hamiltonian can be written in terms of pure irreducible spherical spin tensors $[T^{\Lambda}_{\lambda}]$ of rank λ instead $[\mathcal{T}^{\Lambda}_{l}]$. Further, a spatial tensor $[A^{\Lambda}_{\lambda}]$ can be defined, which is related by numerical factors to the spatial tensor $[\mathcal{A}^{\Lambda}_{l}]$.

Here, the spatial and spin tensors rank can be different and their forms are given in Table 2.4. The transformation of the Hamiltonian under rotations are described by the quantum numbers l, m, λ, μ where l is the spatial rotational rank and λ is the rank with respect to rotations of the spin polarization. The other two components m and μ take values $m = -l, -l+1, ..., +l$ and $\mu = -\lambda, -\lambda+1, ..., +\lambda$.

Table 2.3: The space and spin parts for spin interactions [174].

Interactions	Frame	Space part				Spin part
		$[A^{\Lambda}_{00}]^F$	$[A^{\Lambda}_{20}]^F$	$[A^{\Lambda}_{2\pm1}]^F$	$[A^{\Lambda}_{2\pm2}]^F$	
Zeeman	L	ω_0	-	-	-	T^j_{10}
isoCS	L	$\omega_0\delta^j_{iso}$	-	-	-	T^j_{10}
CSA	P	-	$\omega_0(\delta^p_{zz} - \delta^j_{zz})$	0	$\frac{\eta}{\sqrt{6}}[A_{20}]^P$	T^j_{10}
Homo DD-couplings	P	-	$\sqrt{6}b_{ij}$	0	0	T^{ij}_{20}
Homo J-couplings	L	$-\sqrt{3}2\pi J$	-	-	-	T^{ij}_{00}
Heter DD-couplings	P	-	$2b_{ij}$	0	0	$T^I_{10}T^S_{10}$
Heter J-couplings	L	$2\pi J$	-	-	-	$T^I_{10}T^S_{10}$

Usually, the spatial tensor is expressed in the principal axis frame P^{Λ}, however rotated to the laboratory frame with the Euler angles Ω^{Λ}_{PL} and the Hamiltonian finally has to be expressed in the laboratory frame. Therefore, the spin Hamiltonian using equation 2.23 is given as:

$$[\mathcal{A}^{\Lambda}_{lm}]^L = \sum_{m'=-l}^{l} D^l_{mm'}(\Omega^{\Lambda}_{PL})[\mathcal{A}^{\Lambda}_{lm'}]^P \tag{2.29}$$

Here, Ω^{Λ}_{PL} is the set of Euler angles which relates the P frame and L frame. The equation (2.28) for the spin Hamiltonian of an interaction Λ can be written as:

$$\hat{\mathcal{H}}^{\Lambda}_{spin} = C^{\Lambda}\sum_{l}\sum_{\lambda}\sum_{m,m'=-l}^{l}\sum_{\mu=-\lambda}^{\lambda}(-1)^m[\mathcal{A}^{\Lambda}_{lm'}]^P D^l_{mm'}(\Omega^{\Lambda}_{PL})[\mathcal{T}^{\Lambda}_{\lambda\mu}]^L \tag{2.30}$$

Table 2.4: Relationships between the spatial tensor components $\mathcal{A}_{lm}^{\Lambda}$ and $A_{lm'}^{\Lambda}$ and the spin tensor components $T_{\lambda 0}^{\Lambda}$ and the spin-field tensor components $\mathcal{T}_{\lambda 0}^{\Lambda}$ [174].

Interactions	C^{Λ}	Space Part	Spin Part
Zeeman	$-\gamma$	$[\mathcal{A}_{00}]^L = -\frac{\sqrt{3}}{\omega_0}[A_{00}]^L$	$[\mathcal{T}_{00}]^L = -\frac{1}{\sqrt{3}}B_0 T_{10}^j$
isoCS	$-\gamma$	$[\mathcal{A}_{00}]^L = -\frac{\sqrt{3}}{\omega_0}[A_{00}]^L$	$[\mathcal{T}_{00}]^L = -\frac{1}{\sqrt{3}}B_0 T_{10}^j$
CSA	$-\gamma$	$[\mathcal{A}_{2m}]^P = \frac{\sqrt{3}}{\sqrt{2}}\omega_0[A_{2m}]^P$	$[\mathcal{T}_{20}]^L = \sqrt{\frac{3}{2}}B_0 T_{10}^j$
Homo DD-couplings	1	$[\mathcal{A}_{2m}]^P = [\mathcal{A}_{2m}]^P$	$[\mathcal{T}_{20}]^L = \mathcal{T}_{20}^{ij}$
Homo J-couplings	2π	$[\mathcal{A}_{00}]^L = \frac{1}{2\pi}[A_{00}]^L$	$[\mathcal{T}_{00}]^L = T_{00}^{ij}$
Heter DD-couplings	1	$[\mathcal{A}_{2m}]^P = \sqrt{\frac{3}{2}}[A_{2m}]^P$	$[\mathcal{T}_{20}]^L = \frac{1}{\sqrt{6}}(2T_{10}^I T_{10}^S + T_{1-1}^I T_{11}^S + T_{11}^I T_{1-1}^S)$
Heter J-couplings	2π	$[\mathcal{A}_{00}]^L = -\frac{\sqrt{3}}{2\pi}[A_{00}]^L$	$[\mathcal{T}_{00}]^L = -\frac{1}{\sqrt{3}}(2T_{10}^I T_{10}^S - T_{1-1}^I T_{11}^S - T_{11}^I T_{1-1}^S)$

2.5.4 Typical Reference Frames

In this section, the typical reference frames used in solid-state magic angle spinning (MAS) NMR will be defined and described.

1. **Principal axis frame, (PAF or P^{Λ}):** The principal axis frame, P^{Λ}, of a spin interaction Λ is defined as the reference frame where the tensor of the spin interaction is diagonal. Each interaction has its own PAF. In a molecule consisting of several spin sites, there are several P^{Λ} frames.

2. **Molecular frame, (MOL or M):** The molecular frame is fixed with respect to the molecular structure. The molecular frame used to describe the molecular orientation and can be defined arbitrarily.

3. **Crystal frame, (CRS or C):** The crystal frame can be defined as an intermediate or alternative reference frame between the molecular frame M and the rotor frame R. It is fixed to the crystal structure. The crystal axes are defined as: $x = \mathbf{a}/\mid \mathbf{a} \mid$, $y = (\mathbf{b} - \mathbf{b} \cdot x)/\mid (\mathbf{b} - \mathbf{b} \cdot x) \mid$, and $z = x \times y$.

4. **Rotor frame, (ROT or R):** In the rotor frame, its z-axis direction is along the rotational axis of the rotor (see section 2.14). x-axis is along the line from the center towards a point on the rotor wall at which the rotation is optically detected and y-axis is given as $y = z \times x$.

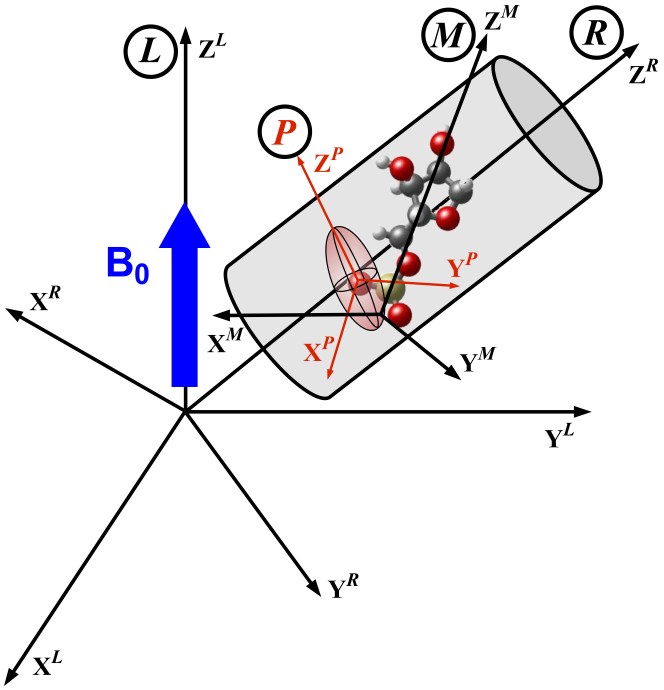

Figure 2.5: Typical reference frames used in solid-state magic angle spinning NMR: laboratory (L), rotor (R), molecular (M) and PAF (P).

5. **Laboratory frame, (LAB or *L*):** In the laboratory frame, the z-axis is aligned in the direction of the external magnetic field $\mathbf{B}_0$. The radiofrequency field is along x-axis in the plane through solenoid coil and $\mathbf{B}_0$. The y-axis is given by $y = z \times x$.

Objects (vectors and tensors) that are expressed in these coordinate systems, are denoted with respective superscripts P, M, C, R, L. The mutual relation of these coordinate frames is illustrated in Fig. 2.5. Using the Wigner matrices [171, 172], a complete transformation of the spin interaction, Λ, from its principal axis frame to the laboratory frame can be accomplished mathematically [175].

2.6 High-Field Approximation

It is necessary to introduce the *secular* or *high-field approximation* before discussing the spin interactions. In NMR by definition, the Zeeman Hamiltonian is much larger than all other spin interactions. Hence, it is possible to treat the other spin interactions as a perturbation to the Zeeman Hamiltonian [168]. The interaction Hamiltonian can be decomposed into terms which commute with the Zeeman interaction and terms which do not commute. In first order only commuting terms need to be taken into account which applies to magnetic fields of a few Tesla to all interactions except the quadrupole interaction, where higher order terms may become important. In terms of spherical tensors, this corresponds to the selection of the spin operators of the form $[T^{\Lambda}_{\lambda 0}]^L$ because these commute with the T_{10} tensor of the Zeeman interaction. Non-commuting terms produce small perturbations of the NMR spectrum called *dynamic frequency shifts* [176]. These effects are small and ignored in this thesis.

2.7 External Spin Interactions

In an NMR experiment, external spin interactions can be expressed as a sum of an external static magnetic field and transverse radio frequency (rf) fields [159, 172] which are controlled by the spectroscopist. The external spin Hamiltonian can be written as:

$$\hat{\mathcal{H}}_{ext} = \hat{\mathcal{H}}^j_Z + \hat{\mathcal{H}}^j_{RF} \tag{2.31}$$

The first term, $\hat{\mathcal{H}}^j_Z$, describes the interaction of the spin system with a strong static field, $\mathbf{B}_0$, the Zeeman interaction, and the second term, $\hat{\mathcal{H}}^j_{RF}$, is the interaction with a transverse oscillating rf, $\mathbf{B}_{RF}$, generated by a coil.

2.7.1 Zeeman Interaction

If a spin system placed into a static magnetic field, the interaction between the spin nuclear magnetic moment and the static field $\mathbf{B}_0$ is called the *Zeeman inter-*

action. Due to the external static field, the degeneracy of the spin states is lifted and a preferential orientation of the nuclear spin along the z-axis of the L frame is induced.

The strong static field along the z direction of the laboratory frame is given as:

$$\mathbf{B}_0 = B_0 \mathbf{e}_z \tag{2.32}$$

The spin Hamiltonian of the Zeeman interaction for an I-spin labelled j can be expressed as:

$$\hat{\mathcal{H}}_Z^j = -\mu_I^j \cdot \mathbf{B}_0 = -\gamma_I^j \hat{\mathbf{I}}^j \mathbf{B}_0 = -\gamma_I^j B_0 \hat{I}_z^j = \omega_0 \hat{I}_z^j \tag{2.33}$$

Here, γ_I^j is the gyromagnetic ratio of the spin I^j, $\hat{I}_z^j$ is the z-component of the spin operator, B_0 is the magnetic field along the z-direction and ω_0 is the Larmor frequency. The Zeeman Hamiltonian can be written in terms of ISTOs as follows:

$$\hat{\mathcal{H}}_Z^j = [A_{00}^Z] T_{10}^j = \omega_0 T_{10}^j \tag{2.34}$$

2.7.2 Interaction with the Radio Frequency Field

Using an rf pulse, the longitudinal magnetization is rotated by 90° to the transverse plane. In the NMR spectrometer, the rf coil along the x-axis of the laboratory frame generates an rf field $\mathbf{B}_{RF}$. The magnitude of this rf field oscillates at the reference frequency ω_{ref} during the rf pulse. The rf field for a perfect rectangular pulse can be expressed as:

$$\mathbf{B}_{RF}(t) = \begin{cases} B_{RF} \cos(\omega_{ref} t + \phi_p) \mathbf{e}_x & \text{during an rf pulse} \\ 0 & \text{otherwise} \end{cases} \tag{2.35}$$

where B_{RF} and ϕ_p are the amplitude and the phase of the rf pulse, respectively. It is convenient to decompose the oscillatory field into a sum of two rotating components with the same frequency but opposite direction. The component that rotates in the same sense as the spin precession (positive for spins with $\gamma < 0$ and negative for spins with $\gamma > 0$) is called the *resonant component* of the rf field. The component rotating in the opposite sense to the Larmor frequency is the *non-resonant* rf field component. In good approximation, if on-resonance i.e. $\omega_{ref} \approx \omega_0$, the non-resonant component can be neglected. Thus, only the resonant part has an influence on the nuclear spin. The transverse part of the spin Hamiltonian resulting from the interaction between the resonant component of the rf field and the nuclear spin can be written as:

$$\hat{\mathcal{H}}_{RF}^j(t) = -\frac{1}{2} \gamma_I^j B_{RF} \{\sin(\omega_{ref} t + \phi_p) \hat{I}_y^j\} \tag{2.36}$$

Since the spin Hamiltonian is time-dependent in the above equation, it is useful to express the spin Hamiltonian in the rotating frame. Thus, the spin

Hamiltonian appears to be time-independent. The rf Hamiltonian expressed in the rotating frame as:

$$\hat{\mathcal{H}}^j_{RF}(t) = \omega^j_{nut}(\hat{I}^j_x \cos\phi_p + \hat{I}^j_y \sin\phi_p) \tag{2.37}$$

where ω^j_{nut} is called *nutation frequency* of the rf field, $\omega^j_{nut} = 1/2\,|\gamma^j_I B_{RF}|$ which measures the rf field amplitude.

Pulse

The rf pulse can be defined by a *flip angle* β_p and a *phase* ϕ_p. When the rf pulse is applied, the spin polarization is rotated according to the flip angle which is given by:

$$\beta_p = \omega_{nut}\tau_p \tag{2.38}$$

It is proportional to the rf pulse amplitude, through the factor ω_{nut} and proportional to the τ_p i.e. pulse duration. Long and weak pulses are more frequency-selective whilst short and strong pulses excite a wide range of frequencies. The effect of the flip angle and the phase of the rf pulse on the spin magnetization of an isolated spin in a strong static magnetic field is shown in Fig. 2.6.

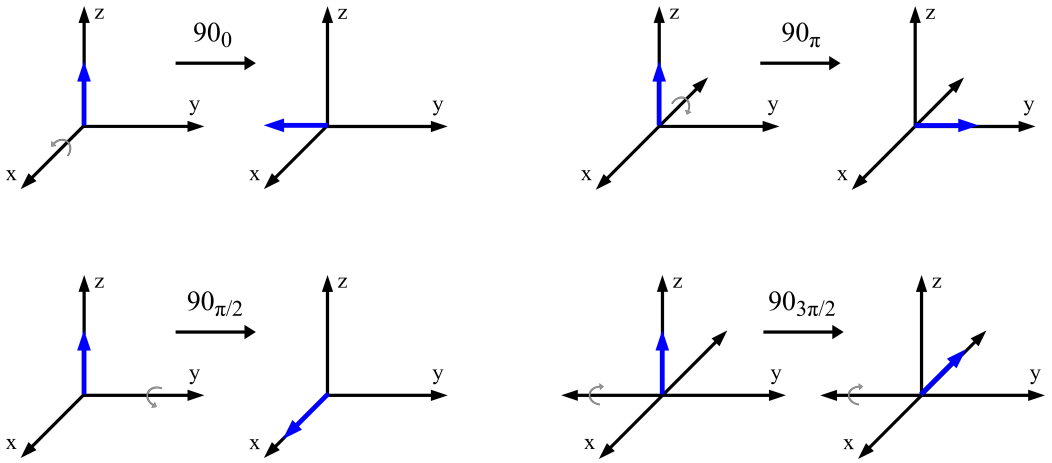

Figure 2.6: The effect of an rf pulse with flip angle 90° and different phases (0, $\pi/2$, π, and $3\pi/2$) on the spin magnetization. In the NMR jargon, these four pulses are known as x, y, -x/$\bar{x}$ and -y/$\bar{y}$-pulse, respectively.

2.8 Internal Spin Interactions

The nuclei are surrounded by magnetic and electric fields originating from the sample itself. The nuclear spin interaction with these fields can be expressed by

an internal Hamiltonian $\hat{\mathcal{H}}_{int}$ [158]. The internal Hamiltonian contains the following terms: *chemical shift interaction*, *direct dipole-dipole couplings*, *J-couplings*, and *quadrupolar interaction*, in the case of diamagnetic solids. The quadrupolar interaction only appears for nuclei with spin $> 1/2$, which is an interaction with an electric field.

$$\hat{\mathcal{H}}_{int} = \hat{\mathcal{H}}^j_{CS} + \hat{\mathcal{H}}^{ij}_{DD} + \hat{\mathcal{H}}^{ij}_{J} + \hat{\mathcal{H}}^j_{Q} + ... \tag{2.39}$$

2.8.1 Chemical Shift Interaction

An external magnetic field ($\mathbf{B}_0$) induces currents in the electron clouds in the molecule. The circulation of this current generates a magnetic field called an *induced magnetic field* ($\mathbf{B}^j_{induced}$). The nuclear spins experience the sum of these two fields which can be expressed as a *local magnetic field* ($\mathbf{B}^j_{local}$):

$$\mathbf{B}^j_{local} = \mathbf{B}_0 + \mathbf{B}^j_{induced} \tag{2.40}$$

Even though the induced field is very small compared to the static field $\mathbf{B}_0$, it causes measurable shifts in the spin precession frequencies. The new Larmor frequency is called the *chemically shifted Larmor frequency* [158].

The induced field is linearly dependent on the applied magnetic field $\mathbf{B}_0$ and can be expressed as:

$$\mathbf{B}^j_{induced} = \boldsymbol{\delta}^j \mathbf{B}_0 \tag{2.41}$$

The symbol $\boldsymbol{\delta}^j$ is a 3×3 matrix called the *chemical shift (or shielding) tensor* (CS) of the spin j. The chemical shift tensor is a rank-2 tensor. The values of the chemical shift are given on a deshielding scale [172, 177–180].

Assuming the applied static magnetic field B_0 is along the z-axis of the laboratory frame, the induced magnetic field in a matrix-vector form can be written as:

$$\begin{pmatrix} B^{j,x}_{induced} \\ B^{j,y}_{induced} \\ B^{j,z}_{induced} \end{pmatrix} = \begin{pmatrix} \delta^j_{xx} & \delta^j_{xy} & \delta^j_{xz} \\ \delta^j_{yx} & \delta^j_{yy} & \delta^j_{yz} \\ \delta^j_{zx} & \delta^j_{zy} & \delta^j_{zz} \end{pmatrix} \cdot \begin{pmatrix} 0 \\ 0 \\ B_0 \end{pmatrix} \tag{2.42}$$

$$\begin{pmatrix} B^{j,x}_{induced} \\ B^{j,y}_{induced} \\ B^{j,z}_{induced} \end{pmatrix} = \begin{pmatrix} \delta^j_{xz} B_0 \\ \delta^j_{yz} B_0 \\ \delta^j_{zz} B_0 \end{pmatrix} \tag{2.43}$$

The induced magnetic field has a component not only along the z-direction of the L frame but also along the x-direction and the y-direction, as the electronic distribution is not spherical around the nuclei.

The full form of the chemical shift Hamiltonian of spin I^j is given by:

$$\begin{aligned} \hat{\mathcal{H}}^j_{CS} &= -\boldsymbol{\mu}^j_I \cdot \mathbf{B}^j_{induced} \\ &= -\gamma^j_I \delta^j_{xz} \mathbf{B}_0 \hat{I}^j_x - \gamma^j_I \delta^j_{yz} \mathbf{B}_0 \hat{I}^j_y - \gamma^j_I \delta^j_{zz} \mathbf{B}_0 \hat{I}^j_z \end{aligned} \tag{2.44}$$

In the secular approximation, only the last term of the equation 2.44 is retained. Thus, the secular chemical shift Hamiltonian is given as:

$$\hat{\mathcal{H}}_{CS}^{j} \cong -\gamma_I^j \delta_{zz}^j \mathbf{B}_0 \hat{I}_z^j \tag{2.45}$$

The CS tensor can be decomposed into three irreducible tensors of rank-0, rank-1, and rank-2:

$$\boldsymbol{\delta}^j = \delta_{iso}^j + \delta_{asymm}^j + \delta_{anisotropy}^j \tag{2.46}$$

Here, the δ_{iso}^j is called the *isotropic chemical shift*. It is a rank-0 tensor, equals to the trace of the CS tensor and a scalar quantity:

$$\begin{aligned} \delta_{iso}^j &= \frac{1}{3} Tr(\boldsymbol{\delta}^j) \\ &= \frac{1}{3}(\delta_{xx}^j + \delta_{yy}^j + \delta_{zz}^j) \end{aligned} \tag{2.47}$$

The term δ_{asymm}^j is a rank-1 tensor and can be ignored under the secular approximation because it has no secular part. The $\delta_{anisotropy}^j$ is a rank-2 tensor called the *chemical shift anisotropy* (CSA). The chemical shift anisotropy plays an important role in order to gain useful information about the geometry and the orientation of the electronic distribution around the nucleus. Three diagonal elements of the matrix $\boldsymbol{\delta}^j$ are known as the *principal values of the CSA tensor* and denoted by δ_{xx}^P, δ_{yy}^P, δ_{zz}^P. The chemical shift tensor is *isotropic* if all three principal values are equal. If two or more principal values of the chemical shift tensor are different, then the chemical shift tensor is *anisotropic*. The CSA quantifies the deviation from isotropy.

The three principal values are ordered as follows by using the Haeberlen-Mehring-Spiess convention [172, 177, 178]:

$$|\delta_{zz}^p - \delta_{iso}^j| \geq |\delta_{xx}^p - \delta_{iso}^j| \geq |\delta_{yy}^p - \delta_{iso}^j| \tag{2.48}$$

The *chemical shift anisotropy parameter* (δ_{aniso}) can be explained as the largest deviation in chemical shift from the isotropic value:

$$\delta_{aniso} = \delta_{zz}^P - \delta_{iso}^j \tag{2.49}$$

The difference between the other two principal values is quantified by a parameter which is denoted by η, known as the *asymmetry parameter*. It is defined as follows:

$$\eta = \frac{\delta_{yy}^P - \delta_{xx}^P}{\delta_{zz}^P - \delta_{iso}^j}, \quad (0 \leq \eta \leq 1) \tag{2.50}$$

and the CSA frequency is given by:

$$\omega_{aniso}^j = \omega_{ref} \delta_{aniso}^j \tag{2.51}$$

Normally, the Zeeman and CS Hamiltonian are expressed together. This Hamiltonian expressed in terms of ISTOs becomes:

$$\hat{\mathcal{H}}^j_{CS} = \omega^j_0 T^j_{10} + \sum_{m=-2}^{2} \omega^j_{aniso} [\mathcal{A}^j_{2m}]^L [\mathcal{T}^j_{10}] \tag{2.52}$$

The CS is indispensable in study of the spectral assignment of spin sites [54], molecular orientation [128] and mobility of molecular groups [31]. For more details on the CSA tensor and its relation to the point group symmetry see section 2.9.

2.8.1.1 Chemical Shift Scale

In the chemical shift (δ) scale, the sample frequency (ν_{sample}) is referenced to the resonance frequency of a standard reference sample (ν_{ref}) instead of the Larmor frequency [54]. The chemical shift is often used instead of chemical shielding (σ) and given as per IUPAC conventions [54, 179–181]:

$$\delta/ppm = \frac{\nu_{sample} - \nu_{ref}}{\nu_{ref}} \times 10^6 \tag{2.53}$$

The relationship between the chemical shift and the chemical shielding scale can be obtained by reversing the sign as follows:

$$\delta = -\sigma \tag{2.54}$$

The SIMPSON program [156,157] uses the Haeberlen-Mehring-Spiess convention [172, 177, 178]:

for $\delta_{aniso} > 0$ (i.e. $\delta^P_{zz} = \delta_{11}$)	for $\delta_{aniso} < 0$ (i.e. $\delta^P_{zz} = \delta_{33}$)
$\delta_{11} = \delta_{iso} + \delta_{aniso}$	$\delta_{33} = \delta_{iso} + \delta_{aniso}$
$\delta_{22} = \delta_{iso} - \delta_{aniso}\frac{(1-\eta)}{2}$	$\delta_{22} = \delta_{iso} - \delta_{aniso}\frac{(1-\eta)}{2}$
$\delta_{33} = \delta_{iso} - \delta_{aniso}\frac{(1+\eta)}{2}$	$\delta_{11} = \delta_{iso} - \delta_{aniso}\frac{(1+\eta)}{2}$

If $\delta_{aniso} > 0$, then the nucleus is said to be deshielded relative to the reference, and if $\delta_{aniso} < 0$, the nucleus is set to be shielded. The tensor components of chemical shifts are ordered according to $\delta_{11} \geq \delta_{22} \geq \delta_{33}$.

2.8.2 Direct Dipole-Dipole Coupling

Each nuclear spin, for $I > 0$, is magnetic and generates a magnetic field. A second nuclear spin in the surrounding interacts with this magnetic field. As this interaction is mutual, the first spin also interacts with the magnetic field generated

by the second spin. This interaction between spins is called the *direct dipole-dipole coupling or through-space dipole-dipole coupling*, since the fields between the nuclear spins propagated through the space. Other known terms for this interaction are the *dipole-dipole coupling* or the *DD-coupling*.

For the two spins I^i and I^j the spin Hamiltonian of the dipole-dipole coupling can be defined as:

$$\hat{\mathcal{H}}_{DD}^{ij} = \hat{\mathbf{I}}^i \, \mathbb{D} \, \hat{\mathbf{I}}^j \tag{2.55}$$

In the case of dipolar interaction, the tensor $\mathbb{D}$ in the above equation is axially symmetric with zero trace ($Tr\{\mathbb{D}\} = 0$) [172]. The full form of the direct dipole-dipole interaction in the spin Hamiltonian is given as :

$$\hat{\mathcal{H}}_{DD}^{ij} = b_{ij} \left(3(\hat{\mathbf{I}}^i \cdot \mathbf{e}_{ij})(\hat{\mathbf{I}}^j \cdot \mathbf{e}_{ij}) - \hat{\mathbf{I}}^i \cdot \hat{\mathbf{I}}^j \right) \tag{2.56}$$

where $\mathbf{e}_{ij}$ is a unit vector parallel to line joining the centers of the two nuclei (see Fig. 2.7).

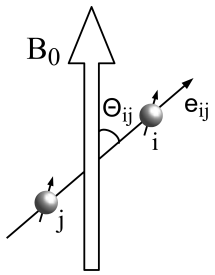

Figure 2.7: An angle Θ_{ij} between the the internuclear vector $\mathbf{e}_{ij}$ (between the spins I^i and I^j) and an external static magnetic field $\mathbf{B_0}$.

If the spins are of the same isotopic species i.e. *homonuclear case*, the secular approximation of the homonuclear dipole-dipole spin Hamiltonian can be written as:

$$\hat{\mathcal{H}}_{DD}^{ij} = b_{ij} \tfrac{1}{2} (3\cos^2\Theta_{ij} - 1)(3\hat{I}_z^i \, \hat{I}_z^j - \hat{\mathbf{I}}^i \cdot \hat{\mathbf{I}}^j) \tag{2.57}$$

Here, Θ_{ij} is the angle between the dipolar vector and the static field (see Fig. 2.7) and b_{ij} is the *dipole-dipole coupling constant* and given by:

$$b_{ij} = -\frac{\mu_0}{4\pi} \frac{\gamma^i \gamma^j \hbar}{r_{ij}^3}, \tag{2.58}$$

where γ^i and γ^j are the gyromagnetic ratios of the two spins and r_{ij} is the spin-spin distance between two spins.

The dipole-dipole interaction depends on the gyromagnetic ratio of the nuclei and the inverse cube of the internuclear distance. This property is useful for the internuclear distance and hence the geometrical form of the molecule from solid-state NMR experiments [158, 182]. Even though the b_{ij} (DD coupling constant)

is constant and does not depend on molecular orientation, but the dipole-dipole spin Hamiltonian depends on the orientation [158].

In the secular approximation, the homonuclear dipole-dipole Hamiltonian in terms of ISTOs in the laboratory frame can be given as:

$$\hat{\mathcal{H}}_{DD}^{ij} = [A_{20}^{DD}]^L [T_{20}^{DD}]^L \tag{2.59}$$

Similarly, the heteronuclear dipole-dipole Hamiltonian in the secular approximation can be written as:

$$\hat{\mathcal{H}}_{DD}^{ij} = b_{ij}(3\cos^2\Theta_{ij} - 1)\hat{I}_z^i \, \hat{I}_z^j = [A_{20}^{DD}]^L [T_{10}^{I^i}]^L [T_{10}^{I^j}]^L \tag{2.60}$$

In the above equations, the first term $[A_{20}^{DD}]^L$ is the spatial part, which depends on the angle Θ and the second terms, $[T_{20}^{DD}]^L$,$[T_{10}^{I^i}]^L$,and $[T_{10}^{I^j}]^L$ are the spin parts (see Appendix A and [183]).

2.8.3 *J*-Coupling

Different atoms in a molecule are chemically bonded with each other. The nuclear spins of chemically bonded atoms are coupled by the spin of the bonding electrons. This indirect coupling interaction is called the *J-coupling*, *indirect spin-spin coupling*, or *indirect dipole-dipole coupling*, which is useful for the determination of chemical structure and study of bonding between two atoms [184, 185]. It is usually represented by the symbol J.

The form of the spin Hamiltonian for J-coupling interaction between spins I^i and I^j is given as [172]:

$$\hat{\mathcal{H}}_J^{ij} = \hat{\mathbf{I}}^i \, \mathbb{J} \, \hat{\mathbf{I}}^j \tag{2.61}$$

where $\mathbb{J}$ is the J-coupling tensor and a 3×3 real matrix. $\hat{\mathbf{I}}^i$ and $\hat{\mathbf{I}}^j$ are the spin operators for spins i and j, respectively. The tensor $\mathbb{J}$ can be decomposed into irreducible tensors of rank-0 ($J^{(0)}$), rank-1 ($J^{(1)}$), and rank-2 ($J^{(2)}$). The tensor $J^{(0)}$ is the isotropic part of the $\mathbb{J}$ tensor and its spin Hamiltonian is given by:

$$\hat{\mathcal{H}}_{J_{iso}}^{ij} = 2\pi J_{iso}^{ij} \hat{\mathbf{I}}^i \cdot \hat{\mathbf{I}}^j \tag{2.62}$$

The term J_{iso}^{ij} is called the *isotropic J-coupling* constant and given in units of Hz. It is equal to the average of the diagonal elements of the J-coupling tensor given as:

$$J_{iso}^{ij} = \tfrac{1}{3}(J_{xx}^{ij} + J_{yy}^{ij} + J_{zz}^{ij}) \tag{2.63}$$

The tensor $J^{(1)}$ is the antisymmetric part of the $\mathbb{J}$ tensor and can be ignored to the first order [172]. The rank-2 part of the $\mathbb{J}$ tensor represents the orientation dependence of the J-coupling. Under rotations, the irreducible tensor for the anisotropic part of the J-coupling has the same rotational behavior and form

as the usually much larger DD coupling, thus this rank-2 tensor is difficult to measure separately from the DD interaction [158, 183].

The isotropic form of J-coupling Hamiltonian in terms of ISTOs can be given by (for details see Appendix A):

$$\hat{\mathcal{H}}^{ij}_{J_{iso}} = [A^J_{00}]^L [T^{ij}_{00}]^L \tag{2.64}$$

2.8.4 Quadrupolar Interaction

For a spin $I^j \geq 1$, the electric charge distribution of the nucleus is not spherically symmetric. Hence, the interaction energy of quadrupolar nuclei with an electric field gradients from the surrounding electrons depends on the nuclear orientation. The basic form of quadrupolar Hamiltonian which describes the interaction between a nuclear electric quadrupole moment and the electric field gradient in angular frequency units can be expressed as [13]:

$$\hat{\mathcal{H}}^j_Q = \frac{eQ_j}{2I^j(2I^j-1)\hbar}\,\hat{\mathbf{I}}^j\,\mathbb{V}\,\hat{\mathbf{I}}^j \tag{2.65}$$

If the interaction is small compared to $\hat{\mathcal{H}}_z$, secular approximation can be used and the quadrupolar Hamiltonian in natural units is given as [158]:

$$\hat{\mathcal{H}}^j_Q = \frac{3eQ_j}{4I^j(2I^j-1)}\,V^j_{zz}\left(3(\hat{I}^j_z)^2 - \hat{\mathbf{I}}^j\cdot\hat{\mathbf{I}}^j\right) \tag{2.66}$$

where e is the proton charge, $\mathbb{V}$ is the second-rank tensor that describes the electric field gradient, eQ_j is the nuclear quadrupole moment of the nucleus I^j, and V^j_{zz} is the electric field gradient term that depends on the molecular orientation. In some cases, the high-field approximation is not applicable to the quadrupolar Hamiltonian and more terms are necessary [186, 187].

The quadrupolar interaction can be described, similar to the CSA interaction, by its anisotropy. In its principal axis frame (P), only diagonal elements ($|V^P_{xx}| \geq |V^P_{yy}| \geq |V^P_{zz}| = eq$) are non-zero. The quadrupole coupling constant, C_Q, (in units of Hz) and the asymmetry parameter, η_Q, are defined from the principal values as below:

$$C_Q = \frac{eQ_jV^P_{zz}}{h} = \frac{e^2qQ_j}{h} \tag{2.67}$$

$$\eta_Q = \frac{V^P_{xx}-V^P_{yy}}{V^P_{zz}}, \qquad (0 \leq \eta_Q \leq 1) \tag{2.68}$$

where C_Q measures the strength of the quadrupolar interaction.

In case of quadrupolar nuclei with half-integer spins ($I = \frac{3}{2}, \frac{5}{5}...$), there are two kinds of possible transitions namely *central* ($-\frac{1}{2} \leftrightarrow \frac{1}{2}$) and *satellite* transitions ($m \leftrightarrow (m \pm 1)$). The only central transition is allowed by the selection rule, $\Delta_m = \pm 1$. For further reading about NMR of quadrupolar nuclei see [186, 188–190].

2.9 Chemical Shift Tensor and Point Group Symmetry Relation

There is a close mutual relationship between symmetry considerations and NMR spectroscopy [73, 74, 191, 192]. The symmetry properties of second-rank tensors are described by using group theoretical methods originally utilized for crystallographic purposes [193]. These methods have been used in NMR for the chemical shift tensor description [73, 192, 194], as well as, depending on the different point group symmetries at the observed nuclei, the minimum number of chemical shift tensor components are determined [73, 192]. A few symmetry properties of the chemical shift tensor are shown in Fig. 2.8.

In a molecule, the presence of a C_n or S_n axis ($n \geq 3$) at nuclear site ensures axial symmetry of the electronic environment of the nucleus. As a consequence, the asymmetry parameter is reduced to zero i.e. $\eta = 0$ (Fig. 2.8), as for example for the tensor of ^{13}C in $^{13}CH_4$. The anisotropy vanishes i.e. $\delta_{aniso} = 0$, if two or more such axes intersect at the nuclear site. Hence, in such cases the shielding is isotropic and only depends on the scalar quantity, δ_{iso}, as for example for the tensor of ^{13}C in $^{13}CH_4$. Similarly, this occurs for all atoms and ions with spherical symmetry (for example ^{3}He and $^{19}F^-$).

Anet and O'Leary [191] have phrased simple rules which help to derive the directions of the *principal axes* of the chemical shift tensor depending on the site symmetry.

1. "If both the anisotropy (δ_{aniso}) and the asymmetry parameter (η) are zero, the principal axes of chemical shift tensor can be chosen arbitrarily because the shielding is isotropic" as shown in Fig. 2.8 (left).

2. "If only $\eta = 0$, one principal coordinate axis must be parallel to the C_n or S_n ($n \geq 3$) axis that is present at the nuclear site, and as a result of axial symmetry, the orientation of the other two axes can be chosen arbitrarily" (Fig. 2.8, middle).

3. "If δ_{aniso} and η are both non-zero, the principal axes must be determined with respect to arbitrary axes, except that any local C_2 axis, or the normal two any local plane of symmetry, must have principal coordinate axis parallel to it".

Moreover, in the case of D_2 or $C_{2\nu}$ site point group symmetry, where more than one C_2 axis or more than one plane of symmetry is present, all three principal coordinate axes are determined by symmetry as shown in Fig. 2.8 (right).

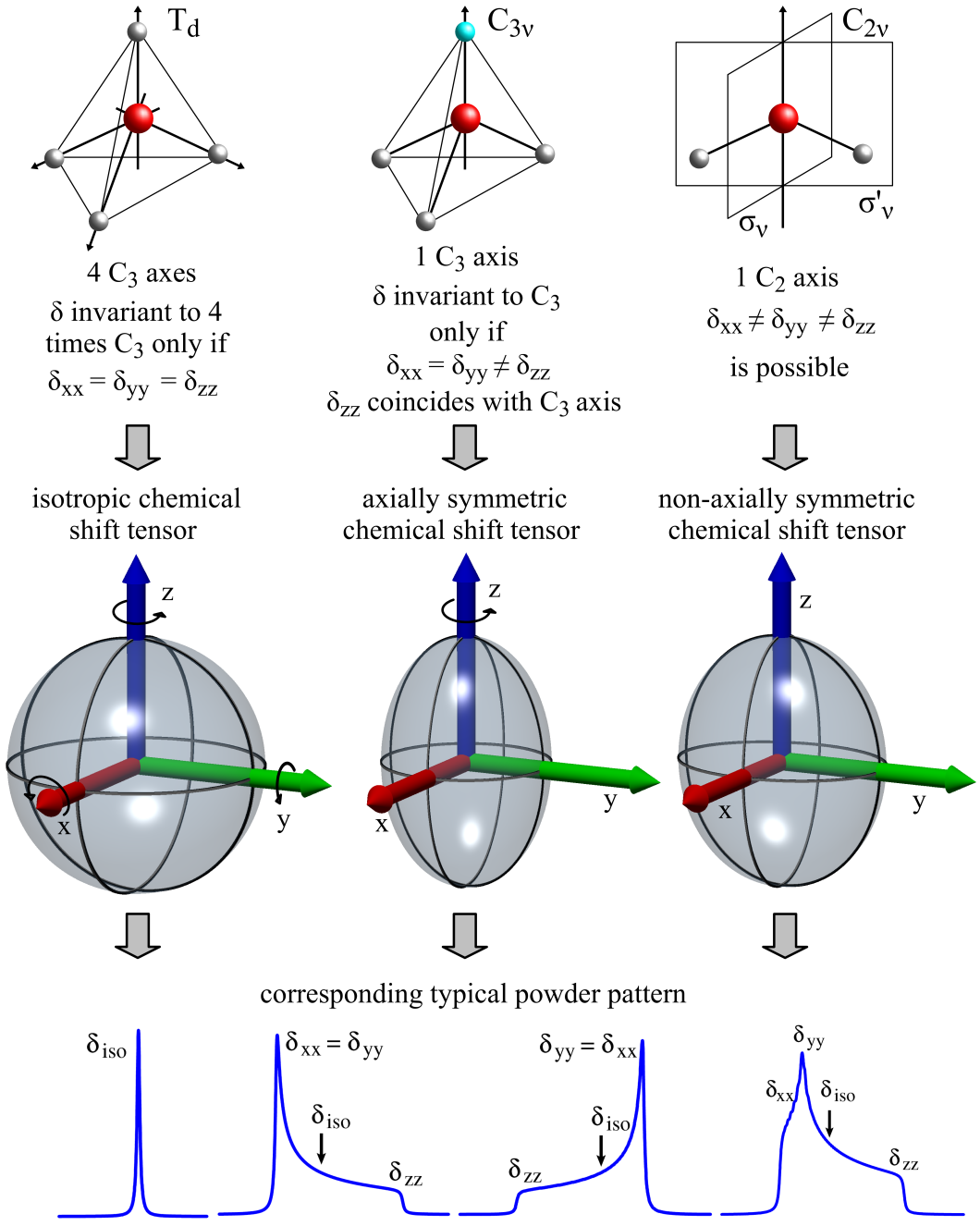

Figure 2.8: Pictorial representation for the relation between the point group symmetry and the chemical shift tensors, adopted from Klaus *et al.* ([192], Fig. 1). Illustrative examples namely the T_d (left), $C_{3\nu}$ (middle), and $C_{2\nu}$ (right) point group symmetries are shown with their chemical shift tensors and corresponding powder spectra.

2.10 Density Operator

A collection of independent and identical spin systems in the sample is called an *ensemble*. The total nuclear magnetization is the sum of small contributions from the individual spins. In principle it is possible to treat each spin individually and calculate the total magnetization by adding their results. In reality such calculations are impractical. However, there is an elegant alternative method called the *density operator* to calculate the overall spin state of a spin ensemble without referring to the individual spin states.

A single spin in a superposition state with coefficients C_α and C_β can be written as:

$$|\psi\rangle = \begin{pmatrix} C_\alpha \\ C_\beta \end{pmatrix} \tag{2.69}$$

The expectation value of an operator $\hat{Q}$ for a single spin is given by:

$$\langle \hat{Q} \rangle = \langle \psi | \hat{Q} | \psi \rangle \tag{2.70}$$

Similarly consider an ensemble of N spins in a superposition state $|\psi_k(t)\rangle$. The result is the average outcome of many measurements which is the sum of all expectation values and given by [158]:

$$\langle \overline{Q_{obs}} \rangle = \sum_{k=1}^{N} \langle \psi_k(t) | \hat{Q} | \psi_k(t) \rangle \tag{2.71}$$

The density operator $\hat{\rho}(t)$ is defined as:

$$\hat{\rho}(t) = \overline{|\psi_k(t)\rangle\langle\psi_k(t)|} \tag{2.72}$$

here the overbar indicates the average over the N spins of the ensemble. The macroscopic observation of Q for the entire ensemble of spins is given by:

$$\overline{\langle Q \rangle} = Tr\{\hat{\rho}(t)\hat{Q}\} \tag{2.73}$$

Consider an ensemble of non-interacting spins-1/2, the matrix representation of the density operator is given by:

$$\hat{\rho} = \begin{pmatrix} \rho_{\alpha\alpha} & \rho_{\alpha\beta} \\ \rho_{\beta\alpha} & \rho_{\beta\beta} \end{pmatrix} \tag{2.74}$$

The diagonal elements $\rho_{\alpha\alpha}$ and $\rho_{\beta\beta}$ of the density matrix operators are known as *populations* of states $|\alpha\rangle$ and $|\beta\rangle$. The off-diagonal elements $\rho_{\alpha\beta}$ and $\rho_{\beta\alpha}$ are known as *coherences* of states $|\alpha\rangle$ and $|\beta\rangle$.

Consider a coherence ρrs between two energy eigenstates $|r\rangle$ and $|s\rangle$. The density operator in the Zeeman basis can be expressed as [158, 183]:

$$\hat{\rho}(t) = \sum_{r,s} \rho_{rs}(t)|r\rangle\langle s| \tag{2.75}$$

If the spin states $|r\rangle$ and $|s\rangle$ with eigenstates of $\hat{I}_z$ and eigenvalues equal to M_r and M_s, the coherence order (p) between eigenstates $|r\rangle$ and $|s\rangle$ is given by

$$p_{rs} = M_r - M_s \tag{2.76}$$

Consider a spin system which is left undisturbed for a long time in a strong magnetic field in contact with the molecular surroundings. After a time, the system reaches a state where it is in *thermal equilibrium* with the surrounding. At this state, the density matrix can be described by using the *Boltzmann distribution* [158]:

$$\hat{\rho}^{eq} \cong \tfrac{1}{2}\left(\hat{\mathbf{1}} + \mathbb{B}\hat{I}_z\right) \tag{2.77}$$

Here $\hat{\mathbf{1}}$ is the unity operator and $\mathbb{B}$ is a Boltzmann factor, defined as:

$$\mathbb{B} = \frac{\hbar\gamma_I B_0}{k_B T} \tag{2.78}$$

As $\hat{\mathbf{1}}$ commutes with all Hamiltonians, only the term $\hat{I}_z$ is considered in the calculations.

The evolution of the density operator under the effect of Hamiltonian $\hat{\mathcal{H}}(t)$ can be given by:

$$\frac{d\hat{\rho}(t)}{dt} = i\left[\hat{\mathcal{H}}(t), \hat{\rho}(t)\right] \tag{2.79}$$

This equation is derived from the time-dependent *Schrödinger* equation and known as the *Liouville-Von Neumann* equation. The solution of above equation for evolution under a time-independent Hamiltonian is:

$$\hat{\rho}\,(t) = e^{-i\hat{\mathcal{H}}(t-t_0)}\,\hat{\rho}\,(t_0)\,e^{i\hat{\mathcal{H}}(t-t_0)} \tag{2.80}$$

where $\hat{\rho}(t)$ is the density operator at time t and $\hat{\rho}(t_0)$ at time $t_0 = 0$. The term $e^{-i\hat{\mathcal{H}}(t-t_0)}$ defines the *propagator* operator $U(t, t_0)$ associated to the Hamiltonian $\hat{\mathcal{H}}$ as:

$$U\,(t, t_0) = e^{-i\hat{\mathcal{H}}(t-t_0)} \tag{2.81}$$

If the Hamiltonian is time-independent, using the propagator operator U, equation 2.80 becomes:

$$\rho\,(t) = U\,(t, t_0)\,\rho(t_0)U^{\dagger}\,(t, t_0) \tag{2.82}$$

For a time-dependent Hamiltonian, the propagator operator U is defined as:

$$U\,(t, t_0) = \hat{T}e^{-i\int_{t_o}^{t}\hat{\mathcal{H}}(t')dt'} \tag{2.83}$$

where $\hat{T}$ is the *Dyson time-ordering* operator [13, 161, 169, 183, 195].

2.11 Carousel Averaging of Single-Crystal

In general single-crystal spectra under MAS are dispersive in nature. The lineshape of each spinning sideband of single-crystal spectra has an arbitrary phase [173, 196]. In single-crystal MAS NMR, the signal phase is important as it provides information about chemical shift tensor orientation. In 1989, Levitt has shown that a powdered sample under uniform distribution of spins generates an absorptive spectrum by investigating the average signal of a carousel for a single-crystal [197]. This concept of signal averaging could be applied to a single-crystal for determining the correct signal phase or phase reference in single-crystal MAS NMR.

Consider a complete rotation of a single-crystal from 0 to 2π as a carousel. The total signal intensity of a spectrum can be obtained from the summation of signal contributions from all points on the carousel. If these points (N) on the carousel are distinguished by the variable α_{RL}, where α_{RL} runs from 0 to 2π, the resonance frequency ω is given as a function of time t:

$$\omega(t;\alpha_{RL}) = \omega(\omega_r t + \alpha_{RL}) \tag{2.84}$$

Here, ω_r is the sample rotation frequency. This equation indicates that all α_{RL} on the carousel experience the same sets of resonance frequencies, but at shifted times. The signal contribution from each α_{RL} is obtained by assuming that the single quantum coherences in each α_{RL} are prepared with the same phase ϕ_0 at time $t = 0$, and is proportional to:

$$S(t;\alpha_{RL}) = \exp\{i\Phi(t,0;\alpha_{RL}) + \phi_0\} \tag{2.85}$$

where

$$\Phi(t_1,t_2;\alpha_{RL}) = \int_{t_1}^{t_2} \omega(t;\alpha_{RL})\, dt \tag{2.86}$$

Here Φ is the integrated phase accumulated by the coherences between times t_1 and t_2 as the α_{RL} travels around the carousel. Each signal component of the α_{RL} may be expanded as a set of sidebands (n):

$$S(t;\alpha_{RL}) = \exp(i\Phi_0) \sum_n a_n(\alpha_{RL}) \exp\{i(\omega_C + n\omega_r)t\} \tag{2.87}$$

where n is the sideband order of the signal contribution for the α_{RL}. ω_C is the isotropic chemical shift frequency independent of α_{RL}. The generated complex sideband intensities a_n are in general functions of α_{RL} and have arbitrary phase. The total signal intensity can be obtained by averaging over the N uniform distributions of α_{RL} and proportional to:

$$\overline{S(t)} = \exp(i\Phi_0) \sum_N \sum_n \overline{a_n} \exp\{i(\omega_C + n\omega_r)t\} \tag{2.88}$$

where $\overline{a_n}$ is the total sideband intensity provided by the entire carousel of N uniform distributions of α_{RL} and $\alpha_{RL} \in \{0, \frac{360^\circ}{N}, ..., (360^\circ - \frac{360^\circ}{N})\}$.
Using the following symmetry of the integrated phase Φ:

$$\Phi(t_2, t_1; \alpha_{RL}) = \Phi(t_2 + \tfrac{\alpha_{RL}}{\omega_r}, t_1 + \tfrac{\alpha_{RL}}{\omega_r}; 0) \tag{2.89}$$

it is demonstrated from equations 2.84 and 2.86 that:

$$\Phi(t, 0; \alpha_{RL}) = \Phi(t + \tfrac{\alpha_{RL}}{\omega_r}, 0; 0) - \Phi(\tfrac{\alpha_{RL}}{\omega_r}, 0; 0) \tag{2.90}$$

and therefore:

$$S(t; \alpha_{RL}) = \exp(i\Phi_0) S(t + \tfrac{\alpha_{RL}}{\omega_r}; 0) S(\tfrac{\alpha_{RL}}{\omega_r}; 0)^* \tag{2.91}$$

Using equation 2.87, both sides of this expression are expanded and the coefficients of $\exp\{i(\omega_0 + n\omega_r)t\}$ are equated. The result is expressed as:

$$a_n(\alpha_{RL}) = \sum_{n'} a_n(0) a_{n'}(0)^* \exp\{i(n - n')\alpha_{RL}\} \tag{2.92}$$

Averaging over α_{RL} on the both sides results in:

$$\overline{a_n} = |a_n(0)|^2 \tag{2.93}$$

where $\overline{a_n}$ is real and positive. Thus the sideband intensities provided by the entire carousel of N uniform distributions of α_{RL} are real and positive.

Fig. 2.9 represents this averaging process using $N = 10$ uniform distributions of α_{RL} for single-crystal MAS NMR spectra. Numerical simulations of single-crystal MAS spectra are shown in (a)-(j), with orientations corresponding to different positions on the same "carousel" with a mixture of absorptive and dispersive spinning sidebands. The sum of signal contributions from all 10 positions of α_{RL} on the carousel is shown in Fig. 2.9 (bottom). The resultant spectrum shows positive absorptive sidebands. Moreover, equation 2.93 shows that the sideband intensities generated by the entire carousel can be derived from the sideband intensities generated by a single α_{RL}.

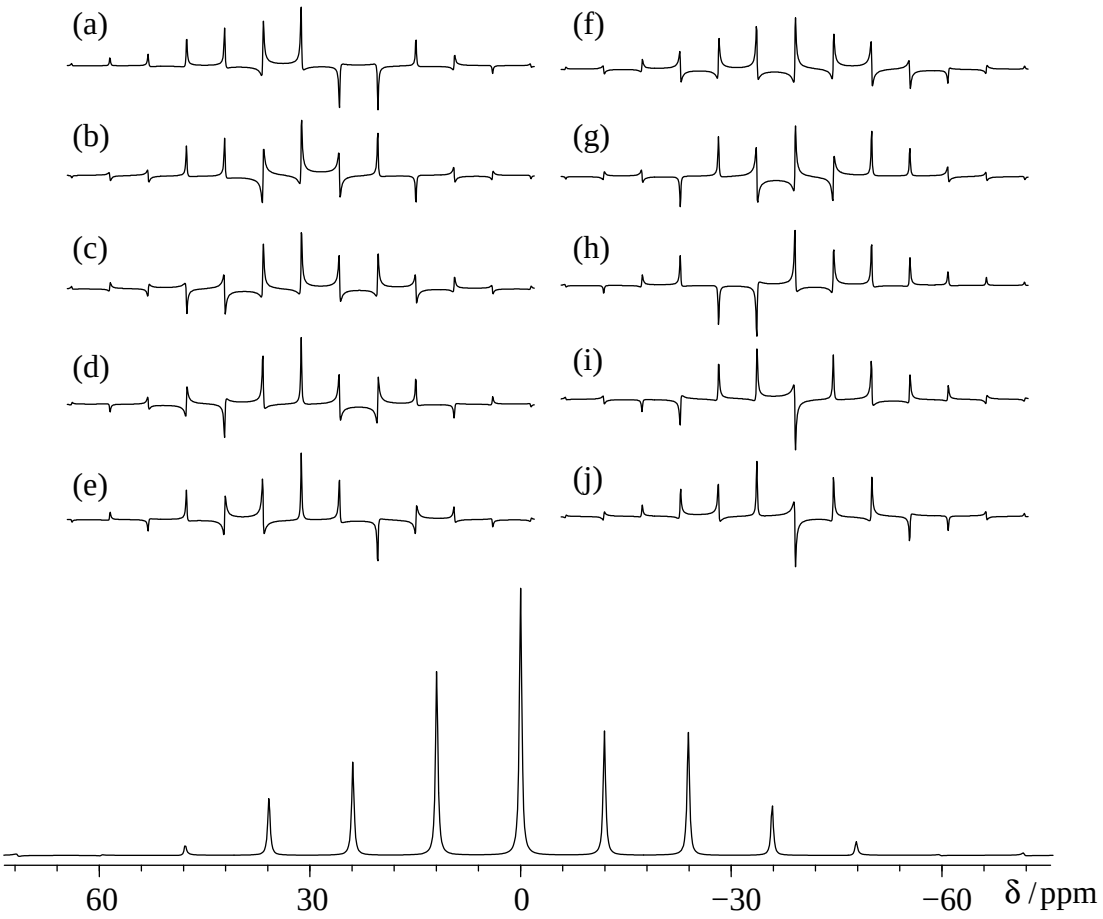

Figure 2.9: (top) Numerical simulations of single-crystal magic angle spinning NMR. Parameters are: $\omega_r/2\pi = 1.5$ kHz, chemical shift anisotropy parameter $\delta_{aniso} = -68.3$ ppm, and asymmetry parameter $\eta = 0.76$. Single-crystal orientation specified by Euler angles $\alpha_{PR} = 350°$, $\beta_{PR} = 95°$, and $\gamma_{PR} = 100°$. (a)-(j) spectra generated by $N = 10$ subsystems with $\alpha_{RL} = 0$, 36°, 72°, 108°, 144°, 180°, 216°, 252°, 288°, 324°, respectively. (bottom) Sum of the spectra (a)-(j).

An interesting question is how many uniform distributions (N) of α_{RL} on the carousal will be sufficient to get an absorptive spectrum of a single-crystal. Fig. 2.10 shows the signal averaging for various N uniform distributions on the carousel. It is observed that better absorptive spectrum could be obtained for larger number of N on the carousel. As an example, the absorptive spectrum for $N = 20$ is compared with the absorptive spectrum for $N = 100$ (spectrum for $N = 100$ is not shown in the Fig 2.10), which shows a signal phase error below 0.05° for the four sidebands of highest intensity. The number of uniform distributions of α_{RL} necessary to achieve an close-to-absorptive spectrum might differ for different samples. This carousal averaging concept of a single-crystal

with an optimum number of α_{RL} distributions is used for my single-crystal MAS NMR work (for detailed see Paper-I).

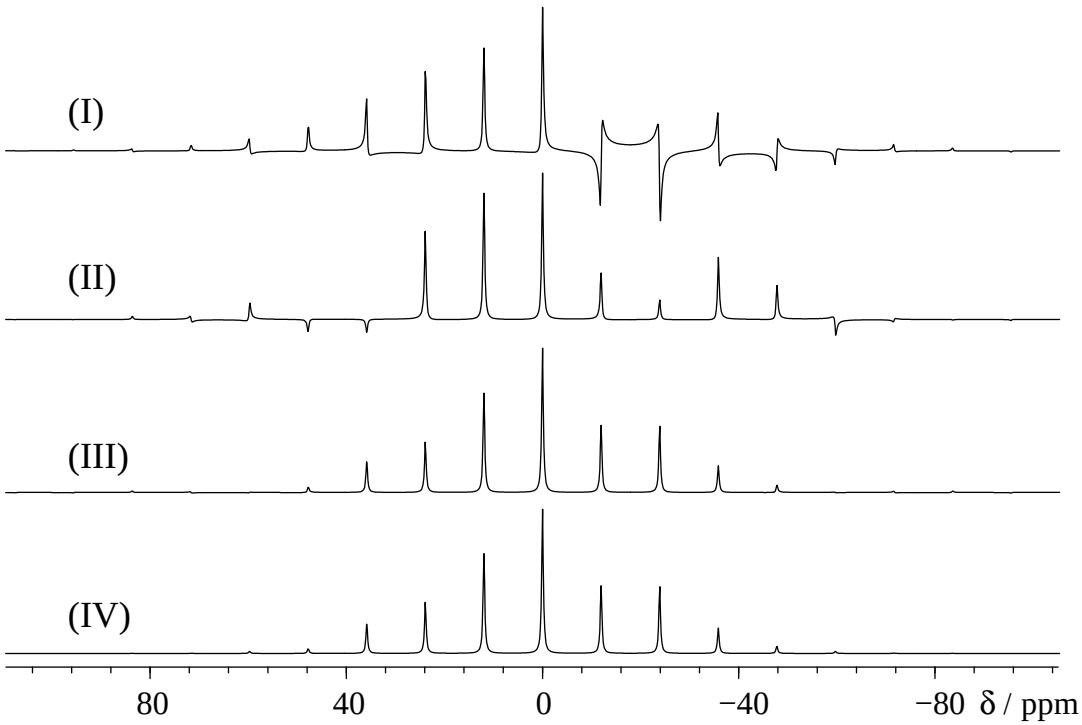

Figure 2.10: Signal averaging of single-crystal magic angle spinning spectra for (I) $N = 2$, (II) $N = 5$, (III) $N = 10$, and (IV) $N = 20$ uniform distributions of α_{RL} on a carousel. Good absorptive spectrum is observed for $N = 20$ (IV). Numerical simulation parameters are same as in Fig. 2.9.

2.12 Bessel Functions

Bessel functions appear in a wide variety of physical problems. Bessel functions contribute to the mathematical analysis with some interesting and useful properties. Some of these properties which are used in this thesis work are described below [198–200].

Bessel function arise from separation of the Helmholtz, or wave, equation in circular cylindrical or spherical coordinates. They are used primarily as solutions of differential equations which is given as [199]:

$$z^2 \frac{d^2w}{dz^2} + z \frac{dw}{dz} + (z^2 - \nu^2)w = 0 \tag{2.94}$$

where the constant ν defines the Bessel functions order which is found in the solution of Bessel's differential equation. The order of the Bessel function is

an integer value for the cylindrical problems i.e. $\nu = n$ while for the spherical problems the order of the Bessel function takes half integer values i.e. $\nu = n + \frac{1}{2}$. There are two linearly independent solutions as the Bessel's differential equation is a second-order equation. The general solution is given by:

$$w = A\boldsymbol{J}_\nu(z) + B\boldsymbol{Y}_\nu(z) \tag{2.95}$$

Here, $\boldsymbol{J}_\nu(z)$ and $\boldsymbol{Y}_\nu(z)$ are the special functions. The special function $\boldsymbol{J}_\nu(z)$ is the Bessel functions of the first kind. It is finite at $z = 0$ for all real values of ν. $\boldsymbol{Y}_\nu(z)$ is the Bessel functions of second kind. It is singular at $z = 0$. This is also known as *Weber* or *Neumann functions*. In this work, the focus is only on the Bessel functions of the first kind.

The useful recurrence formulas for the Bessel functions are given below [198–200]:

$$\boldsymbol{J}_{\nu-1}(z) + \boldsymbol{J}_{\nu+1}(z) = \frac{2\nu}{z}\boldsymbol{J}_\nu(z) \tag{2.96}$$

$$\boldsymbol{J}_{\nu-1}(z) - \boldsymbol{J}_{\nu+1}(z) = 2\,\boldsymbol{J}'_\nu(z) \equiv 2\frac{d\boldsymbol{J}_\nu(z)}{dz} \tag{2.97}$$

$$\boldsymbol{J}_{-\nu}(z) = (-1)^\nu \boldsymbol{J}_\nu(z) \tag{2.98}$$

Following identities are useful for calculating the effects on plane wave as a linear combination of cylinder waves of integral order. These are know as a *fundamental* or *generating function* identity ($\nu = n$) and given by:

$$e^{\pm iz\sin\phi} = \sum_{n=-\infty}^{\infty} \boldsymbol{J}_n(z)\, e^{\pm in\phi} \tag{2.99}$$

Multiplying above equation with its complex conjugate results:

$$1 = \sum_{m,n} \boldsymbol{J}_m(z)\, \boldsymbol{J}_n(z)\, e^{\pm i(m-n)\phi} \tag{2.100}$$

The following summation relation is obtained by integrating above equation over ϕ from 0 to 2π:

$$1 = \sum_{n=-\infty}^{\infty} \boldsymbol{J}_n^2(z) \tag{2.101}$$

Multiplying equation 2.100 by $\cos\phi$ and then integrating over ϕ and using equation 2.96 gives [199, 200]:

$$0 = \sum_{n=-\infty}^{\infty} n\boldsymbol{J}_n^2(z) \tag{2.102}$$

Integral representation of the Bessel function, for integer orders of $\nu = n = 0, 1, 2, 3, ...$, is given as:

$$\boldsymbol{J}_n(z) = \frac{1}{\pi}\int_0^\pi \cos\left(n\phi - z\sin\phi\right) d\phi \tag{2.103}$$

Another integral representation is:

$$\boldsymbol{J}_n(z) = \frac{1}{2\pi} \int_{-\pi}^{\pi} e^{-i\,(n\phi - z\,\sin\phi)}\, d\phi \tag{2.104}$$

The properties of the Bessel functions of the first kind are used to derive an analytical expression to calculate the intensities and the phases of the dispersive lineshape of the spinning sidebands peaks of a single-crystal.

2.13 Solid-State NMR Techniques

In this section, the experimental solid state NMR techniques used in this thesis are described.

2.14 Magic Angle Spinning

In solid state NMR, we generally deal with powdered samples which consist of a vast number of randomly oriented crystallites. The spin interactions in solids are orientation dependent due to restricted molecular motion. The orientation dependence and the superposition of different spin interactions lead to broad spectral lineshapes, where the linewidths are typically tens of kilohertz wide for spin-1/2 [14]. Fig. 2.11 (a) shows a spectrum of $^{13}C_1$-labeled L-alanine under static conditions. The broad features are caused by the ^{13}C CSA's and the homonuclear dipolar couplings.

A static NMR spectrum contains a lot of information which can be related to structural information of the sample, however, retrieval of such information is difficult. The information is dominated by broad lineshapes with low resolution because of anisotropic interactions such as DD-coupling or CSA (Fig 2.11 (a)). *Magic angle spinning* (MAS) technique averages out all anisotropic interactions that can be described by second-rank tensors, to achieve the high resolution spectrum.

The principles of line narrowing by MAS were performed in the late 1950's by Andrew *et al.* [39] and Lowe [40]. As shown in Fig. 2.12, the sample is rotated continuously around an axis which subtends at an angle of $\approx 54.74°$ with respect to the static field, $\mathbf{B}_0$. The spinning frequency of the sample is upto 65 kHz [158].

MAS averages out to zero all the spin interactions (e.g. CSA, DD-coupling), if the spinning frequency is high enough with respect to the interactions size [173]. The spatial rotation of the sample introduces a time-dependence to the anisotropic spin interactions which are averaged out more efficiently as the sample spinning increases (see Fig. 2.11).

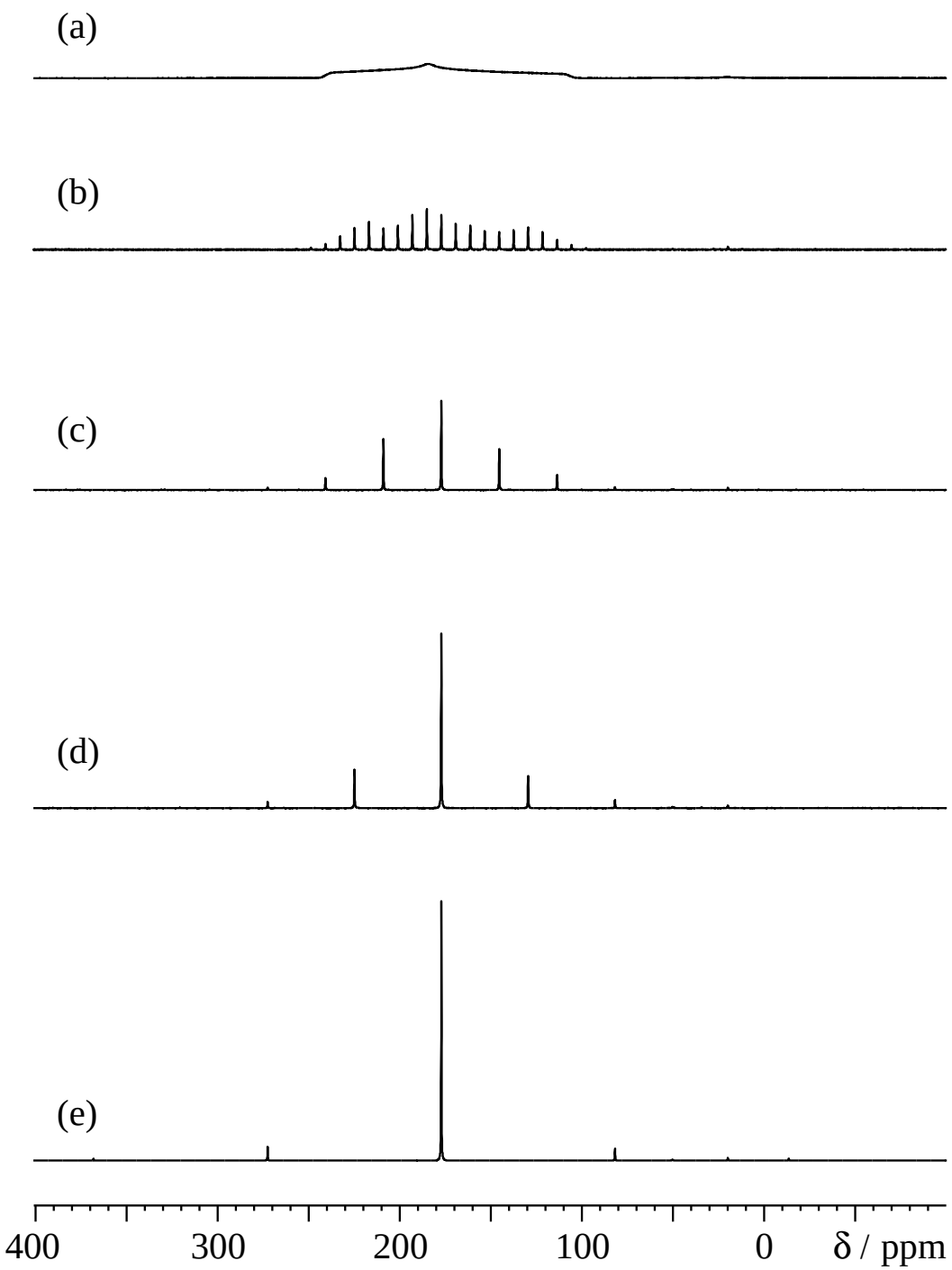

Figure 2.11: ^{13}C CP-MAS spectra of 99%$-^{13}C_1$-labeled L-alanine at a spinning frequency, $\omega_r/2\pi$, of (a) 0.0 kHz, (b) 1.0 kHz, (c) 4.0 kHz, (d) 6.0 kHz, and (e) 12.0 kHz on a 11.74 T spectrometer.

The CSA and DD interactions involve a $(3\cos^2\beta_{PL}-1)$ factor. Rapid isotropic molecular tumbling in solution averages the $(3\cos^2\beta_{PL}-1)$ factor to zero, thus

explaining the narrow NMR lines observed in the solution state. Since there is no rapid isotropic molecular tumbling in solids, it is necessary to find the time average of $(3\cos^2\beta_{PL}-1)$. The time average of the orientation dependence of the nuclear spin interaction, $<\underline{(3\cos^2\beta_{PL}-1)}>$, can be shown as [13, 14, 54]:

$$<\underline{3\cos^2\beta_{PL}-1}>=\tfrac{1}{2}\left(3\cos^2\beta_{RL}-1\right)\left(3\cos^2\beta_{PR}-1\right),\ \text{at}\ \nu_r\to\infty \quad (2.105)$$

where, the angles β_{PL} and β_{PR} are defined in Fig. 2.12.

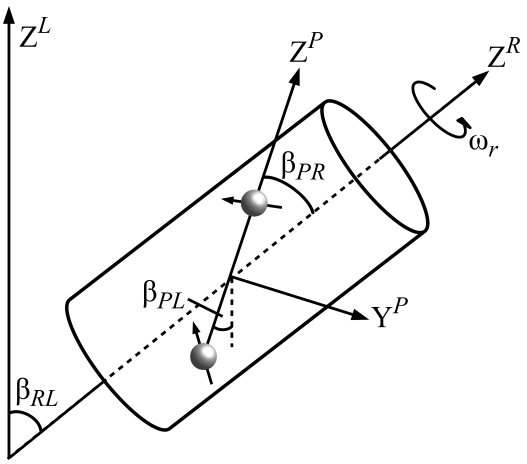

Figure 2.12: Macroscopic sample rotation at an angle to the applied magnetic field $\mathbf{B}_0$. β_{PR} is the angle between the internuclear vector and the rotor axis. β_{RL} is the angle between the rotor axis and the magnetic field. β_{PL} is the angle between the magnetic field and the internuclear vector.

In a powder sample, β_{PR} takes all possible values while the angle β_{RL} is under the control of spectroscopist. When β_{RL} equals the magic angle, $\approx 54.74°$, since $\cos\beta_{RL}=1/\sqrt{3}$ and $\frac{1}{2}\left(3\cos^2\beta_{PL}-1\right)=0$, so that $<\underline{3\cos^2\beta_{PL}-1}>=0$ for all orientations (i.e. all values of β_{PR}). Thus, just as for isotropic tumbling, the CSA and DD interactions are averaged to zero, so effectively the broadening is eliminated, resulting in a higher resolution spectra [14]. This technique applies to both homo- and heteronuclear cases.

Fig. 2.11 shows a series of ^{13}C MAS spectra for $^{13}C_1$-labeled L-alanine at different spinning frequencies. As the spinning frequency increases, numerous peaks begin to appear at frequency distances of integer multiples of the spinning frequency. These additional peaks are known as spinning sidebands. Spinning sidebands can be used to determine details of the anisotropic interactions which are averaged out by MAS.

In case of a single-crystal, spinning sidebands can be used to determine chemical shift tensor orientations as shown in paper-I.

2.15 Spin Echoes

A solid state NMR spectrum often consists of broad lines arising from a rapidly decaying FID. The NMR signal cannot be measured immediately after a pulse, because some time, the *dead time*, is needed during which the electric transients induced by the powerful pulse are allowed to decay. Some portion of the FID cannot be acquired due to this dead time, for example in case of amorphous samples. However, the transverse magnetization is not stationary but evolves under various spin interactions during the dead time. As a consequence, a loss of intensity and severe baseline distortion are observed in NMR spectra.

A spin-echo pulse-sequence introduced by Hahn in 1950 [201], is used to regain the FID signal loss due to the dead time shown in Fig. 2.13.

$$90^\circ_x - \tau/2 - 180^\circ_y - \tau/2 - acquire \tag{2.106}$$

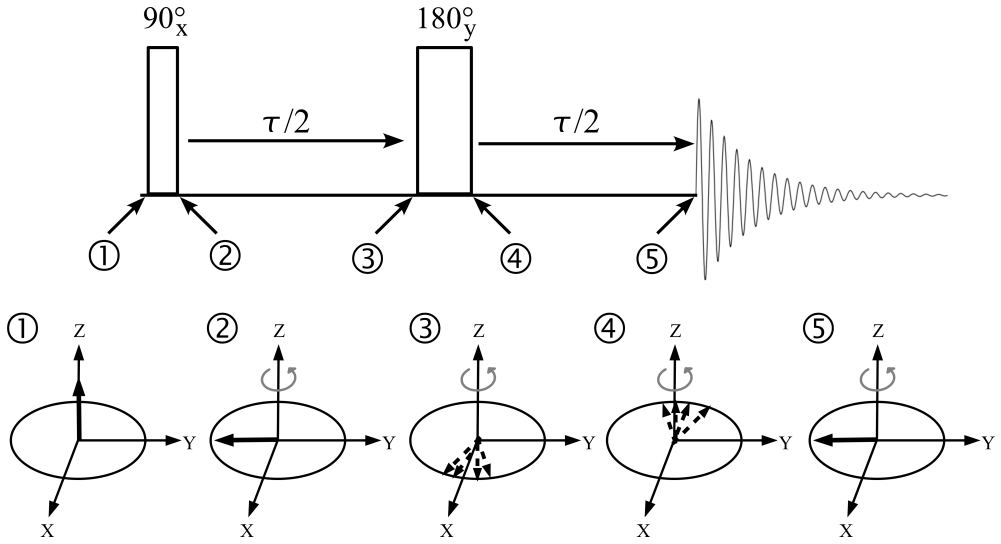

Figure 2.13: A spin-echo pulse-sequence shows ① preparation of transverse magnetization, ② the transverse magnetization evolves for the first time interval, $\tau/2$, ③ the magnetization is then flipped by a π pulse, ④ the magnetization is allowed to evolve for another time period, $\tau/2$, and ⑤ the spin-echo forms.

In the spin-echo sequence, the initial 90°_x pulse aligns the magnetization along the y-axis (Fig. 2.13 ①-②). The magnetization is then allowed to precess freely for a period of $\tau/2$ until the 180°_y pulse is applied (Fig. 2.13 ③). It flips the magnetization to its mirror image position (Fig. 2.13 ④). The magnetization is refocused along the y-axis after precessing freely for an identical period of time $\tau/2$ (Fig. 2.13 ⑤).

It should be noted that, for echo formation in rotating solids, the intervals $\tau/2$ must be an integer number of the rotor period [202]. A use of the spin-echo sequence eliminates the signal loss due to the dead time. The relaxation of the transverse magnetization during the τ period contributes in remaining signal loss [13].

The application of the spin-echo technique for the quantification of ^{1}H NMR signals under low resolution conditions for solids is described in paper-II.

2.16 Cross Polarization

Solid-state NMR of nuclei with low abundance often referred as *rare* nuclei (e.g. ^{13}C, ^{15}N), and has low sensitivity. The equation 2.35 shows that, for a given temperature and field, the observable magnetization is proportional to the gyromagnetic ratio of each nucleus. The sensitivity of rare spins, S-spins, with low gyromagnetic ratios can be enhanced by transferring magnetization from abundant spin species, I-spins, with high gyromagnetic ratios (e.g. ^{1}H). Cross-polarization (CP) [46] is a method used to transfer polarization between unlike species through the dipolar interaction between I and S spins.

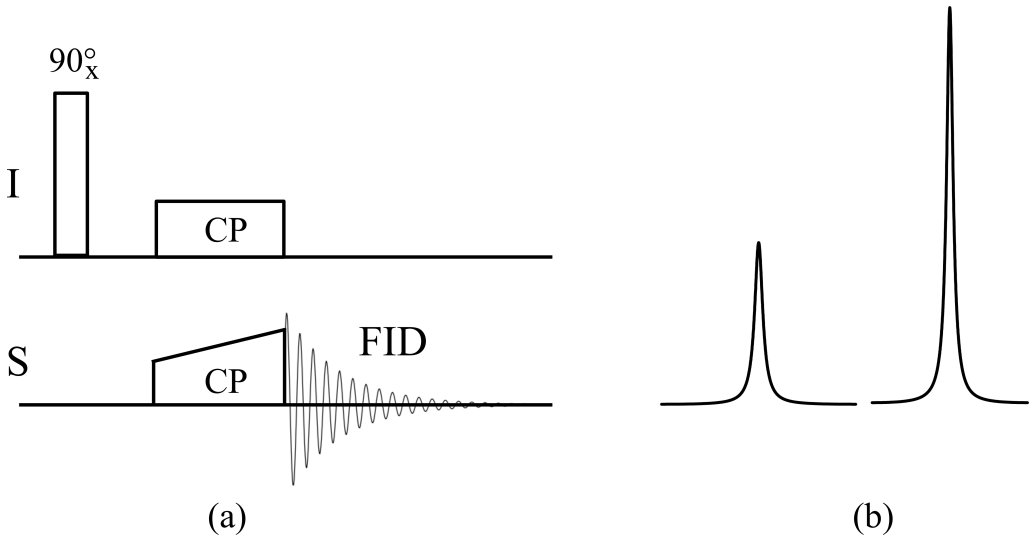

Figure 2.14: (a) The ramped cross-polarization [133] sequence, starting with a $\pi/2$ pulse being applied to the I channel. In effect, the transfer of the magnetization from the abundant spin I to the rare spin S occurs via the dipolar coupling between the spins. Finally, acquisition of the S signal is acquired. (b) The result of applying ramped-CP: the signal gets stronger.

In cross polarization, a $\pi/2$ pulse is applied to flip the I magnetization into the xy-plane and then *spin-locked* for a certain interval of time, called as the

contact time, and simultaneously an rf field is applied on the S channel as well. The enhancement of transverse S magnetization can be achieved using a proper choice of the nutation frequencies of the two fields. Under static conditions, the nutation frequencies are tuned to fulfil the Hartmann-Hahn condition [203], $\omega^I_{nut} = \omega^S_{nut}$. The cross polarization condition under magic angle spinning (MAS) becomes, $\omega^I_{nut} = \omega^S_{nut} + n\omega_r$, where n is an integer number. The Hartmann-Hahn matching condition is difficult to achieve for high spinning frequencies and as a consequence, the CP sequence performance decreases. The increase in the signal is ideally enhanced by a factor of around γ_I/γ_S.

An improvement in the reliability and reproducibility of the CP experiment is the *ramped*-CP [133] experiment, which is presented graphically in Fig. 2.14. In the ramped CP experiment, the contact pulse on one of the spins (it can be either) is steadily increased in amplitude over the contact period.

2.17 Heteronuclear Spin Decoupling

The application of rf fields in order to remove the effects of dipolar couplings in solid state NMR is known as decoupling. In solid samples, it is necessary to use decoupling in order to obtain high spectral resolution.

Much of the chemical shift anisotropies and through-space dipolar couplings (a few Hz to tens of kHz) are averaged out when magic angle spinning is performed with spinning frequencies greater than 30 kHz [204]. However, for the moderate spinning frequencies employed in Fig. 2.11, the effect of ^{13}C-^{1}H (S-I) dipolar couplings is not fully suppressed and the residual dipolar couplings make spectral lines broad. Therefore, rf irradiation techniques (heteronuclear decoupling methods) are needed to decouple these strong heteronuclear interactions. There are many heteronuclear decoupling methods available; however, only the methods used for the work in this thesis will be discussed below.

2.17.1 Continuous Wave Decoupling

A technique called *continuous wave* (CW) decoupling is used to eliminate heteronuclear couplings in solid state NMR spectroscopy (Fig. 2.15). CW decoupling works by rotating the spin state of ^{1}H (I) spins, and the dipolar interaction is averaged out every π rotation while the spin state of the ^{13}C (S) spins is not modified.

Sample rotation and CW rf irradiation can interfere with each other under magic angle spinning NMR, if their timescales are comparable. This interference leads to inefficient heteronuclear decoupling. Under MAS, CW decoupling has the following regimes namely *high power CW decoupling* and *low power CW decoupling* [205]. In high power CW decoupling, high CW irradiation (50-250 kHz) is applied while the spinning frequency is maintained in a low-moderate regime

(upto 25 kHz). In this regime the linewidth decreases when the rf irradiation is increased. However, low power CW decoupling is applied under high spinning frequency (> 40 kHz) and the continuous wave rf field is maintained above 50 kHz [205].

As stated by Ernst *et al.*, low power CW decoupling can be used instead of high power CW decoupling for spinning frequencies above 40 kHz [206]. In this case, the rf field strength should be about 1/4 of the spinning frequency. Additionally, for spinning frequencies above 50 kHz, the rf field strength can also be about 2/5 of the spinning frequency [206].

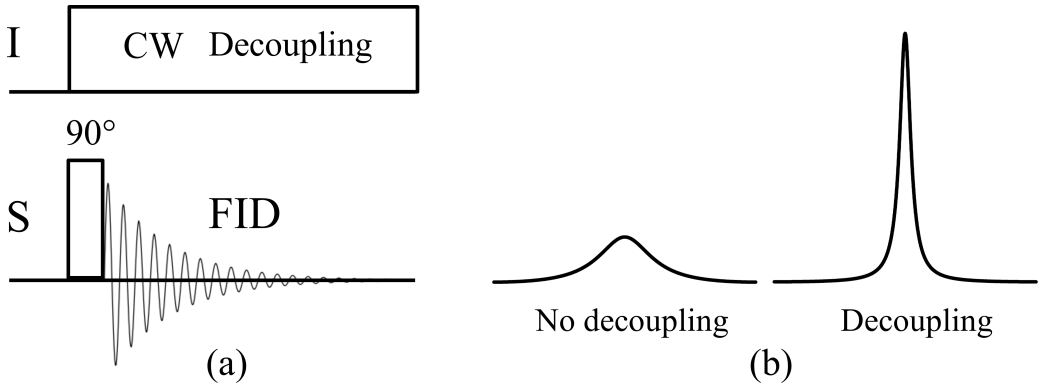

Figure 2.15: (a) Direct excitation with heteronuclear continuous-wave decoupling. (b) The result of the decoupling: spectral lines become narrower, while their peak areas remain conserved.

One of the limitations of CW decoupling is that *off-resonance effects* produce incomplete heteronuclear decoupling. Residual line splittings increase with increasing MAS frequency and decoupling sidebands can be observed at the rf irradiation frequency. However, the introduction of *phase modulated decoupling sequences* [207, 208] has given a significant improvement in both linewidth and line intensity.

2.17.2 Two Pulse Phase Modulation

A *two pulse phase modulation* (TPPM) decoupling technique introduced by Bennett *et al.* [207], is a multiple-pulse technique which is relevant for decoupling under MAS condition.

In the presence of a strong proton (I) decoupling field, the resonance offset effect causes ^{1}H line broadening in solid-state MAS NMR spectra of S spins (e.g. ^{13}C, ^{15}N, ^{31}P, etc.) [209]. The offset originates from following two sources. First is a broadening of the isotropic chemical shifts in a ^{1}H spectrum (≈ 10 ppm). Second, a crystallite in a powder under MAS experiences a range of proton frequencies, due to proton CSA, which are sampled over the rotor period. As a

result, it is impossible to set the transmitter frequency precisely *on-resonance* even for a single ^{1}H [210].

The residual linewidths arising from insufficient ^{1}H decoupling are reduced with the help of TPPM decoupling [207]. TPPM decoupling gives significant improvements in both the linewidth and line intensity [207] at moderate spinning frequencies (10-40 kHz).

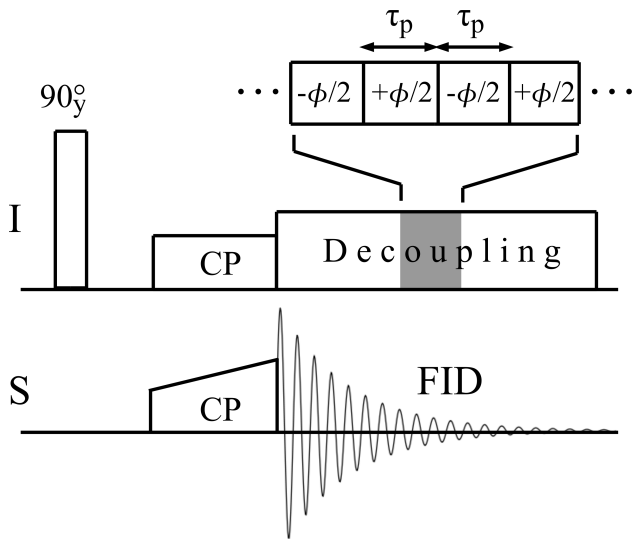

Figure 2.16: Pulse-sequence for a CP-MAS experiment with TPPM decoupling applied to the I channel throughout the acquisition of the FID on S. The grey section in the decoupling period illustrates the rapid alternation of the phase of rf excitation between $+\phi/2$ and $-\phi/2$ with the overall period τ_p.

The TPPM pulse-sequence consists of application of rf pulses of length τ_p with an alternating phase $\pm\phi/2$ (Fig. 2.16) [205,207]. Often, the optimum values of the flip angle are near 180° and the optimum values of the phase ϕ are between 10°-70° [13]. Experimental linewidth in the TPPM decoupling sequence is sensitive to the precise setting of the pulse length and the phase angle [211]. Changes in the experimental parameters (e.g. rf field strength, MAS frequency, spectrometer, or probe) may require reoptimization of both the pulse length and the phase angle of the sequence.

The decoupling efficiency of the TPPM is often better that CW, especially at higher spinning frequency, which is apparent from the achievable linewidth.

2.18 Recoupling

The dipolar coupling and chemical shift anisotropy interactions lead to the significant loss in the resolution of the NMR spectrum in static solids. Magic angle

spinning (MAS) can be used to obtain highly resolved spectra. Unfortunately, MAS also suppresses the direct dipole-dipole couplings, which are essential to determine distance constraints by NMR. The dipolar coupling interaction can be reintroduced for selected periods of an experiment by carefully designed pulse-sequences, known as recoupling sequences [212]. The basic principle of recoupling sequences is to reintroduce all the dipolar couplings associated with the irradiated spin types.

There is a wide range of recoupling methods for homo- and heteronuclear spin systems [7, 212, 213]. Some of the recoupling methods are Dipolar Recoupling at the Magic Angle (DRAMA) [214], Homonuclear Rotary Resonance (HORROR) [215], Rotational Echo Double Resonance (REDOR) [128], Radio Frequency Driven Dipolar Recoupling (RFDR) [216], and symmetry-based C-type and R-type sequences [175, 217–219].

2.18.1 Rotational Echo Double Resonance

The *rotational echo double resonance* (REDOR) method introduced by Gullion and Schaefer [128] has proven to be useful for the measurement of internuclear distances between unlike nuclei. REDOR provides site selective dipolar coupling information under magic angle spinning [220–223]. As described earlier in equation 2.60, the dipolar Hamiltonian for a heteronuclear interaction can be split into the space, I spin ("abundant" spins) and S spin ("rare" spins) parts. Under the MAS, the dipolar interaction is averaged out over the rotor cycle. However by applying a train of π-pulses to the non-observed S-spins, the dipolar interaction in average is non zero and hence the interaction is recoupled.

The REDOR sequence is shown in Fig. 2.17. It consists of two separate experiments. The first is a spin-echo experiment in which the dipolar coupling between the IS-spin pair is averaged out at the end of every rotor period (Fig. 2.17, a) which yields the "full echo" intensity. In the second experiment, Fig. 2.17 (b), this averaging of the dipolar coupling is prevented by a series of rotor synchronized π-pulses applied to the S-spins. Hence a decrease in signal intensity of the dephased-echo intensity shows the through space proximity between I and S spins i.e. the heteronuclear dipole-dipole coupling. The intensities of the full-echo (absence of recoupling pulses) and the dephased-echo (presence of recoupling pulses) are S_0 and S, respectively. Experiments are performed as a function of a rotor period and one measures the normalized difference signal as:

$$\frac{\Delta S}{S_0} = \frac{(S_0 - S)}{S_0}, \tag{2.107}$$

A REDOR curve is then generated by plotting $\Delta S/S_0$ as a function of dephasing time, $N\tau_r$, as shown in Fig. 2.18. The $N\tau_r$ is the duration of one rotor period, τ_r, multiplied by the number of rotor cycles, N. Fig. 2.18 shows simulated REDOR curves for two-spin systems, for example ^{119}Sn-^{19}F.

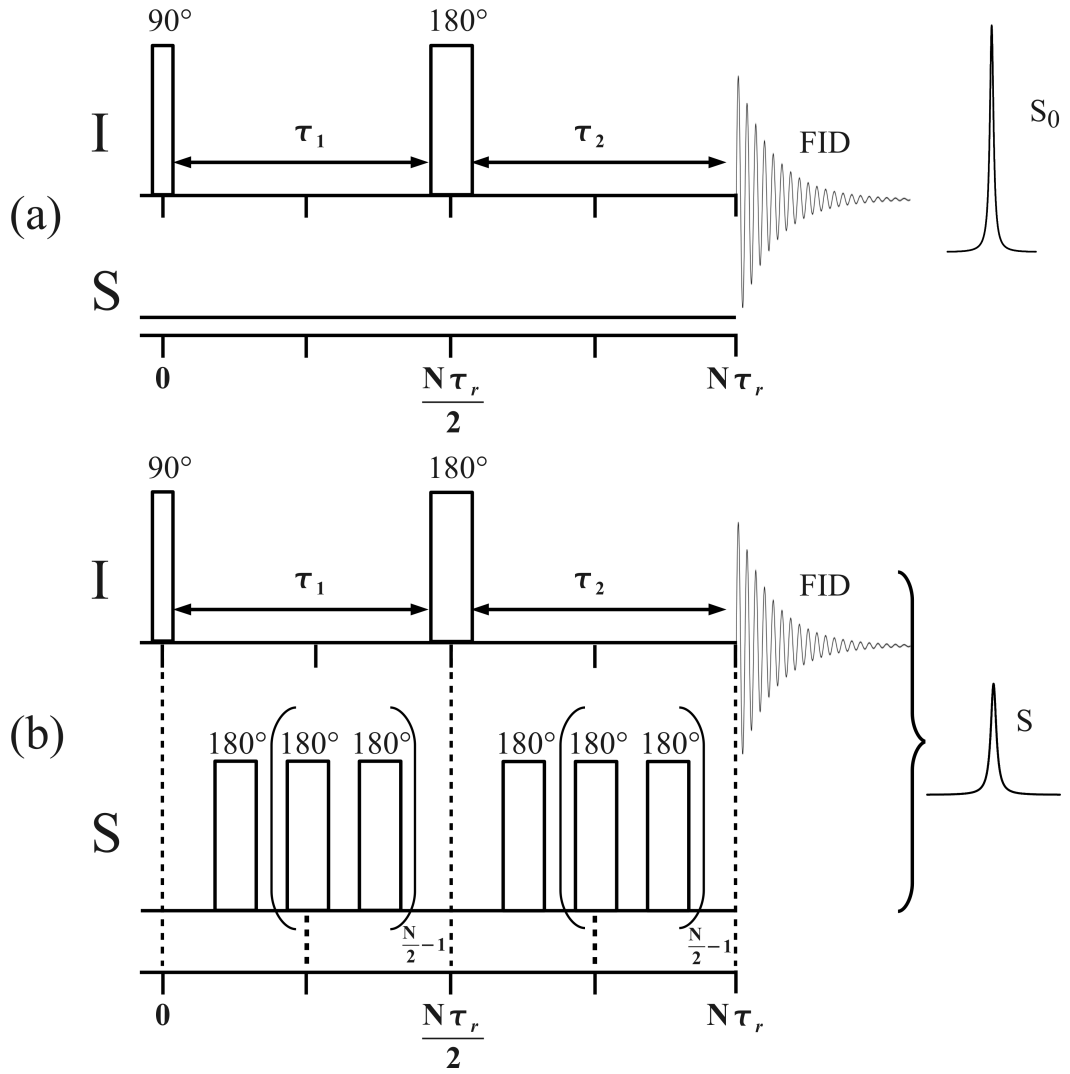

Figure 2.17: Schematic diagram of the pulse-sequence for a REDOR experiment: (a) The spin-echo pulse-sequence results in the full-echo intensity S_0. (b) The REDOR experiment, in order to measure the dipolar coupling between the I and S spin. $N\tau_r$ gives the number of full rotor-periods (τ_r). S is the intensity of the dephased-echo.

A REDOR curve has a universal character for two-spin (spin-1/2) systems, and can be directly used to obtain the inter-nuclear distance [128, 220, 224, 225]. However, for large number of coupling nuclei in a spin-system the REDOR curve is dependent on the orientation [223, 226]. The REDOR curve is found to be geometry-independent by limiting the REDOR data analysis to the initial curvature, where $\Delta S/S_0 < 0.2$ [223, 227–229]. The analysis of the initial curvature in a two-spin approximation leads to a dipole-dipole coupling constant (b_{IS}) as described in equation 2.58. The dipole-dipole coupling constant can be com-

pared with the *effective dipole-dipole coupling constant*, ν_{eff}. The ν_{eff} can be calculated from the sum of all squared dipole-dipole coupling constants from the observed spin I to all surrounding spins S. The sign of the ν_{eff} can be chosen according to the sign of the individual dipole-dipole coupling constants. The effective dipole-dipole coupling constant behaves as a heteronuclear second moment (M_2) [159, 223] apart from a constant pulse-sequence dependent factor and is given by:

$$|\nu_{eff}| = \sqrt{\sum_S b_{IS}^2} \tag{2.108}$$

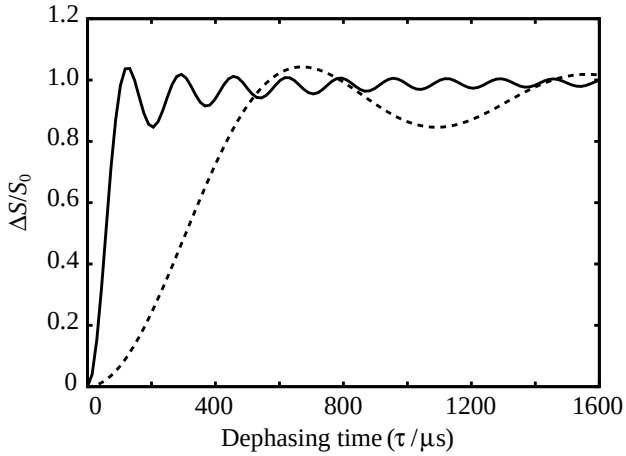

Figure 2.18: ^{119}Sn{^{19}F} REDOR simulated curve for SnF spin system. ^{119}Sn-^{19}F distances are 2.052 Å (solid line) and 3.593 Å (dashed line).

2.18.2 Symmetry-Based Recoupling Sequences

Using symmetry-based recoupling sequences, it is possible to select certain spin interactions while suppressing others [175]. In general, each spin interaction can be expressed as a product of three terms, namely *space* which expresses the transformation properties of the interactions with respect to rotations of the molecular framework, *spin* which expresses the rotations of the nuclear spin polarizations, and rotations of the external magnetic field [175]. Each nuclear spin interaction is defined by the rotational properties which can be summarized in terms of three *rotational ranks* and is known as *rotational signature* of a spin interaction as shown in Table. 2.5.

The nuclear spin interactions have ranks 0, 1, or 2. Using the analogy of atomic orbital symmetry, the rank 0, 1, and 2 are related with atomic orbital symmetry of s, p, and d orbital, respectively. As an example, consider the homonuclear dipolar interaction, which has rank 2 for both spatial and spin rotations. This indicates that a rotation of the molecular framework by 180° does

not change the interaction strength, but a rotation through 90° changes the sign of the interaction.

Table 2.5: "Rotational signatures of homonuclear spin interactions in diamagnetic systems of spin-1/2" [175].

Interaction	Space rank, l	Spin rank, λ	Field rank
Isotropic chemical shift	0	1	1
Chemical shift anisotropy	2	1	1
Isotropic J-coupling	0	0	0
DD-coupling	2	2	0

The space and spin elements can be broken down into components denoted by m for space components and μ for spin components (Table 2.6). The space components, m take the values of $m = -l, -l+1, ..., +l$; and the spin components, μ take the values of $\mu = -\lambda, -\lambda+1, ..., +\lambda$. Components with $l = 2$ and $m = 0$ vanish under MAS [175]. Both the space and spin components can be manipulated to generate an average Hamiltonian containing specific spin interaction terms $\{l, m, \lambda, \mu\}$ while others are suppressed. These pulse-sequences are categorized

Table 2.6: "Components of homonuclear spin interactions in the interaction frame of an applied radiofrequency field, in the case of MAS" [175].

Spin Interaction	Space Rank, l	Space Components, m	Spin Rank, λ	Spin Components, μ
Isotropic chemical shift	0	0	1	{-1,0,1}
CSA	2	{-2,-1,1,2}	1	{-1,0,1}
Isotropic J-coupling	0	0	0	0
DD-coupling	2	{-2,-1,1,2}	2	{-2,-1,0,1,2}

in families of general nature CN_n^ν or RN_n^ν. The C-type sequence consists of the pulse-sequence being built by repeating radiofrequency cycles, with incrementing phases [218, 219, 230, 231]. The R-type sequence, consists of a basic construction block for the pulse-sequence which is a 180°rotating element, denoted by $\mathcal{R}$ [175, 217, 232]. Both the C- and R-type sequences are based on rf irradiations with phase shifted pulses, with an integer number N of pulse elements fitted into an integer number n of rotor revolutions.

2.18.2.1 CN_n^ν-sequence

A CN_n^ν sequence can be constructed by dividing n rotational periods into N equal intervals during which a cyclic rf sequence is applied, which implies that

the rf sequence induces a rotation of nuclear spin polarization through an integer multiple of 360°. The phase difference between the successive cyclic rf elements is given by $2\pi\nu/N$, where ν is the winding number. At the same time, the sample experiences a set of cyclic rf elements and its phases advances through ν full rotations. Fig. 2.19 (a) shows a schematic diagram of the CN_n^ν-sequence with timing.

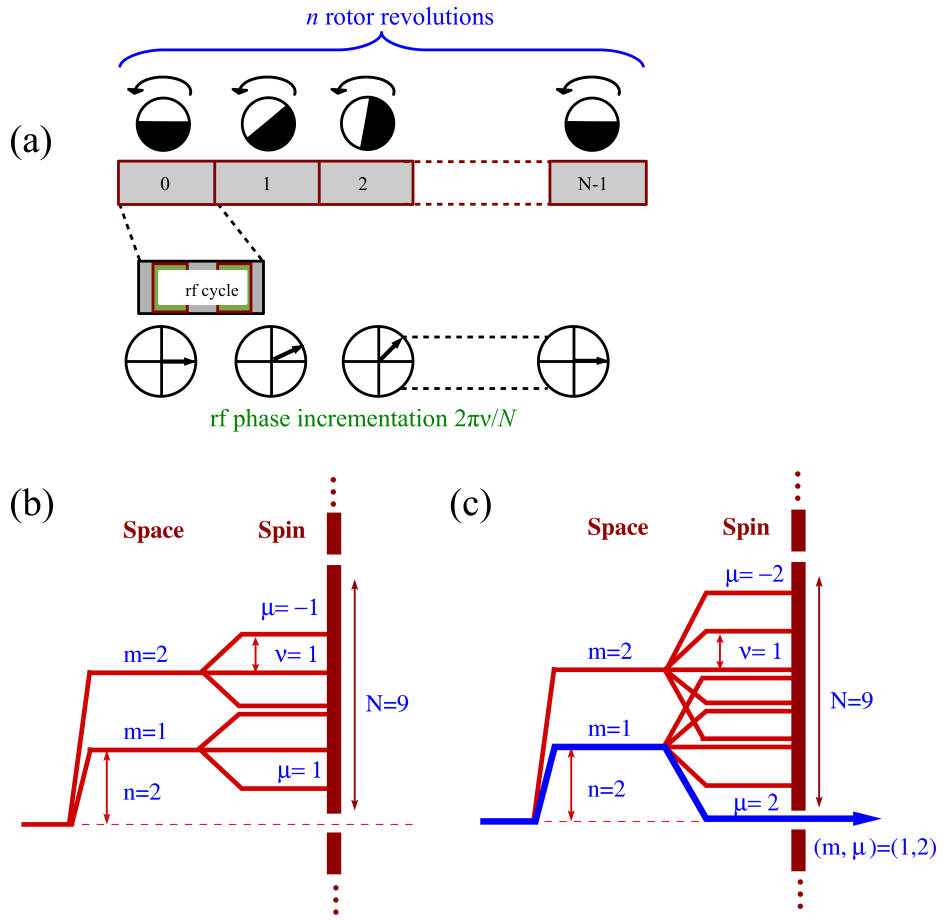

Figure 2.19: (a) Construction of a CN_n^v sequence. The pulse-sequence is set up in such a way that n rotor revolutions are synchronized with N rf elements. The phase of consecutive elements increments in steps of $2\pi\nu/N$. (b-c) Space-spin selection diagram for $C9_2^1$ symmetry, where the components with $m < 0$ have been omitted. Suppression of all CSA modulation components (b). Behavior of homonuclear dipole-dipole coupling terms (c). The component $(l, m, \lambda, \mu) = (2, 1, 2, 2)$ is symmetry-allowed. This diagram (a-c) is adapted from [175].

Following selection rule is applied to determine whether a spin interaction term is symmetry-allowed or symmetry-forbidden on the average Hamiltonian

terms [217–219]:

$$\hat{\mathcal{H}}_{lm\lambda\mu} = 0, \quad \text{if} \quad mn - \mu\nu \neq NZ \tag{2.109}$$

where Z is any integer [231].

The symmetry sequence $C9^1_2$ is taken as an illustrative example where $N = 9$, $n = 2$, and $\nu = 1$ [174]. Consider the double quantum dipole-dipole term with $\{l, m, \lambda, \mu\} = \{2, 1, 2, 2\}$. The term $mn - \mu\nu$ gives a value 0, which is an integer multiple of $N = 9$. Hence, we can say the DD coupling term is symmetry-allowed in the $C9^1_2$ sequence. Further, the CSA term is assumed as $\{l, m, \lambda, \mu\} = \{2, 2, 1, 1\}$, the result of $mn - \mu\nu$ gives a value 2, which is not an integer multiple of $N = 9$. Hence the CSA interaction is said to be symmetry-forbidden under $C9^1_2$.

Fig. 2.19 (b) and (c) shows a space spin selection diagram to depict the selection rules. The diagram clearly shows that in case of $C9^1_2$ sequence, the two homonuclear dipolar terms are symmetry-allowed, whereas all the CSA terms are suppressed. This sequence therefore recouples the DD coupling terms while it suppresses the CSA terms. Since only dipole-dipole terms with spin quantum number $\mu = \pm 2$ are allowed this sequence, results in the generation of CSA compensated double quantum recoupling sequence [175].

We have characterized the noncrystalline zinc phosphate (paper-IV) as well as fluorine doped tin oxide nanomaterials (FTO, SnO_2:F) (paper-V) by using Permutationally Offset Stabilized C (POST-C) variant of $C3^1_3$ sequence together with REDOR [128–130].

2.18.2.2 RN^ν_n-sequence

The basic rf element of RN^ν_n sequence denoted as $\mathcal{R}$ consists of a pulse or pulses (composite pulses) that rotates the nuclear spin polarization through an angle of 180°around the x-axis [175]. The $\mathcal{R}$ element is repeated again with changing the signs of the rf phases within the element $\mathcal{R}$. This phase-inverted element is called $\mathcal{R}'$. The rf amplitude is selected so that the N elements occupy exactly the same time interval as n rotational periods of the sample and denoted by $\tau_R = n\tau_r/N$ where $\tau_r = 2\pi/\omega_r$ is the rotor period and ω_r is the angular spinning frequency. Here N is an even integer and n is any integer. The RN^ν_n sequence can now be developed using $N/2$ concatenating phase shifted $\{\mathcal{R}\mathcal{R}'\}$ pairs as follows:

$$RN^\nu_n = (\mathcal{R})_\phi(\mathcal{R}')_{-\phi}(\mathcal{R})_\phi(\mathcal{R}')_{-\phi}...(\mathcal{R}')_{-\phi} \equiv \{\mathcal{R}_\phi\mathcal{R}'_{-\phi}\}^{N/2} \tag{2.110}$$

where the phase shifts are specified by, $\phi = \pi\nu/N$, and ν is an integer. Fig. 2.20 (a) shows a schematic construction of the RN^ν_n sequence.

The selection rule for the RN^ν_n sequence can be described as [217]:

$$\hat{\mathcal{H}}_{lm\lambda\mu} = 0, \quad \text{if} \quad mn - \mu\nu \neq \tfrac{N}{2}Z_\lambda \tag{2.111}$$

where Z_λ is any integer with the same parity as that of λ. This implies that if λ is odd then Z_λ is any odd integer and if λ is even then Z_λ is any even integer [232].

From this it is quite evident that RN_n^ν sequences are more restrictive than CN_n^ν sequences [175].

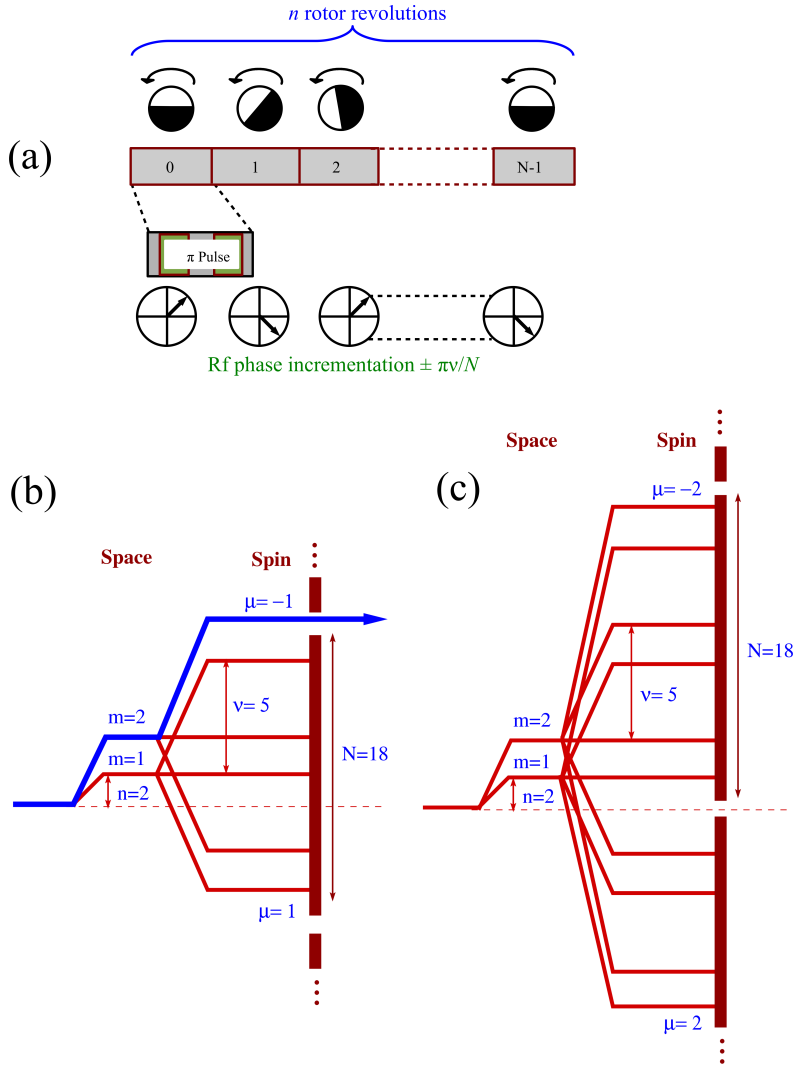

Figure 2.20: (a) Construction of a RN_n^ν sequence. The pulse-sequence is set up in such a way that n rotor revolutions are synchronized with N rf elements. The phase of consecutive elements increments in steps of $\pm\pi\nu/N$. (b-c) Space-spin selection diagram for $\mathrm{R18}_2^5$ symmetry, where the components with $m < 0$ have been omitted. Behavior of the heteronuclear dipole-dipole terms (b). The component $(l, m, \lambda, \mu) = (2, 2, 1, -1)$ is symmetry-allowed. Suppression of all homonuclear dipole-dipole components (c). This diagram (a-c) is adapted from [175].

Here, $\mathrm{R18}_2^5$ sequence is considered as an example [233]. The heteronuclear dipolar coupling interaction is assumed with $\{l, \lambda\} = \{2, 1\}$. For this interaction

$l = 2$, there are four m components with $m = \{-2, -1, 1, 2\}$ and since $\lambda = 1$ there are three components of $\mu = \{-1, 0, 1\}$. For the combinations of $\{l, m, \lambda, \mu\} = \{2, 2, 1, -1\}$ and $\{2, -2, 1, 1\}$, the selection rule $mn - \mu\nu$ results values of 9 and -9, both of which are odd integers of $\frac{N}{2} = 9$ and spin rank λ is also odd. Hence these terms are symmetry-allowed.

Now consider, homonuclear dipolar coupling interaction with $\{l, \lambda\} = \{2, 2\}$. It can be easily found out that combinations of $\{l, m, \lambda, \mu\}$ yields an even integer multiple of $\frac{N}{2} = 9$. This means that homonuclear dipolar coupling interaction is symmetry-forbidden under the application of $R18_2^5$ sequence. Fig. 2.20 (b) and (c) summarizes the results.

We have made use of symmetry-based pulse-sequence $SR6_6^2$ with the R-element $270_0\text{-}90_{180}$ [232] for the background compensated 2D-DEPTH-$SR6_6^2$ homonuclear zero-quantum recoupling experiments to probe homogeneity of point defects as in the case of fluorine doped tin oxide nanoparticles (paper-V). Similarly, a modified two-dimensional version of PRESTO-III based on $R18_1^7$ recoupling sequence [135] is used to investigate heteronuclear patterns between ^{27}Al and ^{1}H in the case of aluminum doped zinc oxide nanoparticles (AZO, ZnO:Al) (paper-VI).

2.19 Multiple Quantum Magic Angle Spinning

The second order quadrupolar line broadening of quadrupolar nuclei ($I > 1/2$) can be eliminated by combining MAS NMR with multiple quantum excitation known as *multiple quantum magic angle spinning* (MQMAS), introduced by Frydman *et al.* [234] and Amoureux *et al.* [235]. In MQMAS, the second-order quadrupolar broadening can be eliminated by refocusing the fourth-rank elements of the second-order quadrupole interaction in spin space, which provides 2D high-resolution NMR spectra of quadrupole nuclei.

The main drawback of the MQMAS experiment is the rather inefficient conversion between the zero and multiple quantum (MQ) coherence. In order to enhance the resolution and a high efficiency of MQMAS, the dispersion signal is decreased by using z-filter principles to MQMAS [236]. A standard z-filtered triple-quantum magic angle spinning pulse-sequence, along with the respective coherence level diagram is shown in Fig. 2.21(a-b) [236]. Multiple quantum (MQ) coherence is excited by the initial pulse. During time period t_1, multiple quantum coherence evolves which is followed by the second intense pulse converting it to zero-quantum coherence. A soft selective pulse follows the z-filter and produces single quantum coherence which is related to the central transition. The single quantum coherence is acquired during the detection period t_2. Double Fourier transformation with respect to both time domains t_1 and t_2 is performed providing a 2-D spectrum (Fig. 2.21, c). The 2D NMR spectrum after shearing has an isotropic dimension which is free of second order quadrupolar line broadening and the normal anisotropic dimension.

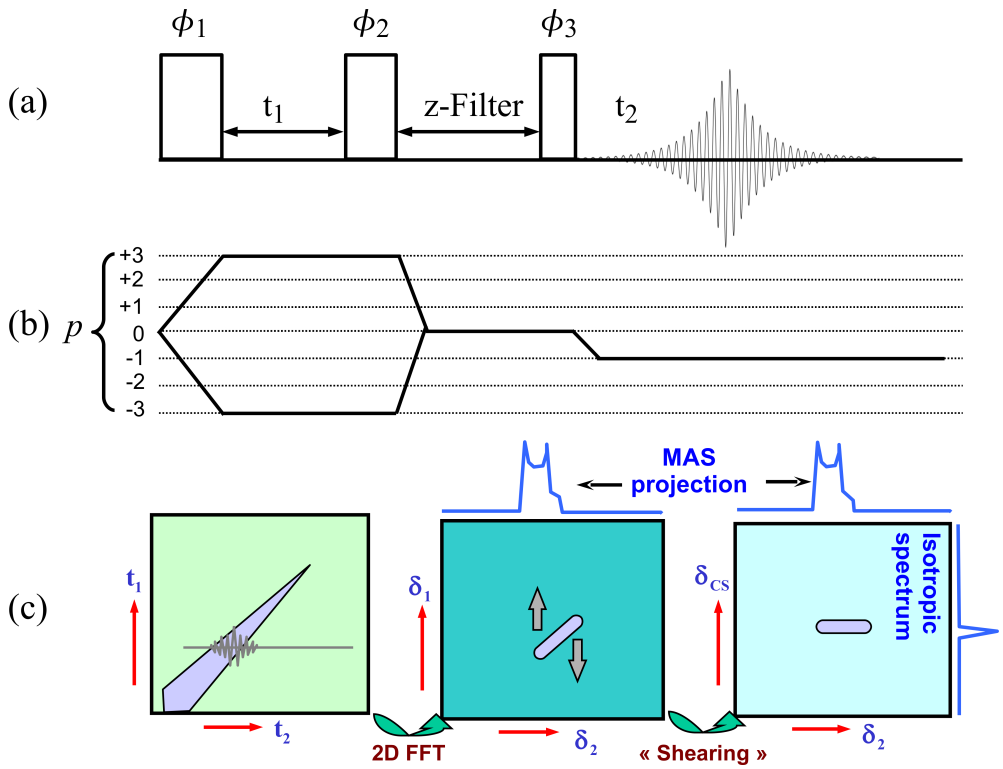

Figure 2.21: (a) A pulse-sequence of a 2D triple quantum z-filtering magic angle spinning (TQMAS) experiment. ϕ_1, ϕ_2, and ϕ_3 represent the phases of the excitation, reconversion, and selective $\pi/2$ pulses, respectively. (b) A coherence transfer pathways (p): $0 \rightarrow \pm 3 \rightarrow 0 \rightarrow -1$. (c) The 2D TQMAS shows systematic increment in t_1, acquisition in t_2, double FFT in t_1 and t_2 and the result of shearing transformation along δ_1: results in high resolved projection.

Fig. 2.21 (c) shows a schematic- triple quantum magic angle spinning NMR spectrum, followed by a double Fourier transformation with respect to time domains t_1 and t_2 and the result of a shearing transformation. δ_2 is the normal anisotropic dimension while δ_{CS} is the high resolution isotropic dimension obtained after the shearing transformation. From resultant data, the isotropic chemical shift δ_{iso}^{CS} and isotropic quadrupolar shift δ_Q can be obtained as defined below. For spin $I = 3/2$, the centers of gravity of the observed signals in the isotropic (F_1) and the anisotropic (F_2) dimensions are δ_{F_1} and δ_{F_2}, respectively and given by [3, 223]:

$$\delta_{F_1} = \frac{34\delta_{iso}^{CS} - 60\delta_Q}{9} \tag{2.112}$$

$$\delta_{F_2} = \delta_{iso}^{CS} + 3\delta_Q, \tag{2.113}$$

where

$$\delta_Q = \frac{-(\mathrm{SOQE})^2}{30\nu_0^2[2I(2I-1)]^2}. \tag{2.114}$$

Here, ν_0 is the nuclear Larmor frequency, and SOQE is, the *second order quadrupolar effect* parameter, given by:

$$\mathrm{SOQE} = C_Q\sqrt{1+\frac{\eta_Q^2}{3}}. \tag{2.115}$$

Chapter 3

Results and Discussion

3.1 Single-crystal NMR

Chemical shift tensors and their orientations carry information about the structure and the chemistry of samples. For single-crystals, the full tensorial properties are extracted using traditional goniometer probes which are not widely available [78–88]. An alternative method to measure chemical shift data including tensor orientations for single-crystals is rotorsynchronized magic angle spinning (MAS) NMR, introduced by Kunath-Fandrei *et al.* [101]. However, using rotorsynchronized MAS NMR the experimental determination of chemical shift tensors and their orientations are seldom reported. The following paper discusses the extension of the work done by Kunath-Fandrei *et al.* to establish this method as a routine tool for obtaining structural and orientational information of single-crystals. To this end, a necessary hardware assembly for mounting/remounting a single-crystal in the MAS rotor, a detail experimental protocol including pulse sequence, and an analytical function for the intensities and phases of the dispersive spinning sideband peaks are presented in the following paper.

3.2 Quantitative NMR

Many studies have reported on the use of NMR for quantitative analyses (qNMR) [103, 237], showing that NMR allows precise quantification [103, 111, 238, 239]. Accurate determination of ^{1}H NMR signal intensities is useful to the quantitative analysis of the hydrogen containing samples where combustion analysis fails. It also helps to determine the relative peak intensity ratios in different application scenarios. Solid-state qNMR described in the literature for highly resolved spectra has relied on the use of an external as well as internal standard [45, 105, 110, 113, 114]. Moreover, solid-state qNMR studies have highlighted different sources of errors, e.g. repetition delays [105, 110], spectrometer stability [114], pulse length effects [110], and packing effects [113, 114], which may lead to false intensities.

Quantification is straight forward for highly resolved spectra, whereas for low resolution spectra, small phase errors add a considerable amount of uncertainty. The following paper discusses different sources of errors which prevent ^{1}H quantification for poorly resolved spectra. To this end, a protocol is developed which reduces the error margin to a tolerable level for the quantification of poorly resolved ^{1}H NMR spectra and supported by an analytical expression for the phase induced intensity errors (paper-II). Further, this qNMR method is applied for the quantification of different hydrogen-bonded environments in the organic compound for example N-o-Vanillylidene-L-histidine (paper-III).

3.3 Solid-state NMR on Nanoparticles

The increasing use of engineered nanoparticles in research and product development in various application areas engenders a growing need to understand their properties and behaviors [119–126,151,152,240–242]. Solid-state NMR techniques gaining rapid importance in oder to probe spatial variations in nanoparticle composition, the interfacial structure, and other features on the nanometer scale [9, 18–22, 127].

It is widely recognized that as particle size decreases to the nanometer scale, that causes their physical and chemical properties to differ from those associated with their bulk form [243–245]. Equally important and widely acknowledged but seemingly less understood, is recognition that a large portion of atoms or point defects in nanoparticles are at or near the surface of the particles. Investigation of nanoparticle surface and homogeneous/core-shell structure is still a challenging task. In terms of chemical reactivity and interparticle interactions, the composition of the surface and the impact of doping on its properties are clearly most important [125] and leads to following questions. Is there an amorphous surface component? or are they with a hydrogenated surface? Are there dangling bonds at their surface? Are there many OH groups at the surface? Are point defects at the surface or in the core? Is host lattice distorted, and if so, why? Are these point defects homogeneous? Is the nature of these defects dynamic or static in the host lattice?

Many of these questions can be addressed by solid-state NMR spectroscopy. In this work, I present a novel solid-state NMR approach for quantitative internuclear distance measurements of their component ions or atoms from the organic-inorganic interfaces using a variant of rotational echo double resonance experiment [128] called C-REDOR [129, 130] as well as how to probe homogeneity and dynamic of the point defects, in the presence of background signal. In order to gain a detailed insight on these issues, a number of new techniques have been developed in this work, namely a new background compensated homonuclear recoupling experiment (2D-DEPTH-SR6$_6^2$), a modified background compensated two-dimensional exchange sequence (2D-DEPTH-EXSY) and modified a two-dimensional version of PRESTO-III.

A group of established and the above developed solid-state NMR techniques are applied in the following publications to characterize noncrystalline zincphosphate (paper-IV) as well as to study defect structure of Transparent Conducting Oxides (TCOs) namely fluorine doped tin oxide (FTO,SnO_2:F) and aluminum doped zinc oxide (AZO, ZnO:Al) (paper-V and paper-VI, respectively).

Chapter 4

Conclusions

The goal of this thesis was to develop and apply solid-state NMR methods which can be used as a routine tool for structural characterization of oriented or non-oriented (nano-)particles embedded in a matrix. From analytical point of view the focus was on the following aspects: 1) characterization of oriented particles which can be treated as single-crystals from NMR point of view, 2) quantification of the peak area under low resolution conditions, and 3) investigation of quantitative distance constraints and point defects analysis of nanomaterials using solid-state NMR techniques.

With respect to aspect 1), for the first time, a full implementation in theory and hardware of a magic angle spinning NMR method is demonstrated to obtain accurate chemical shift tensor orientations of single-crystals. A cost-effective homemade mounting tool provides the means for mounting and remounting a single-crystal inside magic angle spinning (MAS) rotor with high angular stability, which is a prerequisite for routine application of this method. An elaborate experimental protocol leads to determine tensor orientations as precise as with the traditional static single-crystal NMR below $\pm 1^{\circ}$. An analytical function has been derived to calculate the intensities and phases of the spinning sideband peaks which have a dispersive lineshape. The formula allows fast calculation of single-crystal MAS spectra which will help to develop a software for efficient deconvolution. The formula was validated by comparison with experimental spectra. This method offers large resolution enhancement, considerable time saving, use of standard MAS probes, and low cost in comparison to the traditional static single-crystal NMR. The potential advantage of this method is to gain better spectral resolution in case of small single-crystals due to suppression of dipole-dipole couplings by magic angle spinning. A foreseeable application is to obtain the chemical shift tensor orientations in partially oriented materials. Possible extensions of this method to the microcoil concept and piggy-back design as a routine/standard tool to achieve higher resolution. It should be possible to extend the presented method to determine the orientation of electric-field-gradient (EFG) tensors. Furthermore, it could become useful to study motion and dynam-

ics in crystals, for example ion dynamics, which would add a spatial dimension to the NMR analysis which is lacking in many of the standard NMR techniques.

With respect to aspect 2), a method has been developed to achieve reliable quantification of the hydrogen content even under low-resolution conditions. An easy, and unambiguous method using solid-state NMR has been established to seek the quantitative peak area information under limited spectral resolution. A robust protocol has been presented using the spin-echo experiment, an extrapolation technique, internal referencing and phase fitting to reestablish error margins similar to those under high resolution conditions. My results suggest that it is wise to avoid extreme intensity ratios between the peaks of the internal reference and the analyte in order to achieve accurate results. This approach can be transferred to other isotopes like, for example ^{19}F and ^{119}Sn. In fact the presented technique has found application in a number of chemical problems already, among the studied materials were nanoscale materials [246], organic compounds [117] and metal-organic frameworks [247].

With respect to aspect 3), an aggregation of established and modified multiple solid-state NMR techniques has been presented for the characterization of nanoscale materials. A number of techniques have been developed/introduced namely 2D-DEPTH-EXSY, 2D-DEPTH-SR6$^2_6$, and 2D-PRESTO-III to gain a detailed insight of nanomaterials. Determination of quantitative heteronuclear distance constraints in order to differentiate between homogeneous and core-shell particle structure has been successfully demonstrated using a variant of the rotational echo double resonance (REDOR) experiments called C-REDOR. Moreover, comparison of different flavors of REDOR experiments is possible for the same dipole-dipole coupling constant using the defined universal dephasing scale [248]. A combination of above developed solid-state NMR techniques could contribute for deeper understanding about homogeneity, dynamics, homo-, and heteronuclear connectivities of point defects, quantitative interatomic distances and structural models in nanoscale materials. Further, this improved and promising approach could assist to examine the macroscopically observed properties as a function of the particle composition and serve as a guide for the synthesis of nanoscale materials, especially in the context of Transparent Conducting Oxides (TCOs), as for example materials like nanoscale ZnO:Al (AZO) or nanoscale SnO_2:F (FTO) which investigated here.

Thus the above presented methodology could contribute individually or collectively to the analysis of oriented (nano-)particles embedded in amorphous matrices which might become a very powerful way of running solid-state NMR experiments.

Chapter 5

Summary

This thesis work summarizes the development and application of solid-state NMR spectroscopy which can contribute to the characterization of nanoscale materials and particles embedded in amorphous matrices.

1. An improved way for obtaining the chemical shift tensor orientations of a single crystal by a rotorsynchronized magic angle spinning NMR technique is established. A systematic experimental protocol to perform the chemical shift tensor analysis is presented. With the proposed hardware assembly, experimental data for different orientations can be determined with only small angular errors. An analytical function is derived to calculate the intensities and the phases of the dispersive spinning sideband peaks.

2. A solid-state NMR method is proposed to achieve reliable quantification of the hydrogen content under low resolution conditions. An experimental protocol is presented based on a combination of the spin echo experiment, an extrapolation technique, internal referencing and phase fitting. This protocol reduces relative errors to below 4.9%. An analytical expression is derived to assess the phase induced intensity errors. Moreover, the quantification method is applied to the quantification of different hydrogen-bonded environments in the organic compound for example N-o-Vanillylidene-L-histidine.

3. An application of established and improved solid-state NMR methods is demonstrated for the characterization of nanoscale materials. Quantitative heteronuclear distance constraints for core-shell model of nanoparticles are determined with a variant of the rotational echo double resonance (REDOR) experiments called C-REDOR. Further, the experimental C-REDOR curves for various spin topologies are analyzed analytically and numerically, in order to differentiate between particles which have a homogeneous structure and a core-shell structure. Additionally, the universal dephasing scale is defined to get a pulse sequence independent time-scale which allows to

compare the results from different flavors of REDOR experiments. To probe homogeneity of point defects in doped nanoscale materials, new background compensated homonuclear recoupling experiments (2D-DEPTH-SR6$_6^2$) are carried out. Dynamics of the point defects are studied using modified background compensated two dimensional exchange sequences (2D-DEPTH-EXSY). In order to investigate heteronuclear connectivity patterns between ^{27}Al and ^{1}H, modified a two-dimensional version of the PRESTO-III (Phase Shifted Recoupling Effects a Smooth Transfer of Order) experiment is implemented. Using above solid-state NMR methods, structural models of nanoparticles are proposed namely for zinc-phosphate, fluorine doped tin oxide (SnO_2:F, FTO) and aluminum doped zinc oxide (ZnO:Al, AZO).

Conference Contribution

Talks and Poster Presentation

1. "High-resolution solid state NMR analysis of surfaces and interfaces in aluminum doped ZnO nanoparticles."
   Y. S. Avadhut, J. Weber, E. Hammarberg, C. Feldmann, and J. Schmedt auf der Günne, EUROMAR 2011, August 21-25, 2011, Frankfurt am Main, Germany.

2. "Chemical shift tensors orientations and their correlation to the local structure in solids - a theoretical study."
   J. Weber, Y. S. Avadhut, and J. Schmedt auf der Günne, 32nd Discussion meeting Gesellschaft Deutscher Chemiker, September 20-23, 2010, Münster, Germany.

3. "Study on the defect structure of SnO_2:F nanoparticles by high-resolution solid state NMR."
   Y. S. Avadhut, J. Weber, E. Hammarberg, C. Feldmann, I. Schellenberg, R. Pöttgen, and J. Schmedt auf der Günne, VERHANDLUNGEN der Deutsche Physikalischen Gesellschaft, March 21-26, 2010, Regensburg, Germany.

4. "A method for improved quantification of ^{1}H NMR signals under low-resolution conditions for solids."
   Y. S. Avadhut, D. Schneider, and J. Schmedt auf der Günne, The 6th Alpine Conference on Solid State NMR, Chamonix-Mont Blanc, September 13-17, 2009, Chamonix, France.

5. "Polarized chain-structure and distribution function for inorganic glasses." J. Schmedt auf der Günne, S. Venkatachalam, J. Weber and Y. S. Avadhut, The 6th Alpine Conference on Solid State NMR, Chamonix-Mont Blanc, September 13-17, 2009, Chamonix France.

6. "Study on the defect structure of SnO_2:F nanoparticles by high-resolution solid state NMR."
Y. S. Avadhut, J. Weber, E. Hammarberg, C. Feldmann, I. Schellenberg, R. Pöttgen, and J. Schmedt auf der Günne, 30th Discussion meeting Gesellschaft Deutscher Chemiker, September 22-25, 2008, Regensburg, Germany.

7. "Interpretation of solid state NMR signals in crystalline compounds and disordered nanoparticles by EEIM calculations."
J. Weber, Y. S. Avadhut, and J. Schmedt auf der Günne, 30th Discussion meeting Gesellschaft Deutscher Chemiker, September 22-25, 2008, Regensburg, Germany.

8. "Characterization of nanoparticles by Solid State NMR."
Y. S. Avadhut and J. Schmedt auf der Günne, Hirschegg Seminar für Festkörperchemie, May 22-25,2008, Hirschegg, Austria.

9. "Characterization of covalent linkages in organically functionalized MCM-41 mesoporous materials by solid state NMR and theoretical calculations."
Y. S. Avadhut, J. W. Wiench, N. Maity, S. Bhaduri, G. K. Lahiri, M. Pruski, S. Ganapathy, 13th National Magnetic Resonance Society Meeting, February 5-8, 2007, India.

Appendices

Appendix A

Double Resonance Frequency Splitter

A.1 Introduction

To measure close frequencies such as ^{1}H (200.13 MHz) and ^{19}F (188.35 MHz), a double resonance ^{1}H-^{19}F frequency splitter box (DRFS) is necessary. In this appendix, design and construction of ^{1}H-^{19}F DRFS box is described based on the previous work of Hasse *et al.* [249].

A.2 Circuit Design

To allow the separation of the closely spaced ^{1}H-^{19}F [249] resonances in high-power experiments, a series resonant, capacitor coupled, band pass filter circuit is chosen (see Fig. A.1). This circuit consists of two parts. First part of the circuit is single channel probe form Bruker and second part of the circuit is the DRFS box as shown Fig. A.1. *ViPEC* software [250] is used to design the circuit and to find optimum values of the circuit components.

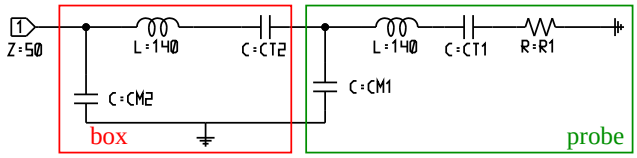

Figure A.1: Design of a series resonant circuit to separate closely spaced ^{1}H-^{19}F frequencies.

The probe and the DRFS box consist of an inductor (L) and matching and tuning capacitors (CM and CT), respectively. A sample coil inductance of 140 nH is chosen. Referring to this inductance, optimum values for tuning and matching

Table A.1: A range of tuning and matching capacitors for ^{1}H-^{19}F DRFS circuit.

	minimum capacitance/pF	maximum capacitance/pF	optimum capacitance/pF
CM1	50.0	92.0	74.57
CT1	4.0	6.0	5.12
CM2	100.0	110.0	109.6
CT2	4.0	6.0	5.3

capacitors are found by trial and error method. Table A.1 summarizes minimum to maximum range of the capacitors with their optimum values for both parts of the circuit. Using above circuit, scattering parameters S_{11} (reflection coefficient) are measured against signal frequencies for ^{1}H (200.13 MHz) and ^{19}F (188.35 MHz) as shown in Fig. A.2.

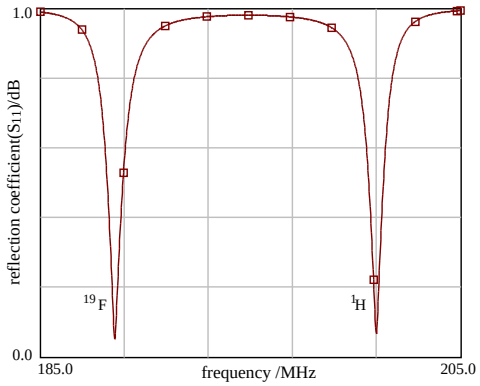

Figure A.2: Magnitude of the scattering parameter S_{11} (reflection coefficient) plotted against signal frequencies for ^{1}H (200.13 MHz) and ^{19}F (188.35 MHz) measured by the *ViPEC* software.

A high pass filter (Fig A.3 (a)) is designed to allow passing ^{1}H and ^{19}F frequencies. Fig. A.3 (b) shows the cutoff frequency as measured on the *ViPEC* software.

A cutoff frequency f_c, at which the output power is half of the input power as defined below; is inversely proportional to product of inductance and capacitance.

$$f_c = \frac{1}{2\pi LC} \tag{A.1}$$

where f_c is in Hertz.

An optimum value of the capacitance and inductance for the high pass filter are obtained for passing ^{1}H and ^{19}F frequency. The obtained values of capacitance and inductance by using *ViPEC* software are 10 pF and 30 nH, respectively.

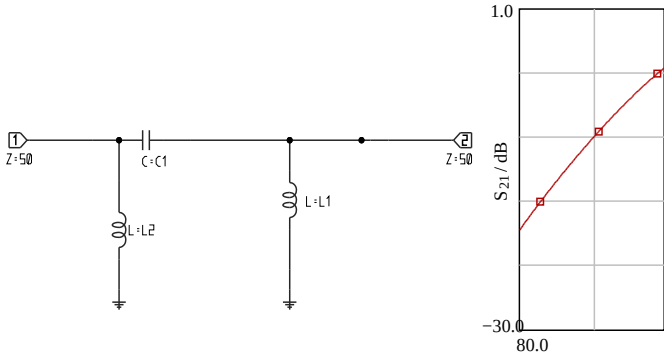

(a)

Figure A.3: (a) Circuit design for high pass filter (b) scattering parameter S_{21} plotted against signal frequency measured by the *ViPEC* software.

A.3 Testing and Implementation

The above circuit design is implemented in the laboratory. The coils are constructed by winding from silver plated copper wire (Nr. 605638, Conrad) with diameter of 1.0 mm around a rod. The resulting coil of 140 nH has five-turn with a 8.0 mm outer diameter. The inductance of the resulting coil is measured by using *BK PRECISION* 889A Bench LCR/ESR meter. Tuning and matching capacitors are chosen so as to be non-magnetic, small in size with obtained optimum capacitance (see Table. A.1). NMNT85 and NMQM22G trimmer capacitors from Voltronics (Denville, NJ) are used. The resulting DRFS box as shown in Fig. A.4.

The DRFS box is tested on the Agilent 8712ES RF vector network analyzer (300 kHz-1300 MHz) and the obtained result (as shown in Fig. A.2) verify the circuit designed using the *ViPEC* software.

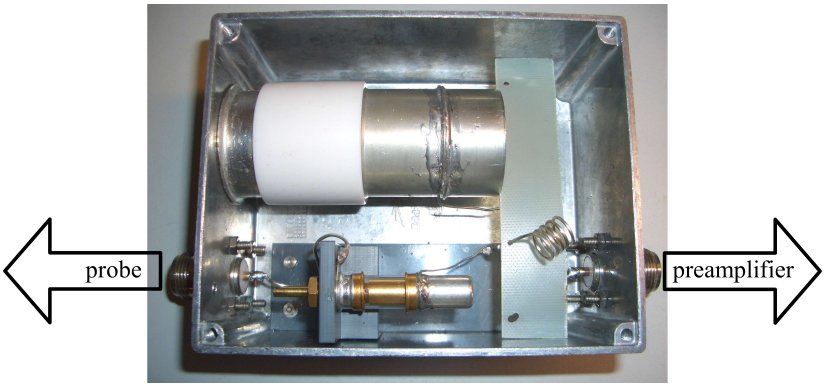

Figure A.4: The ^{1}H-^{19}F double resonance frequency splitter box.

The high pass filter is constructed based on the values obtained by the circuit

($C = 10$ pF and $L = 30$ nH) design using the *ViPEC* software is shown in Fig. A.5 (a) with cutoff frequency of 80 MHz at -20 dB shown on the vector network analyzer as in Fig. A.6.

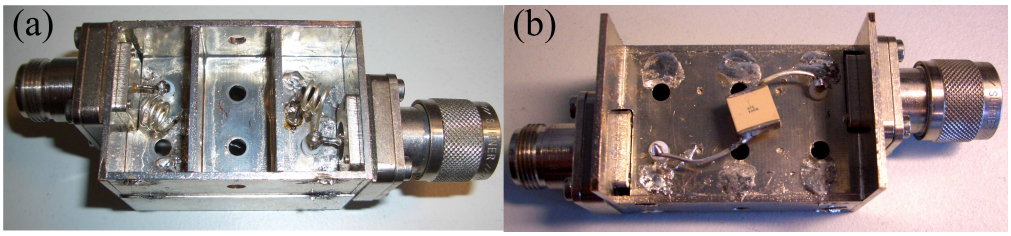

Figure A.5: The designed high pass filter, (a) showing home-made coil with $L = 30$ nH and (b) capacitor having $C = 10$ pF.

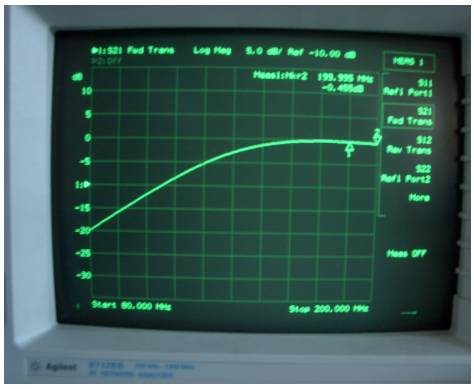

Figure A.6: Cutoff frequency of the high pass filter is 80 MHz at -20 dB is shown on the vector network analyzer.

A.4 Results

The home built ^{1}H-^{19}F double resonance frequency splitter box along with the designed high pass filter is then tested on Bruker Avance II-200 spectrometer for 1D ^{13}C{^{19}F} CP-MAS NMR experiment of Polytetrafluoroethylene (Teflon). Before starting the experiment, final tuning and matching of the probe is done by adjusting the CT1-CM1 and CT2-CM2 (see Fig.A.1) capacitors for the ^{1}H and the ^{19}F channel, respectively. The 1D ^{13}C{^{19}F}CP-MAS NMR experiments are performed with and without the ^{1}H-^{19}F double resonance frequency splitter box and the high pass filter as compared in Fig. A.7, using same experimental conditions.

It is observed that the line-width, intensity and the S/N ratio are comparable to the spectrum without the ^{1}H-^{19}F double resonance frequency splitter box. ^{1}H-^{19}F double resonance frequency splitter box has damping factor of -6.65±0.01 dB

at Larmor frequency of 188.35 MHz and -8.72±0.01 dB at Larmor frequency of 200.13 MHz for ^{19}F and for ^{1}H, respectively. Finally, this home built ^{1}H-^{19}F double resonance frequency splitter box is implemented for 2D ^{19}F{^{1}H} C-REDOR experiments (see section 3.3)

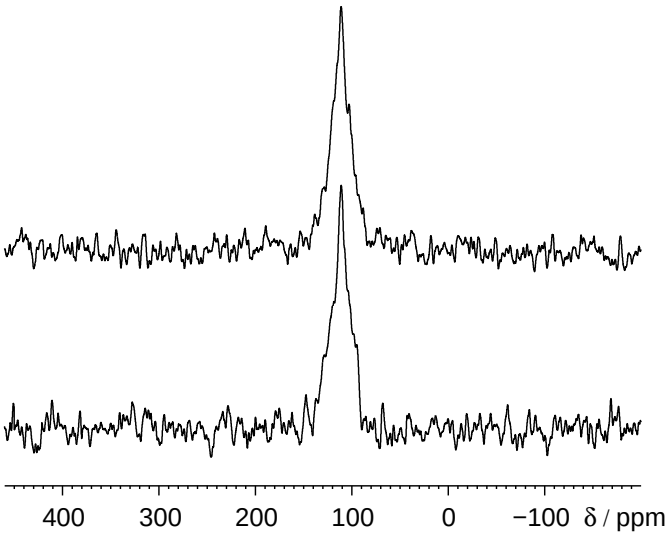

Figure A.7: 1D ^{13}C{^{19}F} CP-MAS NMR spectra of Teflon (top) with the ^{1}H-^{19}F double resonance frequency splitter box and the high pass filter, (bottom) without ^{1}H-^{19}F double resonance frequency splitter box and the high pass filter, are obtained at a sample spinning frequency of 8 kHz, using same experimental conditions.

Appendix B

Hardware Assembly for Single-Crystal MAS NMR

Single-crystal MAS NMR requires mounting of a single-crystal in a MAS rotor with a specific orientation (in our case single-crystal of about 1 mm^3). The presented equipment is designed for single-crystal MAS NMR to fill a 4 mm Bruker rotor. The following two homemade equipments are described below by which one can use the standard MAS probe for single-crystal MAS NMR experiment. The first part is a single-crystal mounting equipment. The second part is a rotor with three parts namely, specially designed rotor insert with bottom cap as a single unit, the both open ended MAS rotor, and a drive cap.

B.1 Single-crystal Mounting Tool

A single-crystal mounting tool is designed to transfer a crystal orientation information from a diffractometer into a MAS rotor insert as shown in Fig. B.1 (right).

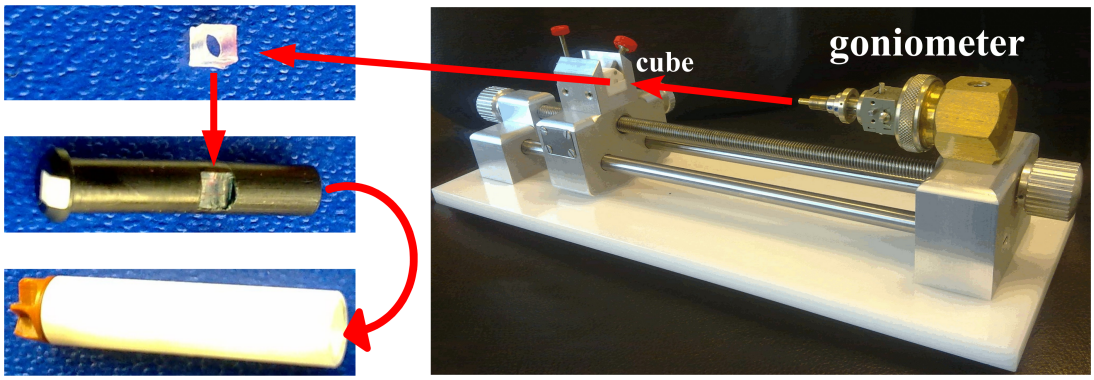

Figure B.1: Complete hardware assembly for single-crystal magic angle spinning NMR experiment.

A single-crystal orientation is measured using a standard goniometer on an X-ray diffractometer. Using this mounting tool the single-crystal with known orientation is transferred from goniometer into a cylindrical void of the cube with 2 mm^3 dimension. The single-crystal is glued into the cube using suitable glue (I used 2-components epoxy resine). This sample cube is then inserted into the cubical hole of the specially designed rotor insert which is of the exact dimensions as the sample cube as shown in Fig. B.1 (left). Further, rotor insert is then transferred in a both open ended 4 mm ZrO_2 MAS rotor. For more details see paper-I.

The most challenging task in the hardware assembly was the rotor insert design which is explained below.

B.2 Development of a Rotor Insert

The rotor insert turned out to be difficult to realize because the optical detection of the sample rotation, and the strength and magnetic properties of the plastics require a specific combination of different black and white polymers. Fig. B.2 shows six different versions of the rotor insert design manufactured by our mechanical workshop.

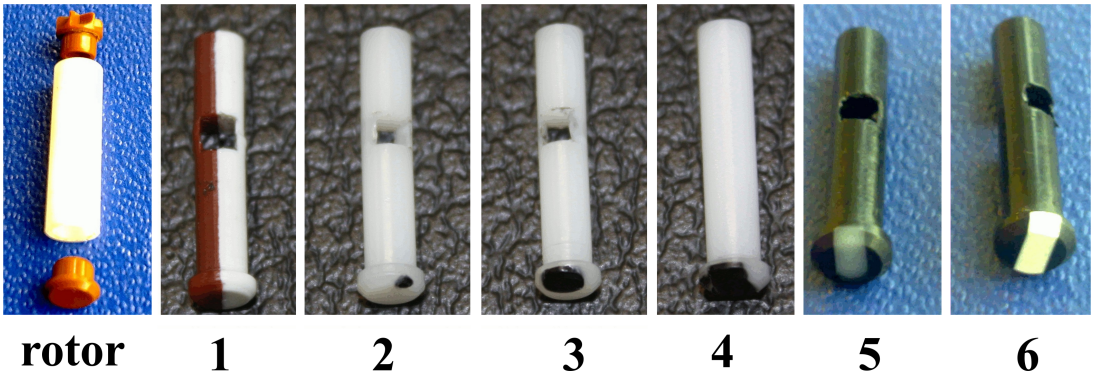

Figure B.2: Different generations of the single-crystal insert for magic angle spinning rotors using polyvinylchloride (PVC) and polyoxymethylene (POM) which were manufactured by our mechanical workshop.

The first rotor insert design made up of two different polyvinylchloride (PVC) (B.2, 1). Eventhough this rotor design showed stable spinning frequency, it was not robust and frequently damaged while mounting-remounting the sample cube. The next versions of rotor insert (B.2, 2-4) were prepared using white polyoxymethylene (POM). To achieve the black and white contrast for spin detection, black POM rods with different sizes were forcefully pressed in the bottom cap of the insert. The second version of rotor insert was robust, optically detectable but unstable while spinning. The subsequent versions (3) and (4) failed to achieve the

spin detection. In version (5) the rotor insert was designed using black POM, and a white POM strip is glued on the half middle strip of the bottom cap. Although this rotor design was robust but fails to achieve the necessary black and white contrast for spin detection. The problem of optical detection is solved in version (6). In this rotor insert design, a small middle strip of the bottom cap is replaced by white PVC to achieve the fixed light detection mark on the MAS rotor for spin detection.

To glue the PVC strip with the bottom cap of the POM rotor insert, the surface of the POM part is treated using chromic sulphuric acid. The bottom cap of the POM rotor insert is dipped for two-three seconds in the solution of chromic sulphuric acid which is preheated to about 100 °C. This chemical pre-treatment oxidizes the surface of the bottom cap of the POM rotor insert. Further, it is washed and dried in air for 20 minutes. Finally, white PVC strip is glued to the bottom cap of the POM rotor insert using a 2-component epoxy glue for 12 hours.

This rotor insert design is robust and achieves stable spinning frequency upto 10 ± 0.001 kHz which is then used for single-crystal MAS NMR (paper-I).

Fig. B.3 describes experimental set up for parallel (Fig. B.3, b) and perpendicular (Fig. B.3, c) orientation of a sample cube (W-frame) in the MAS rotor insert (R-frame). A cube is marked with blue, red and green color to define its three axes (Fig. B.3, a).

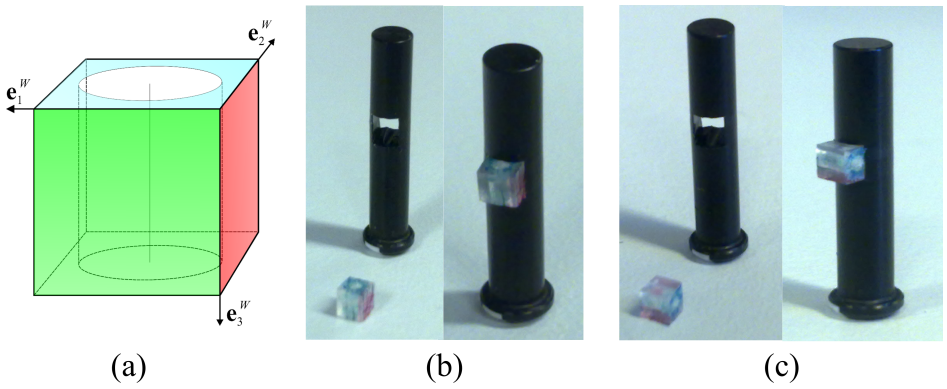

Figure B.3: Experimental set up: (a) a sample cube marked with three different colors, (b) parallel orientation of the cube in the rotor insert, and (c) perpendicular orientation of the cube in the rotor insert.

Appendix C

SIMPSON Input File for Single-Crystal MAS NMR Simulation

C.1 Input File

The following SIMPSON input file is used for simulation of the two orientations of single-crystal MAS NMR data simultaneously. The comments are highlighted in green color.

The following tcl-procedure switches description of the chemical shift (δ_{iso}). Principal axes values are order by absolute value: $\delta_{11} > \delta_{22} > \delta_{33}$, span $= \delta_{11} - \delta_{33}$, gravity $= \delta_{22} - \delta_{33}$/span
This set is called simulation representation and thus diagonal2sim. It takes values in ppm and Hertz.

```
proc cs_diagonal2sim {delta_xx delta_yy delta_zz} {
    if {[llength [regexp -inline -all -- {^(\-?\d+\.?\d* (?:e[+-]\d\d)?p$)}
                                                    $delta_xx]] == 2 && \
        [llength [regexp -inline -all -- {^(\-?\d+ \.?\d*(?:e[+-]\d\d)?p$)}
                                                    $delta_yy]] == 2 && \
        [llength [regexp -inline -all -- {^(\-?\d+\.?\d* (?:e[+-]\d\d)?p$)}
                                                    $delta_zz]] == 2} {
        set delta_xx [string map {p " "} $delta_xx]
        set delta_yy [string map {p " "} $delta_yy]
        set delta_zz [string map {p " "} $delta_zz]
    } elseif {[llength [regexp -inline -all -- {^(\-?\d+ \.?\d*$(?:e[+-]\d\d)?)
                                                    }$delta_xx]] == 2 && \
        [llength [regexp -inline -all -- {^(\-?\d+\.?\d* $(?:e[+-]\d\d)?)}
```

```
                                                    $delta_yy]] == 2 && \
      [llength [regexp -inline -all -- {^(\-?\d+\.?\d* $(?:e[+-]\d\d)?)}
                                                    $delta_zz]] == 2} {
    set memppm 0
    } else {
       puts "error in chemical shift parameters: \n$delta_xx $delta_yy $delta_zz"
       puts "PROC in cs_diagonal2sim"
       puts "cs_diagonal2sim needs either ppm or Hz for all three variables"
       exit 0
    }
    set iso [expr 1.0/3*($delta_xx+$delta_yy+$delta_zz)]
    lappend sortlist $delta_xx $delta_yy $delta_zz
    set sortlist [lsort -decreasing -real $sortlist]
    set span [expr [lindex $sortlist 0]-[lindex $sortlist 2]]
    set gravity [expr ([lindex $sortlist 1]-[lindex $sortlist 2])/$span]
    if {$memppm} {
       append iso p
       append span p
    }
    lappend sim $iso $span $gravity
    return $sim
}

proc cs_sim2diagonal {delta_iso span gravity} {
    if {[llength [regexp -inline -all -- {^(\-?\d+\.?\d* (?:e[+-]\d\d)?p$)}
                                                    $delta_iso]] == 2 && \
      [llength [regexp -inline -all -- {^(\-?\d+\.?\d* (?:e[+-]\d\d)?p$)}
                                                    $span]] == 2 && \
      [llength [regexp -inline -all -- {^(\-?\d+\.?\d* (?:e[+-]\d\d)?$)}
                                                    $gravity]] == 2} {
    set memppm 1
    set delta_iso [string map {p " "} $delta_iso]
    set span [string map {p " "} $span]
    } elseif {[llength [regexp -inline -all -- {^(\-?\d+\.?\d* (?:e[+-]\d\d)?$)}
                                                    $delta_iso]] == 2 && \
      [llength [regexp -inline -all -- {^(\-?\d+\.?\d* (?:e[+-]\d\d)?$)}
                                                    $span]] == 2 && \
      [llength [regexp -inline -all -- {^(\-?\d+\.?\d* (?:e[+-]\d\d)?$)}
                                                      $gravity]] == 2} {
    set memppm 0
    } else {
       puts "error in chemical shift parameters: \n$delta_xx $delta_yy $delta_zz"
       puts "PROC in cs_sim2diagonal"
```

```
        puts "cs_sim2diagonal needs span and delta_iso either in ppm or Hz"
        exit 0
    }
    set delta_33 [expr (3.0*$delta_iso-$gravity*$span-$span)/3.0]
    set delta_22 [expr $gravity*$span+$delta_33]
    set delta_11 [expr $span+$delta_33]
    if {$memppm} {
        append delta_33 p
        append delta_22 p
        append delta_11 p
    }
    lappend diagonal $delta_11 $delta_22 $delta_33
    return $diagonal
}
```

The following tcl-procedure reads a file (e.g. "name_of_raw_file") and writes a string into a file.

```
package provide readwrite 0.1

proc readcoordXYZ {filenameXYZ} {
    set linesXYZ [readrawfile $filenameXYZ]
    set numberofatoms [lindex $linesXYZ 0]
    for {set i 0} {$i < $numberofatoms} {incr i} {
        set string " "
        set atomcoordinate [lindex $linesXYZ [expr 2+$i]]
        set atomcoordinate [string map . _ - x $atomcoordinate]
        for {set j 0} {$j < 4} {incr j} {
            set atomcoordinate [string trimleft $atomcoordinate]
            set first [string wordstart $atomcoordinate 0]
            set last [string wordend $atomcoordinate 0]
            lappend string [string range $atomcoordinate $first [expr $last-1]]
            set atomcoordinate [string replace $atomcoordinate $first $last " "]
        }
        lappend coordinates $string
    }
    set coordinates [string map {_ . x -} $coordinates]
    return $coordinates
}

proc readrawfile {name_of_raw_file} {
    if {[file exists $name_of_raw_file]} {
        if [catch {open $name_of_raw_file RDONLY} f] {
        } else {
```

```
            while {1} {
                gets $f zeile
                    if [eof $f] break
                lappend field_of_ref $zeile
            }
            close $f
        }
    } else {
        puts "File $name_of_raw_file does not exist!"
        exit
    }
    return $field_of_ref
}

proc string2file {string nameoffile {boolappend 0}} {
    if {1!=$boolappend} {
        file delete -force $nameoffile
    }
    set channel [open $nameoffile a+]
    open $nameoffile
    puts $channel $string
    eof $channel
    close $channel
}
```

The following tcl-procedure calculates a set Euler anlgles (α_{BD}, β_{BD}, γ_{BD}) from given direction cosines according to ROSE convention.

```
proc DirectionCosineToEulerAngles {listofdirecosine} {
    set XD [list 1.0 0.0 0.0]
    set YD [list 0.0 1.0 0.0]
    set ZD [list 0.0 0.0 1.0]
    set pi 3.1415926535897932
    set XA [list [lindex [lindex $listofdirecosine 0] 0]
          [lindex [lindex $listofdirecosine 0] 1] [lindex [lindex $listofdirecosine 0] 2]]
    set YA [list [lindex [lindex $listofdirecosine 1] 0]
          [lindex [lindex $listofdirecosine 1] 1] [lindex [lindex $listofdirecosine 1] 2]]
    set ZA [list [lindex [lindex $listofdirecosine 2] 0]
          [lindex [lindex $listofdirecosine 2] 1] [lindex [lindex $listofdirecosine 2] 2]]
    set norm 0.0
    set n1 [expr ([lindex $ZA 1]*[lindex $ZD 2])-([lindex $ZD 1]*[lindex $ZA 2])]
    set n2 [expr ([lindex $ZA 2]*[lindex $ZD 0])-([lindex $ZD 2]*[lindex $ZA 0])]
    set n3 [expr ([lindex $ZA 0]*[lindex $ZD 1])-([lindex $ZD 0]*[lindex $ZA 1])]
```

```
set sum_n [expr ($n1*$n1)+($n2*$n2)+($n3*$n3)]
set norm [expr $norm+sqrt($sum_n)]
set alpha_BD 0.0
set beta_BD 0.0
set gamma_BD 0.0
if {[expr {$norm !=0.0}]} {
   puts "beta_BD is not equal to ZERO"
   set n1norm [expr {$n1/$norm}]
   set n2norm [expr {$n2/$norm}]
   set n3norm [expr {$n3/$norm}]
   set n [list $n1norm $n2norm $n3norm]
   set k1 [expr {([lindex $YA 1]*[lindex $n 2])-([lindex $n 1]*[lindex $YA 2])}]
   set k2 [expr {([lindex $YA 2]*[lindex $n 0])-([lindex $n 2]*[lindex $YA 0])}]
   set k3 [expr {([lindex $YA 0]*[lindex $n 1])-([lindex $n 0]*[lindex $YA 1])}]
   set kvec [list $k1 $k2 $k3]
   set kZA [expr {([lindex $kvec 0]*[lindex $ZA 0])+([lindex $kvec 1]*
                        [lindex $ZA 1])+([lindex $kvec 2]*[lindex $ZA 2])}]
   set YAn [expr {([lindex $YA 0]*[lindex $n 0])+([lindex $YA 1]*
                        [lindex $n 1])+([lindex $YA 2]*[lindex $n 2])}]
   if {$YAn > 1.0} {
      set YAn 1.0
   } elseif {$YAn < -1.0} {
      set YAn -1.0
   }
   if {[expr $kZA > 0.0]} {
      set alpha_BD [expr {$alpha_BD+(acos($YAn)*180.0/$pi)}]
   } else {
      set alpha_BD [expr {$alpha_BD+(360.0-(acos($YAn)*180.0/$pi))}]
   }
   set ZAZD [expr {([lindex $ZA 0]*[lindex $ZD 0])+([lindex $ZA 1]*
                        [lindex $ZD 1])+([lindex $ZA 2]*[lindex $ZD 2])}]
   if {$ZAZD > 1.0} {
      set ZAZD 1.0
   } elseif {$ZAZD < -1.0} {
      set ZAZD -1.0
   }
   set beta_BD [expr {$beta_BD+(acos($ZAZD)*180.0/$pi)}]
   set p1 [expr {([lindex $n 1]*[lindex $YD 2])-([lindex $YD 1]*[lindex $n 2])}]
   set p2 [expr {([lindex $n 2]*[lindex $YD 0])-([lindex $YD 2]*[lindex $n 0])}]
   set p3 [expr {([lindex $n 0]*[lindex $YD 1])-([lindex $YD 0]*[lindex $n 1])}]
   set p [list $p1 $p2 $p3]
   set pZD [expr {([lindex $p 0]*[lindex $ZD 0])+([lindex $p 1]*
                        [lindex $ZD 1])+([lindex $p 2]*[lindex $ZD 2])}]
```

```
        set nYD [expr {([lindex $n 0]*[lindex $YD 0])+([lindex $n 1]*
                                    [lindex $YD 1])+([lindex $n 2]*[lindex $YD 2])}]
        if {$nYD > 1.0} {
            set nYD 1.0
        } elseif {$nYD < -1.0} {
            set nYD -1.0
        }
        if {[expr $pZD > 0.0]} {
            set gamma_BD [expr {$gamma_BD+(acos($nYD)*180.0/$pi)}]
        } else {
            set gamma_BD [expr {$gamma_BD+(360.0-(acos($nYD)*180.0/$pi))}]
        }
    } else {
        puts "beta_BD and gamma_BD is equal to ZERO"
        set beta_BD $beta_BD
        set gamma_BD $gamma_BD
        set XAXD [expr {([lindex $XA 0]*[lindex $XD 0])+([lindex $XA 1]*
                                    [lindex $XD 1])+([lindex $XA 2]*[lindex $XD 2])}]
        set YAXD [expr {([lindex $YA 0]*[lindex $XD 0])+([lindex $YA 1]*
                                    [lindex $XD 1])+([lindex $YA 2]*[lindex $XD 2])}]
        set alpha_BD [expr {$alpha_BD+(atan2($YAXD, $XAXD)*180.0/$pi)}]
        if {[expr $alpha_BD < 0.0]} {
            set alpha_BD [expr {$alpha_BD+360.0}]
        } else {
            set alpha_BD $alpha_BD
        }
    }
    set EulerAngles [list $alpha_BD $beta_BD $gamma_BD]
    return [list $EulerAngles]
}
```

The following tcl-procedure calculates direction cosines from a given set Euler anlgles (α_{BD}, β_{BD}, γ_{BD}) according to ROSE convention.

```
proc EulerAngleToDirectionCosine {alpha beta gamma} {
    set XD [list 1.0 0.0 0.0]
    set YD [list 0.0 1.0 0.0]
    set ZD [list 0.0 0.0 1.0]
    set pi 3.1415926535897932
    set alpha_rad [expr {$alpha/180.0*$pi}]
    set beta_rad [expr {$beta/180.0*$pi}]
    set gamma_rad [expr {$gamma/180.0*$pi}]
    set cos_alpha [expr {cos($alpha_rad)}]
```

```
set sin_alpha [expr {sin($alpha_rad)}]
set cos_beta [expr {cos($beta_rad)}]
set sin_beta [expr {sin($beta_rad)}]
set cos_gamma [expr {cos($gamma_rad)}]
set sin_gamma [expr {sin($gamma_rad)}]
set RzA_alpha [list [list $cos_alpha [expr {-1.0*$sin_alpha}] 0.0]
                    [list $sin_alpha $cos_alpha 0.0] [list 0.0 0.0 1.0]]
set RyB_beta [list [list $cos_beta 0.0 $sin_beta] [list 0.0 1.0 0.0]
                   [list [expr {-1.0*$sin_beta}] 0.0 $cos_beta]]
set RzC_gamma [list [list $cos_gamma [expr {-1.0*$sin_gamma}] 0.0]
                    [list $sin_gamma $cos_gamma 0.0] [list 0.0 0.0 1.0]]
set RzA_alphaT [list [list $cos_alpha $sin_alpha 0.0] [list [expr {-1.0*$sin_alpha}]
                                                           $cos_alpha 0.0] [list 0.0 0.0 1.0]]
set RyB_betaT [list [list $cos_beta 0.0 [expr {-1.0*$sin_beta}]] [list 0.0 1.0 0.0]
                                                            [list $sin_beta 0.0 $cos_beta]]
set RzC_gammaT [list [list $cos_gamma $sin_gamma 0.0]
                     [list [expr {-1.0*$sin_gamma}] $cos_gamma 0.0] [list 0.0 0.0 1.0]]
set RotationMatrix_row1 [list [expr {($cos_alpha*$cos_beta*$cos_gamma)
    -($sin_alpha*$sin_gamma)}] [expr {($cos_beta*$cos_gamma*$sin_alpha)
        +($cos_alpha*$sin_gamma)}] [expr {-1.0*$cos_gamma*$sin_beta}]]
set RotationMatrix_row2 [list [expr {(-1.0*$cos_gamma*$sin_alpha)
    -($cos_alpha*$cos_beta*$sin_gamma)}] [expr {($cos_alpha*$cos_gamma)
    -($cos_beta*$sin_alpha*$sin_gamma)}] [expr {$sin_beta*$sin_gamma}]]
set RotationMatrix_row3 [list [expr {$cos_alpha*$sin_beta}]
                              [expr {$sin_alpha*$sin_beta}] [expr {$cos_beta}]]
set Inverse_RotationMatrix_row1 [list [lindex $RotationMatrix_row1 0]
      [lindex $RotationMatrix_row2 0] [lindex $RotationMatrix_row3 0]]
set Inverse_RotationMatrix_row2 [list [lindex $RotationMatrix_row1 1]
        [lindex $RotationMatrix_row2 1] [lindex $RotationMatrix_row3 1]]
set Inverse_RotationMatrix_row3 [list [lindex $RotationMatrix_row1 2]
        [lindex $RotationMatrix_row2 2] [lindex $RotationMatrix_row3 2]]
set DirCosineX [list [expr {[lindex $Inverse_RotationMatrix_row1 0]*
        [lindex $XD 0]}] [expr {[lindex $Inverse_RotationMatrix_row1 1]*
        [lindex $XD 0]}] [expr {[lindex $Inverse_RotationMatrix_row1 2]*
                                [lindex $XD 0]}]]
set DirCosineY [list [expr {[lindex $Inverse_RotationMatrix_row2 0]*
        [lindex $YD 1]}] [expr {[lindex $Inverse_RotationMatrix_row2 1]*
        [lindex $YD 1]}] [expr {[lindex $Inverse_RotationMatrix_row2 2]*
                                [lindex $YD 1]}]]
set DirCosineZ [list [expr {[lindex $Inverse_RotationMatrix_row3 0]*
        [lindex $ZD 2]}] [expr {[lindex $Inverse_RotationMatrix_row3 1]*
        [lindex $ZD 2]}] [expr {[lindex $Inverse_RotationMatrix_row3 2]*
                                [lindex $ZD 2]}]]
```

```
    return [list $DirCosineX $DirCosineY $DirCosineZ]
}
```

The following tcl-procedure multiplies two matrices.

```
proc MatrixMultiplication {matrix1 matrix2} {
    set XD1 [expr {([lindex [lindex $matrix1 0] 0]*[lindex [lindex $matrix2 0]
                0])+([lindex [lindex $matrix1 0] 1]*[lindex [lindex $matrix2 1] 0])
                +([lindex [lindex $matrix1 0] 2]*[lindex [lindex $matrix2 2] 0])}]
    set XD2 [expr {([lindex [lindex $matrix1 0] 0]*[lindex [lindex $matrix2 0]
                1])+([lindex [lindex $matrix1 0] 1]*[lindex [lindex $matrix2 1] 1])
                +([lindex [lindex $matrix1 0] 2]*[lindex [lindex $matrix2 2] 1])}]
    set XD3 [expr {([lindex [lindex $matrix1 0] 0]*[lindex [lindex $matrix2 0]
                2])+([lindex [lindex $matrix1 0] 1]*[lindex [lindex $matrix2 1] 2])
                +([lindex [lindex $matrix1 0] 2]*[lindex [lindex $matrix2 2] 2])}]
    set XD [list $XD1 $XD2 $XD3]

    set YD1 [expr {([lindex [lindex $matrix1 1] 0]*[lindex [lindex $matrix2 0]
                0])+([lindex [lindex $matrix1 1] 1]*[lindex [lindex $matrix2 1] 0])
                +([lindex [lindex $matrix1 1] 2]*[lindex [lindex $matrix2 2] 0])}]
    set YD2 [expr {([lindex [lindex $matrix1 1] 0]*[lindex [lindex $matrix2 0]
                1])+([lindex [lindex $matrix1 1] 1]*[lindex [lindex $matrix2 1] 1])
                +([lindex [lindex $matrix1 1] 2]*[lindex [lindex $matrix2 2] 1])}]
    set YD3 [expr {([lindex [lindex $matrix1 1] 0]*[lindex [lindex $matrix2 0]
                2])+([lindex [lindex $matrix1 1] 1]*[lindex [lindex $matrix2 1] 2])
                +([lindex [lindex $matrix1 1] 2]*[lindex [lindex $matrix2 2] 2])}]
    set YD [list $YD1 $YD2 $YD3]

    set ZD1 [expr {([lindex [lindex $matrix1 2] 0]*[lindex [lindex $matrix2 0]
                0])+([lindex [lindex $matrix1 2] 1]*[lindex [lindex $matrix2 1] 0])
                +([lindex [lindex $matrix1 2] 2]*[lindex [lindex $matrix2 2] 0])}]
    set ZD2 [expr {([lindex [lindex $matrix1 2] 0]*[lindex [lindex $matrix2 0]
                1])+([lindex [lindex $matrix1 2] 1]*[lindex [lindex $matrix2 1] 1])
                +([lindex [lindex $matrix1 2] 2]*[lindex [lindex $matrix2 2] 1])}]
    set ZD3 [expr {([lindex [lindex $matrix1 2] 0]*[lindex [lindex $matrix2 0]
                2])+([lindex [lindex $matrix1 2] 1]*[lindex [lindex $matrix2 1] 2])
                +([lindex [lindex $matrix1 2] 2]*[lindex [lindex $matrix2 2] 2])}]
    set ZD [list $ZD1 $ZD2 $ZD3]

    return [list $XD $YD $ZD]
}
```

The following tcl-procedure creates new direction cosines according to symme-

try operation.

```
proc Symmetry {direcosinelist symmoperation} {
    for {set z 0} {$z < 4} {incr z} {
    set NewDirCosineX1 [expr {[lindex [lindex $direcosinelist 0] 0]*
                                    double([lindex [lindex $symmoperation $z] 0])}]
    set NewDirCosineX2 [expr {[lindex [lindex $direcosinelist 0] 1]*
                                    double([lindex [lindex $symmoperation $z] 1])}]
    set NewDirCosineX3 [expr {[lindex [lindex $direcosinelist 0] 2]*
                                    double([lindex [lindex $symmoperation $z] 2])}]
    set NewDCX [list $NewDirCosineX1 $NewDirCosineX2 $NewDirCosineX3]

    set NewDirCosineY1 [expr {[lindex [lindex $direcosinelist 1] 0]*
                                    double([lindex [lindex $symmoperation $z] 0])}]
    set NewDirCosineY2 [expr {[lindex [lindex $direcosinelist 1] 1]*
                                    double([lindex [lindex $symmoperation $z] 1])}]
    set NewDirCosineY3 [expr {[lindex [lindex $direcosinelist 1] 2]*
                                    double([lindex [lindex $symmoperation $z] 2])}]
    set NewDCY [list $NewDirCosineY1 $NewDirCosineY2 $NewDirCosineY3]

    set NewDirCosineZ1 [expr {[lindex [lindex $direcosinelist 2] 0]*
                                    double([lindex [lindex $symmoperation $z] 0])}]
    set NewDirCosineZ2 [expr {[lindex [lindex $direcosinelist 2] 1]*
                                    double([lindex [lindex $symmoperation $z] 1])}]
    set NewDirCosineZ3 [expr {[lindex [lindex $direcosinelist 2] 2]*
                                    double([lindex [lindex $symmoperation $z] 2])}]
    set NewDCZ [list $NewDirCosineZ1 $NewDirCosineZ2 $NewDirCosineZ3]

    set NewDClist [list $NewDCX $NewDCY $NewDCZ]
    }
    return $NewDClist
}

spinsys {
   channels 13C
   nuclei 13C
   shift 1 0.0p -70.73211p 0.77192 348.785 93.4101 127.324
}

par {

        proton_frequency    500.249278e6
        method              direct
```

```
        spin_rate           1500
        # gamma_angles      1
        gamma_zero          0
        np                  4096
        crystal_file        alphaXbetaY.cry
        use_3_angle_set     1
        start_operator      Inz
        detect_operator     Inp
        verbose             0
        variable nstep      20.0
        variable sw_exp     24000
        variable np_exp     4096
        variable pstep      20
        variable exp1       664.16667
        variable exp2       665.41667
        variable flipangle  90
        variable rf_field   100000
        variable offangle   0.0
        variable trigtime   505.62963
        sw                  spin_rate*pstep

}
proc pulseq {} {
   global par rotordelay mn
   matrix set 1 totalcoherence {1}
   matrix set 2 totalcoherence {-1}
   maxdt [expr 1.0e6/$par(spin_rate)/100]
   set startdelay [expr {(1.0e6/$par(spin_rate))*$rotordelay+$par(trigtime)}]
   set pulselength [expr 1.0e6/$par(rf_field)*$par(flipangle)/360.0]
   for {set i 0} {$i < $par(pstep)} {incr i} {
      reset [expr $i*1.0e6/$par(spin_rate)/$par(pstep)+
                        $pulselength*3.0+$par(exp1)+$par(exp2)+$startdelay]
      delay [expr 1.0e6/$par(spin_rate)/$par(pstep)]
      store $i
   }
   reset
   delay [expr {$startdelay}]
   pulse $pulselength $par(rf_field) 90
   delay $par(exp1)
   filter 1     pulse [expr {2.0*$pulselength}] $par(rf_field) 0
   filter 2
   delay $par(exp2)
```

```
    acq
    for {set i 0} {$i < [expr {$par(np)-1}]} {incr i} {
        prop [expr $i%$par(pstep)]
        acq
    }
}

proc minuit {} {
    global mn g p firstorien secondorien par spinsys rotordelay
    set par(spin_rate) $mn(mas)
    set par(trigtime) $mn(trigtime)
    set par(sw) [expr {$par(spin_rate)*$par(pstep)}]
    set namesmn [array names mn]
    set numberofspins [llength $spinsys(nuclei)]
    puts "numberofspins=$numberofspins"
    if {[llength $spinsys(channels)]!=1} {
        puts "I can't handle spinsystems with more than one nuclear species yet."
        exit 0
    }
    set totalnormfact 0.0
    set totalchisq 0.0
    set generator [list [list 1.0 1.0 1.0] [list -1.0 -1.0 1.0] [list -1.0 1.0 -1.0]
                                                                  [list 1.0 -1.0 -1.0]]
    for {set k 0} {$k < $par(nstep)} {incr k} {
        set intextension [format "%03i" $k]
        set firstorien$k [fcreate -np $par(np) -sw $par(sw) -type fid]
        set secondorien$k [fcreate -np $par(np) -sw $par(sw) -type fid]
    }
    for {set k 0} {$k < $par(nstep)} {incr k} {
        global g$k
        global p$k
        set intextension [format "%03i" $k]
        set rotordelay [expr {$k/$par(nstep)}]
        for {set i 0} {$i < $numberofspins} {incr i} {
          if {[lsearch -exact $namesmn iso[expr 1+$i]]>=0 &&
                    [lsearch -exact $namesmn span[expr 1+$i]]>=0} {
          for {set q 0} {$q < [llength $generator]} {incr q} {
            set simulationpar " "
            set iso "[subst \$mn(iso[expr 1+$i])]p"
            set span "[subst \$mn(span[expr 1+$i])]p"
            set grav [subst \$mn(grav[expr 1+$i])]
            set alpha [subst \$mn(alpha[expr 1+$i])]
            set beta [subst \$mn(beta[expr 1+$i])]
```

```
        set gamma [subst \$mn(gamma[expr 1+$i])]
        set int [subst \$mn(int[expr 1+$i])]
        set lb [subst \$mn(lb[expr 1+$i])]
        set gl [subst \$mn(gl[expr 1+$i])]
        set tmpstring [join [cs_sim2diagonal $iso $span $grav] " "]
        set tmpstring [subst "\ [cs_diagonal2par $tmpstring\]"]
        set aniso [lindex $tmpstring 1]
        set eta [lindex $tmpstring 2]
        set DClist [EulerAngleToDirectionCosine $alpha $beta $gamma]
        set SymDClist [Symmetry $DClist $generator $q]
        set EulerAngles [DirectionCosineToEulerAngles $SymDClist]
        set newalpha$i [lindex [lindex $EulerAngles 0] 0]
        set newbeta$i [lindex [lindex $EulerAngles 0] 1]
        set newgamma$i [lindex [lindex $EulerAngles 0] 2]
        lappend simulationpar [list shift_1_iso $iso]
        lappend simulationpar [list shift_1_aniso $aniso]
        lappend simulationpar [list shift_1_eta $eta]
        lappend simulationpar [list shift_1_alpha [subst $newalpha$i]]
        lappend simulationpar [list shift_1_beta [subst $newbeta$i]]
        lappend simulationpar [list shift_1_gamma [subst $newgamma$i]]
        set par(crystal_file) alphaXbetaY.cry
        set fq [fsimpson $simulationpar]
        set par(crystal_file) alphaXbetaY1.cry
        set eq [fsimpson $simulationpar]
        fadjustint $fq $int
        fadjustint $eq $int
#         fexpr $fq [list \$re*$int] [list \$im*$int]     (original command)
        faddlb $fq $lb $gl
        faddlb $eq $lb $gl
        fadd [subst $firstorien$k] $fq
        fadd [subst $secondorien$k] $eq
        funload $fq
        funload $eq
      }
     }
    }
    fft [subst \$firstorien$k]
    fft [subst \$secondorien$k]
    fextract [subst \$firstorien$k] [expr -0.5*$par(sw_exp)]
                                                [expr 0.5*$par(sw_exp)]
    fextract [subst \$secondorien$k] [expr -0.5*$par(sw_exp)]
                                                [expr 0.5*$par(sw_exp)]
    fnewnp [subst \$firstorien$k] $par(np_exp)
```

```
        fnewnp [subst \$secondorien$k] $par(np_exp)
        fset [subst \$firstorien$k] -sw [expr int($par(sw_exp))]
        fset [subst \$secondorien$k] -sw [expr int($par(sw_exp))]
        fsave [subst \$firstorien$k] interim-$intextension.spe
        fsave [subst \$secondorien$k] interim_diffcryfile-$intextension.spe
        set gchisq$k [chisquare [subst \$firstorien$k] [subst \$g$k]]
        set pchisq$k [chisquare [subst \$secondorien$k] [subst \$p$k]]
        set gnormlizedfactor$k [normfact [subst \$firstorien$k] [subst \$g$k]]
        set pnormlizedfactor$k [normfact [subst \$secondorien$k] [subst \$p$k]]
        set gRMSrow$k [expr {[subst \$gchisq$k]/[subst \$gnormlizedfactor$k]}]
        set pRMSrow$k [expr {[subst \$pchisq$k]/[subst \$pnormlizedfactor$k]}]
       set totalchisq [expr {$totalchisq+([subst \gchisq$k])+([subst \$pchisq$k])}]
        set totalnormfact [expr {$totalnormfact+([subst \$gnormlizedfactor$k])+
                                                  ([subst \$pnormlizedfactor$k])}]
        fzero [subst \$firstorien$k]
        fzero [subst \$secondorien$k]
    }
    set totalrms [expr {$totalchisq/$totalnormfact}]
    return $totalrms
  }

proc main {} {
    global par g p firstorien secondorien mn rotordelay
    for {set k 0} {$k < $par(nstep)} {incr k} {
          global g$k
          global p$k
          set intextension [format "%03i" $k]
          set g$k [fload "sim-parallel-${intextension}.spe"]
          set p$k [fload "sim-perpendicular-${intextension}.spe"]
          file delete $par(name).mlog
    }
```

C.2 Add-on to the Simpson Program

The following parts are modified in the program SIMPSON (version 2.0.0) [156, 157] for the simulation of single-crystal MAS NMR data.

C.2.1 χ^2 Calculation

In the following section, the "frms"-command in the *ftool.c* file of the simpson program is modified to calculate χ^2 and used in single-crystal MAS NMR.

```
#define PART_COMPLEX 0
#define PART_RE 1
#define PART_IM 2

void daddChiSquare(double2* vec, double2* vec2, int from, int to, int part, dou-
ble* sumrms)
{
        int i;
        double dre, dim;

        if (part == PART_COMPLEX) {
                for (i=from; i<=to; i++) {
                        dre=vec[i].re−vec2[i].re;
                        dim=vec[i].im−vec2[i].im;
                        *sumrms + = dre*dre+dim*dim;
                }
        } else if (part == PART_RE) {
                for (i=from; i<=to; i++) {
                        dre=vec[i].re−vec2[i].re;
                        *sumrms + = dre*dre;
                }
        } else if (part == PART_IM) {
                for (i=from; i<=to; i++) {
                        dim=vec[i].im−vec2[i].im;
                        *sumrms + = dim*dim;
                }
        }
}

int tclChiSquare(ClientData data, Tcl_Interp* interp, int argc, char *argv[ ])
{
    FD* f;
    int fidN, fidN2;
    int nvec;
    double2 *vec, *vec2;
    double v1, v2;
    int part;
    char **par, **par2, *range;
    int i, i1, i2, npar, npar2;
    double sumrms;

    if (argc < 3 || argc > 6)
     return TclError(interp,"Usage: chisquare <descr 1> <descr 2> ?−re | −im?
```

```
                                        ?{{from to} {from to} ..}?");

  if (Tcl_GetInt(interp,argv[1],&fidN) == TCL_ERROR)
   return TclError(interp,"chisquare: argument 1 must be integer
                                        <data set from>");

  if (fidN < 1 || fidN > nfd || fd[fidN] == NULL)
   return TclError(interp,"chisquare: data set %d was not previously
                                        loaded\n",fidN);

  if (Tcl_GetInt(interp,argv[2],&fidN2) == TCL_ERROR)
   return TclError(interp,"chisquare: argument 2 must be integer
                                        <data set to>");

  if (fidN2 < 1 || fidN2 > nfd || fd[fidN2] == NULL)
   return TclError(interp,"chisquare: data set %d was not previously
                                        loaded\n",fidN);

  if (! fsamesize(fd[fidN], fd[fidN2]))
   return TclError(interp,"chisquare: %s\n",ferrormsg);

  f=fd[fidN];
  vec = (double2*) f->data;
  nvec = f->np*(f->ni > 1 ? f->ni : 1);
  vec2 = (double2*) fd[fidN2]->data;

  part=PART_COMPLEX;
  range=NULL;
  for (i=3; i<argc; i++) {
     if (!strcmp(argv[i],"-re")) {
        part=PART_RE;
     } else if (!strcmp(argv[i],"-im")) {
        part=PART_IM;
     } else {
        range=argv[i];
     }
  }
 sumrms=0;
  if (range != NULL) {
     if (Tcl_SplitList(interp, range, &npar, &par) != TCL_OK)
        return TclError(interp,"chisquare: list is not formed correctly\n");

     for (i=0; i<npar; i++) {
```

```
            if (Tcl_SplitList(interp,par[i],&npar2,&par2) != TCL_OK)
               return TclError(interp,"chisquare: list element number %d is not
                                                        formed correctly\n",i+1);

            if (npar2 != 2)
               return TclError(interp,"chisquare: list element number %d must
                                    contain two values, not %d\n",i+1,npar2);

            if (Tcl_GetDouble(interp,par2[0],&v1) != TCL_OK)
               return TclError(interp,"chisquare: unable to convert '%s' to a value
                                       in list element number %d\n",par2[0],i+1);

            if (Tcl_GetDouble(interp,par2[1],&v2) != TCL_OK)
               return TclError(interp,"chisquare: unable to convert '%s' to a value
                                       in list element number %d\n",par2[1],i+1);

            if (v1 >= v2)
               return TclError(interp,"chisquare: value 2 must be larger than value
                                          1 in list element number %d\n",i+1);

            i1=FD_INDEX(f,v1);
            if (i1 < 1) i1=1; else if (i1 > nvec) i1=nvec;
               i2=FD_INDEX(f,v2);
            if (i2 < 1) i2=1; else if (i2 > nvec) i2=nvec;
            if (i1 < i2) {
               daddChiSquare(vec,vec2,i1,i2,part,&sumrms);
            }
            free(par2);
         }
         free(par);
      } else {
         daddChiSquare(vec,vec2,1,nvec,part,&sumrms);
      }
      TclSetResult(interp,"%g",1000.0*sumrms);
      return TCL_OK;
}
void tclcmd_ftools(Tcl_Interp* interp)
{
        Tcl_CreateCommand(interp,"chisquare", tclChiSquare,
                                 (ClientData)NULL,(Tcl_CmdDeleteProc*)NULL);
}
```

command

set chisqvalue [chisquare data1 data2] [-re | -im]

It returns the χ^2 value between the two data sets namely "data1" and "data2". One can choose complex, real, and imaginary part of the data set similar to "frms"-command.

C.2.2 Normalized Intensity Factor Calculation

The following add-on in the *ftool.c* file of the simpson program calculates the normalized intensity factor.

```
#define PART_COMPLEX 0
#define PART_RE 1
#define PART_IM 2

void daddNormFact(double2* vec, double2* vec2, int from, int to, int part, double* sumint)
{
      int i;
       double sre, sim;

       if (part == PART_COMPLEX) {
            for (i=from; i<=to; i++) {
                 sre=vec[i].re+vec2[i].re;
                 sim=vec[i].im+vec2[i].im;
                 *sumint + = sre*sre+sim*sim;
            }
       } else if (part == PART_RE) {
            for (i=from; i<=to; i++) {
                 sre=vec[i].re+vec2[i].re;
                 *sumint + = sre*sre;
            }
       } else if (part == PART_IM) {
            for (i=from; i<=to; i++) {
                 sim=vec[i].im+vec2[i].im;
                 *sumint += sim*sim;
            }
       }
}
int tclNormFact(ClientData data, Tcl_Interp* interp, int argc, char *argv[ ])
{
```

```
FD* f;
int fidN, fidN2;
int nvec;
double2 *vec, *vec2;
double v1, v2;
int part;
char **par, **par2, *range;
int i, i1, i2, npar, npar2;
double sumint;

if (argc < 3 || argc > 6)
   return TclError(interp,"Usage: normfact <descr 1> <descr 2> ?-re | -im?
                                                ?{{from to} {from to} ..}?");

if (Tcl_GetInt(interp,argv[1],&fidN) == TCL_ERROR)
   return TclError(interp,"normfact: argument 1 must be integer
                                                    <data set from>");

if (fidN < 1 || fidN > nfd || fd[fidN] == NULL)
   return TclError(interp,"normfact: data set %d was not previously
                                                        loaded\n",fidN);

if (Tcl_GetInt(interp,argv[2],&fidN2) == TCL_ERROR)
   return TclError(interp,"normfact: argument 2 must be integer
                                                        <data set to>");

if (fidN2 < 1 || fidN2 > nfd || fd[fidN2] == NULL)
   return TclError(interp,"normfact: data set %d was not previously
                                                        loaded\n",fidN);

if (!fsamesize(fd[fidN],fd[fidN2]))
   return TclError(interp,"normfact: %s\n",ferrormsg);

f=fd[fidN];
vec = (double2*) f− >data;
nvec = f− >np*(f− >ni > 1 ? f− >ni : 1);
vec2 = (double2*) fd[fidN2]− >data;

part=PART_COMPLEX;
range=NULL;
for (i=3; i<argc; i++) {
   if (!strcmp(argv[i],"-re")) {
      part=PART_RE;
```

```
    } else if (!strcmp(argv[i],"-im")) {
        part=PART_IM;
    } else {
        range=argv[i];
    }
}
sumint=0;
if (range != NULL) {
    if (Tcl_SplitList(interp, range, &npar, &par) != TCL_OK)
        return TclError(interp,"normfact: list is not formed correctly\n");
    for (i=0;i¡npar;i++) {
        if (Tcl_SplitList(interp, par[i], &npar2, &par2) != TCL_OK)
            return TclError(interp,"normfact: list element number %d is not
                                                    formed correctly\n",i+1);

        if (npar2 != 2)
            return TclError(interp,"normfact: list element number %d must
                                    contain two values, not %d\n",i+1,npar2);

        if (Tcl_GetDouble(interp,par2[0],&v1) != TCL_OK)
            return TclError(interp,"normfact: unable to convert '%s' to a value
                                    in list element number %d\n",par2[0],i+1);

        if (Tcl_GetDouble(interp,par2[1],&v2) != TCL_OK)
            return TclError(interp,"normfact: unable to convert '%s' to a value
                                    in list element number %d\n",par2[1],i+1);

        if (v1 >= v2)
            return TclError(interp,"normfact: value 2 must be larger than value
                                        1 in list element number %d\n",i+1);

        i1=FD_INDEX(f,v1);
        if (i1 < 1) i1=1; else if (i1 > nvec) i1=nvec;
            i2=FD_INDEX(f,v2);
        if (i2 < 1) i2=1; else if (i2 > nvec) i2=nvec;

        if (i1 < i2) {
            daddNormFact(vec, vec2, i1, i2, part, &sumint);
        }
        free(par2);
    }
    free(par);
} else {
```

```
        daddNormFact(vec, vec2, 1, nvec, part, &sumint);
    }
    TclSetResult(interp,"%g",sumint);
    return TCL_OK;
}

void tclcmd_ftools(Tcl_Interp* interp)
{
      Tcl_CreateCommand(interp,"normfact", tclNormFact,
                        (ClientData)NULL,(Tcl_CmdDeleteProc*)NULL);
}
```

command

set normalizedfactor [normfact data1 data2] [-re | -im]

It returns the normalized factor between the two data sets namely "data1" and "data2". One can choose complex, real and imaginary part of the data set similar to "frms"-command.

Normalized root-mean-square (RMS) deviation can be calculated by using the presented "chisquare" and "normfact"-commands.

C.2.3 Intensity Fitting

The following add-on in the *ftool.c* of the simpsson program is presented to simulate intensity of the experimental data.

```
int tclFAdjustInt(ClientData data, Tcl_Interp* interp, int argc, char *argv[ ])
{
    int fidN;
    double intensity;
    int i;
    FD *f;

    if (argc != 3 )
        return TclError(interp,"Usage: fadjustint <data set> <intensity>");

    if (Tcl_GetInt(interp, argv[1], &fidN) == TCL_ERROR)
        return TclError(interp,"fadjustint: argument 1 must be integer
                                                    <data set>");

    if (fidN < 1 || fidN > nfd || fd[fidN] == NULL)
        return TclError(interp,"fadjustint: data set %d was not previously
```

```
                                                    loaded\n",fidN);

    if (Tcl_GetDouble(interp, argv[2], &intensity) == TCL_ERROR)
        return TclError(interp,"fadjustint: argument 2 must be double
                                                    <intensity>");

    f=fd[fidN];
    if (f->ni > 1) {
        return TclError(interp,"Sorry, fadjustint currently takes only 1D data");
    } else {
        for (i=1; i<=f->np; i++) {
            f->data[i].re=f->data[i].re*intensity;
            f->data[i].im=f->data[i].im*intensity;
        }
    }
    return TCL_OK;
}

void tclcmd_ftools(Tcl_Interp* interp)
{
      Tcl_CreateCommand(interp,"fadjustint", tclFAdjustInt,
                        (ClientData)NULL,(Tcl_CmdDeleteProc*)NULL);
}
```

command

fadjustint data1 intensity

The "intensity" factor in the above command applies to each data point in the complex data set "data1". The presented "fadjustint"-command is two times faster than original "fexpr"-command in the simpson program.

Appendix D

Mathematica Modules

The following mathematica modules are presented for the "Wolfram *Mathematica 7*" software.

D.1 Euler Angles and Rotation Matrix Calculation

Definitions of Euler angles and rotation Matrices follow the Rose convention and passive rotations [31]. This module calculates Euler Angles and the rotation matrix $\widetilde{\mathbf{R}}_{AD} = (\alpha_{AD}, \beta_{AD}, \gamma_{AD})$, defined in Fig 2.4 (see Chapter 2 section 2.5.1).

```
Needs["VectorAnalysis"]

eulermodule[xA_, yA_, zA_, xD_, yD_, zD_] :=
Module[{x1, y1, z1, x2, y2, z2, alpha, beta, gamma, n, rotZA, rotYB, rotZC,
rtilde, case},
 x1 = xA/Norm [xA]; y1 = yA/Norm [yA]; z1 = zA/Norm [zA];
 x2 = xD/Norm [xD]; y2 = yD/Norm [yD]; z2 = zD/Norm [zD];
 If [ x1.x2 == 1.0 && y1.y2 == 1.0 && z1.z2 == 1.0,
  (* case 1: coordinates systems are identical *)
  case = 100;
  alpha = 0;
  beta = 0;
  gamma = 0;
  ,
  ,(* case 2: coordinates systems are not identical *)
  ,case = 200;
  ,If [ Norm [CrossProduct[z1, z2]] == 0.0,
  ,(* case 2a: z1 and z2 are parallel *)
  ,case = 210;
```

```
,If [ z1.z2 == 1.0,
 ,(* case 2aa: z1 and z2 coincide *)
 ,case = 211;
 alpha = ArcTan [x1.x2, y1.x2];
 If [ alpha < 0,
     alpha = alpha + 2.0*Pi,
     alpha = alpha];
 beta = 0;
 gamma = 0,
 (ast case 2ab: z1 and z2 are antiparallel *)
 case = 212;
 alpha = 0.0;
 beta = Pi;
 If [ArcTan [-x1.x2, y1.x2] < 0,
     gamma = 2*Pi + ArcTan [-x1.x2, y1.x2],
     gamma = ArcTan [-x1.x2, y1.x2]];
];
,
(* case 2b: z1 and z2 are not parallel *)
case = 220;
n = CrossProduct [z1, z2]/ Norm [CrossProduct [z1, z2]];
(* n is the normalized node line vector *)
If [Norm [y1.n] == 1.0,
 (* case 2ba: n and y1 are parallel or antiparallel *)
 case = 221;
 If [y1.n == 1.0,
     (* case 2baa: n and y1 coincide *)
     case = 221.1;
     alpha = 0.0;
     beta = ArcCos [z1.z2];
     gamma = 0.0;
     ,
     (* case 2bab: n and y1 are antiparallel *)
     case = 221.2;
     alpha = Pi;
     beta = ArcCos [z1.z2];
     gamma = Pi;
 ];
 ,
 (* case 2bb: n and y1 are not parallel *)
 case = 222;
 n = CrossProduct[z1, z2]/Norm [CrossProduct[z1, z2]];
 (* no need to calculate n once again here *)
```

```
    If [(CrossProduct [y1, n]).z1 > 0,
        (* case 2bba *)
        case = 222.11;
        alpha = ArcCos [y1.n],
        case = 222.12;
        alpha = 2*Pi - ArcCos [y1.n]];
    beta = ArcCos [z1.z2];
    If[(CrossProduct [n, y2]).z2 > 0,
        (* case 2bbb *)
        case = 222.21;
        gamma = ArcCos [n.y2],
        case = 222.22;
        gamma = 2*Pi - ArcCos [n.y2]];
    ];
   ];
  ];
  (* Now that the angles have been determined, set up rtilde *)
  rotZA = {{Cos[alpha], -Sin[alpha], 0}, {Sin[alpha], Cos[alpha], 0}, {0, 0, 1}};
  (* MatrixForm [N [R_zA[α]]] *)
  rotYB = {{Cos[beta], 0, Sin[beta]}, {0, 1, 0}, {-Sin[beta], 0, Cos[beta]}};
  (* MatrixForm [N [R_yB[β]]] *)
  rotZC = {{Cos[gamma], -Sin[gamma], 0}, {Sin[gamma], Cos[gamma], 0}, {0, 0,
1}};
  (* MatrixForm [N [R_zC[γ]]] *)
  rtilde = rotZC^T.rotYB^T.rotZA^T;
  (* rtilde=[rotZC]^T.[rotYB]^T.[rotZA]^T ;*)
  Return[{alpha, beta, gamma, rtilde, case}]
]
```

Note: comments are higlighted in green color.

D.2 An Analytical Function for Single-Crystal

This module calculates the intensities and phases of the dispersive lineshape of the spinning sidebands of a single-crystal.

```
Needs["VectorAnalysis"]

CRfile = {{275.37}, {14.2941}, {1.0}};
SCSSmodule [δxxp_, δyyp_, δzzp_, γ_, H0_, ωr_, α0_, n1_, αcr_, βcr_, γcr_, αpc_,
βpc_, γpc_] :=
Module [{rγpc, rβpc, rαpc, rγcr, rβcr, rαcr, δp, rpc, δc, rcr, δr, p, a, κxxr, y,
```

```
κyyr, κxyr, κxzr, κyzr, d, θ, f},
  rγpc = {{Cos[γpc], Sin[γpc], 0}, {-Sin[γpc], Cos[γpc], 0}, {0, 0, 1}};
  rβpc = {{Cos[βpc], 0, -Sin[βpc]}, {0, 1, 0}, {Sin[βpc], 0, Cos[βpc]}};
  rαpc = {{Cos[αpc], Sin[αpc], 0}, {-Sin[αpc], Cos[αpc], 0}, {0, 0, 1}};
  rpc = rγpc . rβpc . rαpc;
  δp = {{δxxp, 0, 0}, {0, δyyp, 0}, {0, 0, δzzp}};
  δc = rpc . δp . Inverse[rpc];
  rγcr = {{Cos[γcr], Sin[γcr], 0}, {-Sin[γcr], Cos[γcr], 0}, {0, 0, 1}};
  rβcr = {{Cos[βcr], 0, -Sin[βcr]}, {0, 1, 0}, {Sin[βcr], 0, Cos[βcr]}};
  rαcr = {{Cos[αcr], Sin[αcr], 0}, {-Sin[αcr], Cos[αcr], 0}, {0, 0, 1}};
  rcr = rγcr . rβcr . rαcr;
  δr = rcr . δc . Inverse[rcr];
  κxxr = (-γ*H0)* (1.0/(2.0* ωr))*(2.0/3.0)*(δr[[1, 1]]/2.0);
  κyyr = (-γ*H0)* (1.0/(2.0* ωr))*(2.0/3.0)*(δr[[2, 2]]/2.0);
  κxyr = (-γ*H0)* (1.0/(2.0* ωr))*(2.0/3.0)*(δr[[1, 2]]);
  κxzr = (-γ*H0)* (1.0/ωr)*((2.0*√2)/3.0)*(δr[[1, 3]]);
  κyzr = (-γ*H0)* (1.0/ωr)*((2.0*√2)/3.0)*(δr[[2, 3]]);
  p = (-κxxr*Sin [(2*α0)]) + (κyyr*Sin [(2*α0)]) + (κxyr*Cos [(2*α0)]) -
                                                    (κxzr*Sin [α0]) + (κyzr*Cos [α0]);
  a = Exp[(I * p)];
  d = NIntegrate [Exp[I*((α0 - θ)* n1 + (κxxr * Sin[(2 * θ)]) -
                                        (κyyr * Sin[(2 * θ)]) - (κxyr * Cos[(2 * θ)]) +
                                        (κxzr * Sin[θ]) - (κyzr * Cos[θ]))], {θ, 0, 2π}];
  f = a * (1.0/(2.0 *π )) * d;
  Return[f]
]

filehandle = OpenWrite["SC_alanine_20_step.out"]
δxxp = -62.66582017560001 * 10^-6;
δyyp = -8.066289824399998 * 10^-6;
δzzp = 70.73211 * 10^-6;
γ = 6.728284 * 10^7;
H0 = 11.7467;
ωr = 2.0 *π * 1500.0;
(*α0=(π/180.0) * 360.0;*)
alpha0 = 20.0 (* angle increment *)
startalpha0 = 273.0
For [a = 0, a < 20, a++,
  α0 = (π/180.0) * (startalpha0 + ((360.0/alpha0) * a));
  Print [ "starting angle", " ", α0];
  eulerangle PC = {{348.785, 348.785, 168.785, 168.785},
                   {93.4101, 93.4101, 86.5899, 86.5899},
                   {127.324, 307.324, 52.6759, 232.676}};
```

```
  numbergammaangles = 1;
  For [N1 = -6, N1 ≤ 6, N1++,
   singlesideband = 0.0;
   For [u = 1, u ≤ Dimensions[CRfile][[2]], u++,
    αcr = (π/180.0) * CRfile[[1, u]];
    βcr = (π/180.0) * CRfile[[2, u]];
    (* Print [αcr,βcr];*)
    weightingfactor = CRfile[[3, u]]/numbergammaangles;
    For [k = 1, k ≤ numbergammaangles, k++,
     γcr = k * 22.1021 * π/180.0;
     (* Print [γcr];*)
     For [m = 1, m ≤ Dimensions[euleranglePC][[2]], m++,
      αpc = (π/180.0) * euleranglePC[[1, m]];
      βpc = (π/180.0) * euleranglePC[[2, m]];
      γpc = (π/180.0) * euleranglePC[[3, m]];
      (* Print [αcr]; Print [βcr]; Print [γcr]; *)
      (* Print [αpc]; Print [βpc]; Print [γpc]; *)
      singlesideband = SCSSmodule [δxxp, δyyp, δzzp, γ, H0, ωr, α0, N1, αcr,
                    βcr, γcr, αpc, βpc, γpc] * weightingfactor + singlesideband;
     ];
    ];
   ];
   WriteString [filehandle, α0 , " ", N1, " ", Abs[singlesideband], " ",
                                                Arg[singlesideband], "\n"];
   Print [α0, " ", N1, " ", singlesideband, " ", Abs[singlesideband], " ",
                        Arg[singlesideband], " ", Arg[singlesideband]/π* 180.0];
  ];
 ];
Close [filehandle]
```

Appendix E

Pulse Programs

E.1 Rotorsynchronized Phase Corrected Spin-Echo Sequence

```
;2D sequence
;d7 kill comb delay
;p7 pi/2 kill pulse
;d1 cycle delay
;P1 pi/2 pulse
;p2 pi pulse
;l7 kill loop
;pl2 decoupling H
;d6 rotor period
;d5 is a delay which helps to correct baseline phc1
#include <Avance.incl>
define delay roto
"roto=d6-p1/2.0-p2/2.0"


 1  ze
 2  20m                          pl7:f1
    10u                                  pl2:f2
 3  d7
                                 (p7 ph3):f1              ;saturation
    lo to 3 times l7
    d1                           pl1:f1
    1u                           trigpe4
    d0
    1u                                   cpds2:f2
                                 (p1 ph1):f1
    roto
```

```
                                        (p2 ph2):f1
    d5
    go=2 ph31 ph30:r finally do:f2
    10m wr #0 if #0 id0 ze
    lo to 2 times td1                                   ;repeat td1 times

exit
ph1= 1 2 3 0
ph2= {0 0 0 0}∧1∧2∧3
ph3= 0
ph30= 0
ph31= {1 0 3 2}∧2
```

E.2 Rotorsynchronized Phase Corrected Cross-Polarization with Spin-Echo Sequence

```
;2D sequence, 32 step phase cycle
;d7 kill comb delay
;p7 Pi/2 kill pulse
;d8 kill comb delay
;d6 rotor period
;d1 cycle delay
;p2 Pi/2 Pulse
;p3 Pi/2 Pulse
;p4 Pi/2 Pulse
;p5 Pi Pulse
;d5 is a delay which helps to correct baseline phc1
;pl1 CP
;pl2 hard pi/2
;pl3 CP ramp
;p15 contact pulse
;pl7 kill pulse
;pl12 decoupling

#include <Avance.incl>
define delay rotohalf
"rotohalf=d6/2.0-p3-p4"
define delay roto
"roto=d6-p4/2.0-p5/2.0"
```

```
1   ze
2   10u             pl1:f1
    10u                             pl7:f2
3   d7
                                    (p7 ph30):f2
    lo to 3 times l7
    d1                              pl2:f2
4   d8              pl4:f1
                    (p4 ph30):f1                        ;Pi/2 Pulse
    lo to 4 times l8
    1u              pl1:f1
    1u              trigpe4                             ;wait for trigger signal
                                    (p3 ph1):f2         ;proton 90 pulse
    0.1u                            pl3:f2
                    (p15 ph2):f1    (p15:spf0 ph10):f2  ;contact pulse
    0.1u            pl4:f1          pl12:f2
                    (p4 ph3):f1     (1u cpds2):f2
    rotohalf
    1u              trigpe4
    d0
                    (p4 ph4):f1                         ;Pi/2 Pulse
    roto
                    (p5 ph5):f1
    d5

    go=2 ph31 ph30:r    finally do:f2       ;related to decoupling power
    30m wr #0 if #0 id0 zd
    lo to 2 times td1                       ;repeat td1 times
exit
ph30= 0
ph1= 1 3                                                ;90 H pulse
ph2= {{0}*2}∧2                                          ;X spinlock
ph3= {{1}*4}∧2
ph4= {{0}*8}∧1∧2∧3
ph5= {{0}*32}∧1∧2∧3                                     ;180 pulse from Echo
ph10= 0                                                 ;H spinlock
ph31= {{{{{0}∧2}∧2}∧2}∧3∧2∧1}∧2∧0∧2                     ;receiver
```

E.3 Two Dimensional DEPTH-EXSY Sequence

```
;2D exchange
;Cog36(23,5,14,13,14,13,14;0)
;p1 hard pi/2
;p2 hard pi
;p4 hard pi/2
;pl7 kill pulse
;pl1 hard pi/2
;p7 kill pulse
;l7 kill loop
;d7 kill delay
;d2 mixing time
define loopcounter td1half
"td1half = td1/2"
#include <Avancesolids.incl>


 1  ze
 2  d7                    pl7:f1
                          p7 ph1
    lo to 2 times l7
    d1                                    ;repetition delay
    3u                    pl1:f1
    0.1u                  trigpl4
                          p1 ph1
    d0
                          p1 ph2
    d2
    0.1u                  trigpl4
                          p1 ph3          ;read pulse
                          p2 ph4
                          p2 ph5
                          p2 ph4
                          p2 ph5
    de
    STARTADC                              ;arm adc
    RESETPHASE                            ;reset reference phase for detection
    1u                    RGP_ADC_ON      ;open adc gate
    1u:f1 ph31
    1u                    REC_UNBLK       ;open preamp, receiver and adc
    1u                    DWELL_GEN       ;start dwell time generation
    aq
```

```
    1m                  ip1*23
    1m                  ip2*5
    1m                  ip3*14
    1m                  ip4*13
    1m                  ip5*14
    rcyc=2
    30m wr #0 if #0
    10m                 ze
    1m                  rp1
    1m                  rp2
    1m                  rp3
    1m                  rp4
    1m                  rp5
    1m                  ip1*9
    lo to 2 times 2
    1m                  id0
    1m                  rp1
    1m                  rp2
    1m                  rp3
    1m                  rp4
    1m                  rp5
    lo to 2 times td1half

exit
ph1= (36) {{0}*36}∧9∧18∧27
ph2= (36) {{18}*36}∧9∧18∧27
ph3= (36) {{9}*36}∧9∧18∧27
ph4= (36) {{0}*36}∧9∧18∧27
ph5= (36) {{18}*36}∧9∧18∧27
ph30= 0
ph31= {{0}*36}∧1∧2∧3
```

E.4 Two Dimensional DEPTH-SR6$_6^2$ Sequence

```
;C7
;homonuclear ZQ recoupling SR6_6^2
;Cog72(49,13,31,40,41,40,41,40;0)
;p1 hard pi/2
;p2 pi1/2 R6_6^2
;p3 pi3/2 R6_6^2
```

```
;p4 hard pi/2
;p5 hard pi
;l1 number of R elements
;pl7 kill pulse
;pl9 SR6^2_6
;pl1 hard pi/2
;p7 kill pulse
;l7 kill loop
;d7 kill delay
define loopcounter td1half
"td1half = td1/2"
#include <Avancesolids.incl>


 1  ze
 2  d7                  pl7:f1
                        p7 ph1
    lo to 2 times l7
    d1                                      ;repetition delay
    3u                  pl1:f1
                        p1 ph1
    d0
                        p1 ph2
    1u                  pl9:f1
 3                      p2 ph3^
                        p3 ph4^
    lo to 3 times l1
    1u                  pl1:f1
                        p1 ph5              ;read pulse
                        p5 ph6
                        p5 ph7
                        p5 ph6
                        p5 ph7
    de
    STARTADC                                ;arm adc
    RESETPHASE                              ;reset reference phase for detection
    1u                  RGP_ADC_ON          ;open adc gate
                        1u:f1 ph31
    1u                  REC_UNBLK           ;open preamp, receiver and adc
    1u                  DWELL_GEN           ;start dwell time generation
    aq
    1m                  ipp31 ipp5 ipp6 ipp7
    1m                  ip1*49
```

```
    1m                  ip2*13
    1m                  ip3*31
    1m                  ip4*31
    1m                  ip5*40
    1m                  ip6*41
    1m                  ip7*40
    1m                  rpp3
    1m                  rpp4
    rcycnp=2
    30m wr #0 if #0
    10m                 ze
    1m                  rp1
    1m                  rp2
    1m                  rp3
    1m                  rp4
    1m                  rp5
    1m                  rp6
    1m                  rp7
    1m                  ip1*18
    1m                  rpp31 rpp5 rpp6 rpp7
    lo to 2 times 2
    1m                  id0
    1m                  rp1
    lo to 2 times td1half

exit
ph1= (72) 0
ph2= (72) 36
ph3= (72) {{12 60}*3 {60 12}*3}∧24∧48
ph4= (72) {{48 24}*3 {24 48}*3}∧24∧48
ph5= (72) {{54}*72}∧18∧36∧54
ph6= (72) {{0}*72}∧18∧36∧54
ph7= (72) {{0}*72}∧18∧36∧54
ph30= 0
ph31= {{0}*72}∧1∧2∧3
```

E.5 Two Dimensional PRESTO-III Sequence

```
define delay tau1
define loopcounter rele1
```

```
define delay tau2
define loopcounter rele2
define loopcounter td1half
"td1half = td1*0.5"
"tau1 = p5 - p2"
"tau2 = p5 - p3"
"rele1 = l1/2-1"
"rele2 = l1/2-2"
;pl1 hard pulses
;pl7 kill power
;pl2 hard pi/2 pulse
;pl3 R-sequence
;pl12 decoupling power
;p1 hard pi/2 pulse
;p2 hard pi/2 pulse
;p3 hard pi/4 pulse p5>p2
;p4 hard pi pulse
;p5 R-element R18 1 7
;p10 hard pi/2 kill pulse
;l1 Relements
;l7, l8, d7, d8, p8, p7 regarding saturation comb, kill delay, and kill pulse
#include <Avancesolids.incl>


  1  ze
  2  1u                  reset:f1
                                          1u reset:f2
     10u                 pl1:f1
     10u                                  pl2:f2
  3  d7
                                          (p7 ph0):f2
     lo to 3 times l7
     d1
  4  d8
                         (p8 ph0):f1
     lo to 4 times l8
     10u                                  pl2:f2
                                          (p1 ph1):f2
     d0
                                          (p1 ph2):f2
     0.1u                                 pl3:f2
  5                                       (p5 ph10^):f2   ;R18 1 7 + 0°
                                          (p5 ph10^):f2
```

```
      lo to 5 times rele1
                                    (p5 ph10∧):f2
                        (tau1 p2 ph3):f1  (p5 ph10∧):f2
                        (p2 ph3):f1       (p5 ph11∧):f2   ;R18 1 7 + 180°
                                          (p5 ph11∧):f2
  6                                       (p5 ph11∧):f2
                                          (p5 ph11∧):f2
      lo to 6 times rele2
                                          (p5 ph11∧):f2
                        (tau2 p3 ph4):f1  (p5 ph11∧):f2
                        (p3 ph4 tau2):f1  (p5 ph12∧):f2   ;R18 1 7 + 90°
                                          (p5 ph12∧):f2
  7                                       (p5 ph12∧):f2
                                          (p5 ph12∧):f2
      lo to 7 times rele2
                                          (p5 ph12∧):f2
                        (tau1 p2 ph3):f1  (p5 ph12∧):f2
                        (p2 ph3 tau1):f1  (p5 ph13∧):f2   ;R18 1 7 + 270°
                                          (p5 ph13∧):f2
  8                                       (p5 ph13∧):f2
                                          (p5 ph13∧):f2
      lo to 8 times rele1
      0.1u                                cw:f2
      0.1u                                pl12:f2

      go=2 ph31 ph0:r finally do:f2                   ;do NS scans
      30m wr #0 if #0
1m ip1
1m zd
lo to 2 times 2
1m id0
1m rp1
1m zd
lo to 2 times td1half
exit

ph0= 0
ph1= 0 2                                              ;1st H pi/2 pulse
ph2= 0 0 2 2                                          ;2nd H pi/2 pulse
ph3= 0
ph4= 1
ph10= (36) {{7 29}*9} {{29 7}*9}
```

ph11= (36) {{25 11}*9} {{11 25}*9}
ph12= (36) {{16 2}*9} {{2 16}*9}
ph13= (36) {{34 20}*9} {{20 34}*9}
ph30= 0
ph31= {1 3}∧2

List of Figures

List of Tables

List of Symbols and Abbreviations

$\boldsymbol{\delta}$	chemical shift tensor
δ_{iso}	isotropic chemical shift
δ_{aniso}	chemical shift anisotropy parameter
η	asymmetry parameter of the chemical shift tensor
η_Q	quadrupole asymmetry parameter
γ	gyromagnetic ratio
ν	frequency
ω_{nut}	nutation frequency
ω_0	Larmor frequency
ω_r	sample spinning frequency
ω_{ref}	reference frequency
Ω_{BD}	set of three Euler angles α_{BD}, β_{BD}, and γ_{BD}
Ψ	wave function
$\hat{\rho}$	density operator
σ	chemical shielding
$\hat{\mu}$	magnetic moment
τ	time interval
b_{ij}	dipole-dipole coupling constant
$\mathbf{B}_0$	external magnetic field
C_Q	quadrupole coupling constant
$\hat{I}$	spin angular momentum
I	spin quantum number
J_{iso}	isotropic J-coupling
m	magnetic quantum number
$\mathbf{M}$	magnetization vector
$\hat{\mathcal{H}}$	Hamiltonian
$\mathbf{R}$	Euler rotation matrix
$\hat{R}$	rotation operator
T_1	longitudinal relaxation time
T_2	transverse relaxation time
1D	one dimensional

2D	two dimensional
2D-EXSY	two dimensional exchange spectroscopy
AZO or ZnO:Al	aluminum doped zinc oxide
CP	cross polarization
CRS or C	crystal frame
CS	chemical shift
CSA	chemical shift anisotropy tensor
CW	continuous wave
DD coupling	dipole-dipole coupling
DRFS	double resonance ^{1}H-^{19}F frequency splitter box
FID	free induction decay
FTO or SnO_2:F	fluorine doped tin oxide
EFG	electric field gradient
FT	Fourier transformation
HARDSHIP	heteronuclear recoupling with dephasing by strong homonuclear interactions of protons
HETCOR	heteronuclear correlation spectroscopy
ISTO	irreducible spherical tensor operator
LAB or L	laboratory frame
MAS	magic angle spinning
MOL or M	molecular frame
MQ	multiple quantum
MQMAS	multiple quantum magic angle spinning
NMR	nuclear magnetic resonance
qNMR	quantitative analysis by NMR
PRESTO	phase-shifted recoupling effects a smooth transfer of order
PAF or P	principal axis frame
REDOR	rotational echo double resonance
rf	radiofrequency
ROT or R	rotor frame
SOQE	second order quadrupolar effect
TCO	transparent conductive oxide
TPPM	two pulse phase modulation
TQMAS	triple quantum magic angle spinning

Bibliography

[1] Klinowski, J. *Annu. Rev. Mater. Sci.* **1988**, *18*, 189–218.

[2] Eckert, H. *Prog. Nucl. Magn. Reson. Spectrosc.* **1992**, *24*, 159–293.

[3] Medek, A.; Frydman, L. *J. Braz. Chem. Soc.* **1999**, *10*, 263–277.

[4] Brown, S. P.; Spiess, H. W. *Chem. Rev.* **2001**, *101*, 4125–4155.

[5] Ashbrook, S. E.; Duer, M. J. *Concepts Magn. Reson. A* **2006**, *28*, 183–248.

[6] Böhmer, R.; Jeffrey, K. R.; Vogel, M. *Prog. Nucl. Magn. Reson. Spectrosc.* **2007**, *50*, 87–174.

[7] Laws, D. D.; Bitter, H. M. L.; Jerschow, A. *Angew. Chem. Int. Ed.* **2002**, *41*, 3096–3129.

[8] Goldbourt, A.; Madhu, P. K. *Annu. Rep. NMR Spectrosc.* **2005**, *54*, 81–153.

[9] Mayer, C. *Prog. Nucl. Magn. Reson. Spectrosc.* **2002**, *40*, 307–366.

[10] Foces-Foces, C.; Echevarrìa, A.; Jagerovic, N.; Alkorta, I.; Elguero, J.; Langer, U.; Klein, O.; Minguet-Bonvehì, M.; Limbach, H. H. *J. Am. Chem. Soc.* **2001**, *123*, 7898–7906.

[11] Seyfartha, L.; Sehnerta, J.; El-Gamelb, N. E. A.; Miliusa, W.; Krokeb, E.; Breua, J.; Senker, J. *J. Mol. Struct.* **2008**, *889*, 217–228.

[12] Duer, M. J. *Solid-State NMR Spectroscopy: Principles and Applications.;* Blackwell Science, Malden, 2002.

[13] Duer, M. *Introduction to solid-state NMR spectroscopy;* Blackwell, 2004.

[14] Harris, R. K. *Nuclear magnetic resonance spectroscopy: a physicochemical view.;* Longman, 1986.

[15] Eckert, H. *Encyclopedia of Nuclear Magnetic Resonance* **1994**, pages 756–779.

[16] Eckert, H.; Elbers, S.; Epping, J. D.; Janssen, M.; Kalwei, M.; Strojek, W.; Voigt, U. *Top. Curr. Chem.* **2004**, *246*, 195–233.

[17] Nebel, H.; Neumann, M.; Mayer, C.; Epple, M. *Inorg. Chem.* **2008**, *47*, 7874–7879.

[18] Fang, X. W.; Mao, J. D.; Levin, E. M.; Schmidt-Rohr, K. *J. Am. Chem. Soc.* **2009**, *131*, 1426–1435.

[19] Maoa, J.; Fang, X.; Lan, Y.; Schimmelmann, A.; Mastalerz, M.; Xu, L.; Schmidt-Rohr, K. *Geochim. Cosmochim. Acta* **2010**, *74*, 2110–2127.

[20] Mayer, C. *Annu. Rep. NMR Spectrosc.* **2005**, *55*, 205–258.

[21] Mayer, C. *Prog. Colloid Polym. Sci.* **2006**, *133*, 22–29.

[22] Mayer, C. *NMR Characterization Techniques – Application to Nanoscaled Pharmaceutical Carriers.;* Wiley-VCH Verlag GmbH & Co., 2007.

[23] Tsuchida, J.; Schneider, J.; Rinke, M. T.; Eckert, H. *J. Phys. Chem. C* **2011**, *115*, 21927–21941.

[24] Fry, R.; Pantano, C. G.; Mueller, K. T. *Phys. Chem. Glasses* **2003**, *44*, 64–68.

[25] Karpukhina, N.; Law, R. V.; Hill, R. G. *Adv. Mater. Res.* **2008**, *39-40*, 25–30.

[26] Martineau, C.; Michaelis, V. K.; Schuller, S.; Kroeker, S. *Chem. Mater.* **2010**, *22*, 4896–4903.

[27] Feng, X.; Verdegem, P. J. E.; Lee, Y. K.; Sandström, D.; Edén, M.; Bovee-Geurts, P.; de Grip, W. J.; Lugtenburg, J.; de Groot, H. J. M.; Levitt, M. H. *J. Am. Chem. Soc.* **1997**, *119*, 6853–6857.

[28] Verhoeven, M. A.; Creemers, A. F. L.; Bovee-Geurts, P. H. M.; De Grip, W. J. Lugtenburg, J.; de Groot, H. J. M. *Biochemistry* **2001**, *40*, 3282–3288.

[29] Carravetta, M.; Zhao, X.; Johannessen, O. G.; Lai, W. C.; Verhoeven, M. A.; Bovee-Geurts, P. H. M.; Verdegem, P. J. E.; Kiihne, S.; Luthman, H.; de Groot, H. J. M.; de Grip, W. J.; Lugtenburg, J.; Levitt, M. H. *J. Am. Chem. Soc.* **2004**, *126*, 3948–3953.

[30] Linser, R.; Bardiaux, B.; Higman, V.; Fink, U.; Reif, B. *J. Am. Chem. Soc.* **2011**, *133*, 5905–5912.

[31] Schmidt-Rohr, K.; Spiess, H. W. *Multidimensional solid-state NMR and polymers;* Academic Press, 1999.

[32] Papon, A.; Saalwächter, K.; Schäler, K.; Guy, L.; Lequeux, F.; Montes, H. *Macromolecules* **2011**, *44*, 913–922.

[33] Rastogi, S.; Yao, Y.; Lippits, D. R.; Höhne, G. W. H.; Graf, R.; Spiess, H. W.; Lemstra, P. J. *Macromol. Rapid Commun.* **2009**, *30*, 826–839.

[34] Hansen, M. R.; Graf, R.; Sekharan, S.; Sebastiani, D. *J. Am. Chem. Soc.* **2009**, *131*, 5251–5256.

[35] Purcell, E. M.; Torrey, H. C.; Pound, R. V. *Phys. Rev.* **1946**, *69*, 37–38.

[36] Bloch, F.; Hansen, W. W.; Packard, M. *Phys. Rev.* **1946**, *69*, 127.

[37] Proctor, W. G.; Yu, F. C. *Phys. Rev.* **1950**, *77*, 717.

[38] Dickinson, W. C. *Phys. Rev.* **1950**, *77*, 736–737.

[39] Andrew, E.; Bradbury, A.; Eades, R. *Nat.* **1959**, *183*, 1802–1803.

[40] Lowe, I. *Phys. Rev. Lett.* **1959**, *2*, 285–287.

[41] Stejskal, E. O.; Schaefer, J.; Waugh, J. S. *J. Magn. Reson.* **1977**, *28*, 105–112.

[42] Goldbourt, A.; Madhu, P. K. *Monatshefte für Chemie* **2002**, *133*, 1497–1534.

[43] Hediger, S.; Meier, B. H.; Ernst, R. R. *Chem. Phys. Lett.* **1993**, *213*, 627–635.

[44] Hafner, S.; Demco, D. E. *Solid State Nucl. Magn. Reson.* **2002**, *22*, 247–274.

[45] Pines, A.; Gibby, M. G.; Waugh, J. S. *Chem. Phys. Lett.* **1972**, *15*, 373–376.

[46] Pines, A.; Gibby, M. G.; Waugh, J. S. *J. Chem. Phys.* **1973**, *59*, 569–590.

[47] Aliev, A. E.; Law, R. V. *Nucl. Magn. Reson.* **2003**, *32*, 238–291.

[48] Aliev, A. E.; Law, R. V. *Nucl. Magn. Reson.* **2006**, *35*, 234–312.

[49] Amoureux, J. P.; Pruski, M. *Molecular Physics* **2002**, *100*, 1595–1613.

[50] Dybowski, C.; Bai, S. *Anal. Chem.* **2000**, *72*, 1–7.

[51] Eckert, H. *Curr. Opin. Solid State Mater. Sci.* **1996**, *1*, 465–476.

[52] Fitzgerald, J. J.; DePaul, S. M. *ACS Symp. Ser.* **1999**, *717*, 2–133.

[53] Fyfe, C. A. *Solid State NMR for Chemists.;* C.F.C. Press, 1983.

[54] MacKenzie, K. J. D.; Smith, M. E. *Multinuclear solid state NMR of inorganic materials.*, Vol. 6; Pergamon, Oxford, 2002.

[55] Harbison, G. S.; Vogt, V.-D.; Spiess, H. W. *J. Chem. Phys.* **1987**, *86*, 1206–1218.

[56] Schmidt-Rohr, K.; Wilhelm, M.; Johansson, A.; Spiess, H. W. *Magn. Reson. in Chem.* **1993**, *31*, 352–356.

[57] Chmelka, B. F.; Schmidt-Rohr, K.; Spiess, H. W. *Macromolecules* **1993**, *26*, 2282–2296.

[58] Harbison, G. S.; Spiess, H. W. *Chem. Phys. Lett.* **1986**, *124*, 128–134.

[59] Wilhelm, M.; Féaux de Lacroix, M. S.; Titman, J. J.; Schmidt-Rohr, K.; Spiess, H. W. *Acta Polymer.* **1993**, *44*, 279–284.

[60] Tang, P.; Santos, R. A.; Harbison, G. S. *Adv. Magn. Reson.* **1989**, *13*, 225–255.

[61] Dohi, H.; Kimura, H.; Kotani, M.; Matsunaga, T.; Yamauchi, K.; Kaji, H.; Asakura, T. *Polym. J. (Tokyo, Jpn.)* **2007**, *39*, 502–503.

[62] Kimura, H.; Dohi, H.; Kotani, M.; Matsunaga, T.; Yamauchi, K.; Kaji, H.; Kurosu, H.; Asakura, T. *Polym. J. (Tokyo, Jpn.)* **2010**, *42*, 25–30.

[63] Zhou, S. Z.; Zhou, Y. X.; Graham, C. D. *J. Appl. Phys.* **1988**, *63*, 3534–3536.

[64] Walker, T.; Wirtk, S.; Schläfer, D.; Mattern, N.; Müller, K.; Handstein, A. *Mikrochim. Acta* **1997**, *125*, 355–360.

[65] Legrand, B. A.; Chateigner, D.; Perrier de la Bathie, R.; Tournier, R. *J. Magn. Magn. Mater.* **1997**, *173*, 20–28.

[66] Kim, J.; Chung, S. E.; Choi, S.; Lee, H.; Kim, J.; Kwon, S. *Nat. Mater.* **2011**, *10*, 747–752.

[67] Taira, T.; Akiyama, J.; Asai, S.; Hara, K. *USA Patent* **2011**, *#13,142,132.*

[68] Legrand, B. A.; Chateigner, D.; Perrier de la Bathie, R.; Tournier, R. *J. Alloys Compd.* **1998**, *275-277*, 660–664.

[69] Gent, A. N. *J. Polym. Sci., Part A* **1965**, *3*, 3787–3801.

[70] Alfrey, T. *Int. J. Polym. Mater.* **1979**, *7*, 83–92.

[71] Rao, I. J.; Rajagopal, K. R. *Int. J. Solids Struct.* **2001**, *38*, 1149–1167.

[72] Zhao, B.; Li, X.; Huang, Y.; Cong, Y.; Ma, Z.; Shao, C.; An, H.; Yan, T.; Li, L. *Macromolecules* **2009**, *42*, 1428–1432.

[73] Buckingham, A. D.; Malm, S. M. *Mol. Phys.* **1971**, *22*, 1127–1130.

[74] Widdifield, C. M.; Schurko, R. W. *Concepts Magn. Reson., Part A* **2009**, *34*, 91–123.

[75] Yamada, K.; Asanuma, M.; Honda, H.; Nemoto, T.; Yamazaki, T.; Hirota, H. *J. Mol. Struct.* **2007**, *843*, 45–56.

[76] Bryce, D. L.; Grishaev, A.; Bax, A. *J. Am. Chem. Soc.* **2005**, *127*, 7387–7396.

[77] Zhu, J.; Lau, J. Y. C.; Wu, G. *J. Phys. Chem. B* **2010**, *114*, 11681–11688.

[78] Lauterbur, P. C. *Phys. Rev. Lett.* **1958**, *1*, 343–344.

[79] Naito, A.; Ganapathy, S.; Akasaka, K.; McDowell, C. A. *J. Chem. Phys.* **1981**, *74*, 3190–3197.

[80] Janes, N.; Ganapathy, S.; Oldfield, E. *J. Magn. Reson.* **1983**, *54*, 111–121.

[81] Haberkorn, R. A.; Stark, R. E.; van Willigen, H.; Griffin, R. G. *J. Am. Chem. Soc.* **1981**, *103*, 2534–2539.

[82] Griffin, R. G.; Ellett Jr., J. D.; Mehring, M.; Bullitt, J. G.; Waugh, J. S. *J. Chem. Phys.* **1972**, *57*, 2147–2155.

[83] Kohler, S. J.; Ellett Jr., J. D.; Klein, M. P. *J. Chem. Phys.* **1976**, *64*, 4451–4458.

[84] Kohler, S. J.; Ellett Jr., J. D.; Klein, M. P. *J. Chem. Phys.* **1976**, *65*, 2922.

[85] van Calsteren, M.-R.; Birnbaum, G. I.; Smith, I. C. P. *J. Chem. Phys.* **1987**, *86*, 5405–5410.

[86] Herzfeld, J.; Griffin, R. G.; Haberkorn, R. A. *Biochemistry* **1978**, *17*, 2711–2718.

[87] Spiess, H. W.; Haas, H.; Hartmann, H. *J. Chem. Phys.* **1969**, *50*, 3057–3064.

[88] Lauterbur, P. C.; Burke, J. J. *J. Chem. Phys.* **1965**, *42*, 439–440.

[89] Pausak, S.; Pinest, A.; Waugh, J. S. *J. Chem. Phys.* **1973**, *59*, 591–595.

[90] Pines, A.; Chang, J. J.; Griffin, R. G. *J. Chem. Phys.* **1974**, *61*, 1021–1030.

[91] Pausak, S.; Tegenfeldt, J.; Waugh, J. S. *J. Chem. Phys.* **1974**, *61*, 1338–1344.

[92] Honkonen, R. S.; Doty, F. D.; Ellis, P. D. *J. Am. Chem. Soc.* **1983**, *105*, 4163–4168.

[93] Vosegaard, T.; Langer, V.; Daugaard, P.; Hald, E.; Bildsøe, H. *Rev. Sci. Instrum.* **1996**, *67*, 2130–2133.

[94] Griffin, R. G.; Powers, L.; Pershan, P. S. *Biochemistry* **1978**, *17*, 2718–2722.

[95] Kohler, S. J.; Klein, M. P. *Biochemistry* **1976**, *15*, 967–973.

[96] Kohler, S. J.; Klein, M. P. *Biochemistry* **1977**, *16*, 519–526.

[97] Murray, D. K.; Harrison, J. C.; Wallace, W. E. *J. Colloid Interface Sci.* **2005**, *288*, 166–170.

[98] Grossmann, G.; Scheller, D.; Malkina, O. L.; Malkin, V. G.; Zahn, G.; Schmitt, H.; Haeberlen, U. *Solid State Nucl. Magn. Reson.* **2000**, *17*, 22–38.

[99] Zhang, Y.; Oldfield, E. *J. Phys. Chem. B* **2004**, *108*, 19533–19540.

[100] Weber, J.; Schmedt auf der Günne, J. *Phys. Chem. Chem. Phys.* **2010**, *12*, 583–603.

[101] Kunath-Fandrei, G. H.; Kelbausakas, L.; Döring, D.; Rager, H.; Jäger, C. *Phys. Chem. Miner.* **1998**, *26*, 55–62.

[102] Radeglia, R. *Solid State Nucl. Magn. Reson.* **1995**, *4*, 317–321.

[103] Rizzo, V.; Pinciroli, V. *J. Pharm. Biomed. Anal.* **2005**, *38*, 851–857.

[104] Bekiroglu, S.; Myrberg, O.; Östman, K.; Ek, M.; Arvidsson, T.; Rundlöf, T.; Hakkarainen, B. *J. Pharm. Biomed. Anal.* **2008**, *47*, 958–961.

[105] Suryanarayanan, R.; Wiedmann, T. S. *Pharm. Res.* **1990**, *7*, 184–187.

[106] Nelson, B. N.; Shieber, L. J.; Barich, D. H.; Lubach, J. W.; Offerdahl, T. J.; Lewis, D. L.; Heinrich, J. P.; Munson, E. J. *Solid State Nucl. Magn. Reson.* **2006**, *29*, 204–213.

[107] Skibsted, J.; Rasmussen, S.; Herfort, D.; Jakobsen, H. *Cem. Concr. Comp.* **2003**, *25*, 823–829.

[108] Hilbig, H.; Kohler, F. H.; Schiel, P. *Cem. Concr. Res.* **2006**, *36*, 326–329.

[109] Schmedt auf der Günne, J.; Beck, J.; Hoffbauer, W.; Krieger-Beck, P. *Chem. Eur. J.* **2005**, *11*, 4429–4440.

[110] Harris, R. K.; Hodgkinson, P.; Larsson, T.; Muruganatham, A. *J. Pharm. Biomed. Anal.* **2005**, *38*, 858–864.

[111] Bugay, D. E. *Adv. Drug Deliv. Rev.* **2001**, *48*, 43–65.

[112] Harris, R. K. *Analyst* **1985**, *110*, 649–655.

[113] Sanchez, S.; Ziarelli, F.; Viel, S.; Delaurent, C.; Caldarelli, S. *J. Pharm. Biomed. Anal.* **2008**, *47*, 683–687.

[114] Ziarelli, F.; Viel, S.; Sanchez, S.; Cross, D.; Caldarelli, S. *J. Magn. Reson.* **2007**, *188*, 260–266.

[115] Yesinowski, J. P.; Eckert, H.; Rossman, G. R. *J. Am. Chem. Soc.* **1988**, *110*, 1367–1375.

[116] Nag, A.; Lotsch, B.; Schmedt auf der Günne, J.; Oeckler, O.; Schmidt, P. J.; Schnick, W. *Chem. Eur. J.* **2007**, *13*, 3512–3524.

[117] Draškovć, B.; Bogdanović, G.; Neelakantan, M.; Chamayou, A.-C.; Thalamuthu, S.; Avadhut, Y. S.; Schmedt auf der Günne, J.; Banerjee, S.; Janiak, C. *Crystal Growth & Design* **2010**, *10*, 1665–1676.

[118] Brunner, E.; Sternberg, U. *J. Prog. Nucl. Magn. Reson.* **1998**, *32*, 21–57.

[119] Wu, H.; Engelhard, M.; Wang, J.; Fisher, D.; Lin, Y. *J. Mater. Chem.* **2008**, *18*, 1779–1783.

[120] Baer, D.; Tratnyek, P.; Qiang, Y.; Amonette, J.; Linehan, J.; Sarathy, V.; Nurmi, J.; Wang, C.; Antony, J. *Environmental Applications of Nanomaterials: Synthesis, Sorbents and Sensors, World Scientific Publishing Co.* **2007**, pages 49–86.

[121] Nurmi, J.; Tratnyek, P.; Sarathy, V.; Baer, D.; Amonette, J.; Pecher, K.; Wang, C.; Linehan, J.; Matson, D.; Penn, R.; Driessen, M. *Environ. Sci. Technol.* **2005**, *39*, 1221–1230.

[122] Johnson, R.; Johnson, G.; Nurmi, J.; Tratnyek, P. *Environ. Sci. Techol.* **2009**, *43*, 5455–5460.

[123] Baer, D.; Gaspar, D.; Nachimuthu, P.; Techane, S.; Castner, D. *Anal. Bioanal. Chem.* **2010**, *396*, 983–1002.

[124] Baer, D.; Amonette, J.; Engelhard, M.; Gaspar, D.; Karakoti, A.; Kuchibhatla, S.; Nachimuthu, P.; Nurmi, J.; Qiang, Y.; Sarathy, V.; Seal, S.; Sharma, A.; Tratnyek, P.; Wang, C. *Surf. Interface Anal.* **2008**, *40*, 529–537.

[125] Grainger, D.; Castner, D. *Adv. Mater.* **2008**, *20*, 867–877.

[126] Grassian, V. *J. Phys. Chem. A* **2008**, *112*, 18303–18313.

[127] Schmidt-Rohr, K.; Rawal, A.; Fang, X. W. *J. Chem. Phys.* **2007**, *126*, 054701–p16.

[128] Gullion, T.; Schaefer, J. *J. Magn. Reson.* **1989**, *81*, 196–200.

[129] Chan, J. C. C.; Eckert, H. *J. Chem. Phys.* **2001**, *115*, 6095–6105.

[130] Chan, J. C. C. *Chem. Phys. Lett.* **2001**, *335*, 289–297.

[131] Brinkmann, A.; Schmedt auf der Günne, J.; Levitt, M. H. *J. Magn. Reson.* **2002**, *156*, 79–96.

[132] Jeener, J.; Meier, B. H.; Bachmann, P.; Ernst, R. R. *J. Chem. Phys.* **1979**, *71*, 4546–4553.

[133] Metz, G.; Wu, X.; Smith, S. O. *J. Magn. Reson. A* **1994**, *110*, 219–227.

[134] Hesse, M.; Meier, H.; Zeeh, B. *Spektroskopische Methoden in der organischen Chemie;* Thieme, 1991.

[135] Zhao, X.; Schmedt auf der Günne, J.; Levitt, M. H. *Solid State Nucl. Magn. Reson.* **2001**, *26*, 57–64.

[136] Levitt, M. H.; Madhu, P. K.; Hughes, C. E. *J. Magn. Reson.* **2002**, *155*, 300–306.

[137] Feike, M.; Demco, D. E.; Graf, R.; Gottwald, J.; Hafner, S.; Spiess, H. W. *J. Magn. Reson. A* **1996**, *122*, 214–221.

[138] Feike, M.; Graf, R.; Schnell, I.; Jäger, C.; Spiess, H. W. *J. Am. Chem. Soc.* **1996**, *118*, 9631–9634.

[139] Graf, R.; Demco, D. E.; Gottwald, J.; Hafner, S.; Spiess, H. W. *J. Chem. Phys.* **1997**, *106*, 885–895.

[140] Amoureux, J. P.; Fernandez, C. *J. Magn. Reson. Ser. A* **1996**, *123*, 116–118.

[141] Seth, A.; van Ooij, W. J.; Puomi, P.; Yin, Z.; Ashirgade, A.; Bafna, S.; Shivane, C. *Prog. Org. Coat.* **2007**, *58*, 136–145.

[142] Mostashari, S. M.; Darsaraei, A. *Int. J. Chem.* **2005**, *15*, 89–93.

[143] Tagiyev, D. B.; Aliyev, A. M.; Mamedov, N. D.; Fatullayeva, S. *Surf. Sci. Catal. A* **2004**, *154*, 1049–1055.

[144] Milutinovic-Nikolic, A. D.; Medic, V. B.; Vukovic, Z. M. *Dent. Mater.* **2007**, *23*, 674–678.

[145] Day, R. M.; Boccaccini, A. R. *J. Biomed. Mater. Res. A* **2005**, *73*, 73–79.

[146] Smith, A. L. *J. Electrochem. Soc.* **1951**, *98*, 363–368.

[147] Wang, J.; Wang, S.; Su, Q. *J. Mater. Chem.* **2004**, *14*, 2569–2574.

[148] Granqvist, C. G.; Hultaker, A. *Thin Solid Films* **2002**, *411*, 1–5.

[149] Ginley, D. S.; Bright, C. *MRS Bull.* **2000**, *25*, 15–18.

[150] Lewis, B. G.; Paine, D. C. *MRS Bull.* **2000**, *25*, 22–27.

[151] Minami, T. *Semicond. Sci. Technol.* **2005**, *20*, S35–S44.

[152] Gordon, G. R. *MRS Bull.* **2000**, *25*, 52–57.

[153] Sato, H.; Minami, T.; Miyata, T.; Takata, S.; Ishii, M. *Thin Solid Films* **1994**, *246*, 65–70.

[154] Lu, J. G.; Fujita, S.; Kawaharamura, T.; Nishinaka, H.; Kamada, Y.; Ohshima, T.; Ye, Z. Z.; Zeng, Y. J.; Zhang, Y. Z.; Zhu, L. P.; He, H. P.; Zhao, B. H. *J. Appl. Phys.* **2007**, *101*, 083705–p7.

[155] Brehm, J. U.; Winterer, M.; Hahn, H. J. *J. Appl. Phys.* **2006**, *100*, 064311–p9.

[156] Bak, M.; Rasmussen, J. T.; Nielsen, N. C. *J. Magn. Reson.* **2000**, *147*, 296–330.

[157] Vosegaard, T.; Malmendal, A.; Nielsen, N. C. *Monatshefte für Chemie* **2002**, *133*, 1555–1574.

[158] Levitt, M. H. *Spin Dynamics: Basics of Nuclear Magnetic Resonance;* Wiley, 2001.

[159] Abragam, A. *The principles of nuclear magnetism.;* Clarendon press, Oxford, 1961.

[160] Merzbacher, E. *Quantum Mechanics;* Wiley, New York, 1998.

[161] Gerstein, B. C.; Dybowski, C. R. *Transient Techniques in NMR of Solids, An Introduction to Theory and Practice.;* Academic Press, Inc. New York, 1985.

[162] Press, W.; Teukolsky, S.; Vetterling, W.; Flannery. *Numerical Recipies in C;* Cambridge University Press, New York, 1998.

[163] Fukushima, E.; Roeder, S. B. *Experimental Pulse Nuclear Magnetic Resonance: A Nuts and Bolts Approach.;* Perseus Press, Cambridge, Massachusetts, 1986.

[164] Bracewell, R. N. *The Fourier Transform & Its Applications.;* McGraw-Hill, NewYork, 1986.

[165] Smith, S. A.; Palke, W. E.; Gerig, J. T. *Concepts Magn. Reson.* **1992**, *4*, 107–144.

[166] Smith, S. A.; Palke, W. E.; Gerig, J. T. *Concepts Magn. Reson.* **1992**, *4*, 181–204.

[167] Varshalovich, D. A.; Moskalev, A. N.; Kheronskii, V. K. *Quantum Theory of Angular Momentum.;* World Scientific, Singapore, 1988.

[168] Levine, I. N. *Quantum Chemistry;* Prentice-Hall, 1991.

[169] Mehring, M.; Weberruß, V. A. *Object-oriented magnetic resonance;* Academic Press, 2001.

[170] Rose, M. E. *Elementary Theory of Angular Momentum.;* John Wiley & Sons, Inc., 1957.

[171] Spiess, H. W. *NMR Basic Principles and Progress* **1978**, *15*, 55–214.

[172] Mehring, M. *Principles of high resolution NMR in solids;* Springer, Berlin, 1983.

[173] Maricq, M. M.; Waugh, J. S. *J. Chem. Phys.* **1979**, *70*, 3300–3316.

[174] Brinkmann, A. *Dipolar recoupling in magic angle spinning nuclear magnetic resonance.* PhD thesis, Stockholm University, Sweden, **2001**.

[175] Levitt, M. H. *Encyclopedia of NMR* **2002**, *9*, 165–196.

[176] Slichter, C. *Principles of magnetic resonance;* Springer-verlage, Berlin, 1992.

[177] Haeberlen, U. *Advances in Magnetic Resonance; Suppl. 1.; Waugh, J. S. Ed.,High Resolution NMR in Solids.;* Academic Press: New York, 1976.

[178] Spiess, H. W. *In NMR Basic Principles and Progress.; Diehl, P. and Fluck, E. and Kosfeld, R. Eds.*, Vol. 15; Springer Verlag,Berlin, 1978.

[179] IUPAC. *Pure Appl. Chem.* **1972**, *29*, 627–628.

[180] IUPAC. *Pure Appl. Chem.* **1976**, *45*, 217–219.

[181] Harris, R. K.; Becker, E. D.; Cabral de Menezes, S. M.; Granger, P.; Hoffman, R. E.; Zilm, K. W. *Pure Appl. Chem.* **2008**, *80*, 59–84.

[182] Sedlmaier, S. J.; Döblinger, M.; Oeckler, O.; Weber, J.; Schmedt auf der Günne, J.; Schnick, W. *J. Am. Chem. Soc.* **2011**, *133*, 12069–12078.

[183] Ernst, R. R.; Bodenhausen, G.; Wokaun, A. *Principles of nuclear magnetic resonance in one and two dimensions*, International Series of Monographs on Chemistry; Oxford University Press, 1988.

[184] Lai, W.; McLean, N.; Gansmüller, A.; Verhoeven, M.; Antonioli, G.; Carravetta, M.; Duma, L.; Bovee-Geurts, P.; Johannessen, O.; de Groot, H.; Lugtenburg, J.; Emsley, L.; Brown, S.; Brown, R.; DeGrip, W.; Levitt, M. *J. Am. Chem. Soc.* **2006**, *128*, 3878–3879.

[185] Brown, S. P.; Pérez-Torralba, M.; Sanz, D.; Claramunt, R. M.; Emsley, L. *J. Am. Chem. Soc.* **2002**, *124*, 1152–1153.

[186] Vega, A. J. *Encyclopedia of Nuclear Magnetic Resonance* **1996**, *6*, 3869–3889.

[187] Man, P. P. *Encyclopedia of Analytical Chemistry* **2000**, pages 12224–12265.

[188] Man, P. P. *Encyclopedia of Nuclear Magnetic Resonance* **1996**, *6*, 3838–3848.

[189] Tycko, R. *Encyclopedia of Nuclear Magnetic Resonance* **1996**, *5*, 3425.

[190] Spiess, H. W. *Encyclopedia of Nuclear Magnetic Resonance* **1996**, *6*, 3668.

[191] Anet, F. A. L.; O'Leary, D. J. *Concepts Magn. Reson.* **1991**, *3*, 193–214.

[192] Klaus, E.; Sebald, A. *Magn. Reson. Chem.* **1994**, *32*, 679–690.

[193] Bhagavantam, S.; Venkatarayudu, T. *Theory of groups and its application to physical properties.;* Academic Press, New York, 1969.

[194] Weil, J. A.; Buch, T.; Clapp, J. E. *Adv. Magn. Reson.* **1973**, *6*, 183–257.

[195] Haeberlen, U. *High Resolution NMR in Solids* **1976**, pages 47–69.

[196] Olejniczak, E. T.; Vega, S.; Griffin, R. G. *J. Chem. Phys.* **1984**, *81*, 4804–4817.

[197] Levitt, M. H. *J. Magn. Reson.* **1989**, *82*, 427–433.

[198] Kreyszig, E. *Advanced Engineering Mathematics.*, Vol. 8^{th} Edition; John Wiley & Sons, Inc., 1999.

[199] Abramowitz, M.; Stegun, I. A. *Handbook of mathematical functions.;* Dover publications, Inc. New York, 1972.

[200] Arfken, G. B.; Weber, H. J. *Mathematical methods for physicists.*, Vol. 6^{th} Edition; Elsevier Academic Press, 2005.

[201] Hahn, E. *Phys. Rev.* **1950**, *80*, 580–594.

[202] Kolbert, A. C.; Raleigh, D. P.; Griffin, R. G. *J. Magn. Reson.* **1989**, *82*, 483–491.

[203] Hartmann, S. R.; Hahn, E. L. *Phys. Rev.* **1962**, *128*, 2042–2053.

[204] Filip, C.; Hafner, S.; Schnell, I.; Demco, D. E.; Spiess, H. W. *J. Chem. Phys.* **1999**, *110*, 423–440.

[205] Ernst, M. *J. Magn. Reson.* **2003**, *162*, 1–34.

[206] Ernst, M.; Samoson, A.; Meier, B. H. *Chem. Phys. Lett.* **2001**, *348*, 293–302.

[207] Bennett, A. E.; Rienstra, C. M.; Auger, M.; Lakshmi, K. V.; Griffin, R. G. *J. Chem. Phys.* **1995**, *103*, 6951–6958.

[208] Fung, B.; Khitrin, A. K.; Ermolaev, K. *J. Magn. Reson.* **2000**, *142*, 97–101.

[209] VanderHart, D. L.; Earl, W. L.; Garroway, A. N. *J. Magn. Reson.* **1981**, *44*, 361–401.

[210] Garroway, A. N.; VanderHart, D. L.; Earl, W. L. *Earl. Philos. Trans. R. Soc. London A* **1981**, *299*, 609.

[211] Ernst, M.; Zimmermann, H.; Meier, B. H. *Chem. Phys. Lett.* **2000**, *317*, 581–588.

[212] Dusold, S.; Sebald, A. *Annu. Rep. NMR Spectrosc.* **2000**, *41*, 185–264.

[213] Bennett, A. E.; Griffin, R. G.; Vega, S. *Solid-State NMR IV: Methods and Applications of Solid-State NMR* **1994**, *33*, 54.

[214] Tycko, R.; Dabbagh, G. *Chem. Phys. Lett.* **1990**, *173*, 461–465.

[215] Nielsen, N. C.; Bildsoe, H.; Jakobsen, H. J.; Levitt, M. H. *J. Chem. Phys.* **1994**, *101*, 1805–1812.

[216] Bennett, A. E.; Ok, J. H.; Griffin, R. G.; Vega, S. *J. Chem. Phys.* **1992**, *96*, 8624–8627.

[217] Carravetta, M.; Edén, M.; Zhao, X.; Brinkmann, A.; Levitt, M. H. *Chem. Phys. Lett.* **2000**, *321*, 205–215.

[218] Edén, M.; Levitt, M. H. *J. Chem. Phys.* **1999**, *111*, 1511–1519.

[219] Brinkmann, A.; Edén, M.; Levitt, M. H. *J. Chem. Phys.* **2000**, *112*, 8539–8554.

[220] Gullion, T. *Concepts Magn. Reson.* **1998**, *10*, 277–289.

[221] Gullion, T. *Magn. Reson. Rev.* **1997**, *17*, 83–131.

[222] Jaroniec, C. P.; Tounge, B. A.; Rienstra, C. M.; Herzfeld, J.; Griffin, R. G. *J. Magn. Reson.* **2000**, *146*, 132–139.

[223] Eckert, H. *Z. Phys. Chem.* **2010**, *224*, 1591–1653.

[224] Mueller, K. T.; Jarvie, T. P.; Aurentz, D. J.; Roberts, B. W. *Chem. Phys. Lett.* **1995**, *242*, 535–542.

[225] Garbow, J. R.; Gullion, T. *J. Magn. Reson.* **1991**, *95*, 442–445.

[226] Naito, A.; Nishimura, K.; Tuzi, S.; Saito, H. *Chem. Phys. Lett.* **1994**, *229*, 506–511.

[227] Bertmer, M.; Eckert, H. *Solid State Nucl. Magn. Reson.* **1999**, *15*, 139–152.

[228] Chan, J. C. C.; Eckert, H. *J. Magn. Reson.* **2000**, *147*, 170–178.

[229] Mueller, K. T. *J. Magn. Reson.* **1995**, *A 113*, 81–93.

[230] Hohwy, M.; Jakobsen, H. J.; Edén, M.; Levitt, M. H.; Nielsen, N. C. *J. Chem. Phys.* **1998**, *108*, 2686–2694.

[231] Lee, Y. K.; Kurur, N. D.; Helmle, M.; Johannessen, O. G.; Nielsen, N. C.; Levitt, M. H. *Chem. Phys. Lett.* **1995**, *242*, 304–309.

[232] Brinkmann, A.; Levitt, M. H. *J. Chem. Phys.* **2001**, *115*, 357–384.

[233] Goswami, M. *Development of methodologies in solid-state nuclear magnetic resonance and their applications in material chemistry.* PhD thesis, Tata Institute of Fundamental Research, India, **2010**.

[234] Frydman, L.; Harwood, J. S. *J. Am. Chem. Soc.* **1995**, *117*, 5367–5368.

[235] Amoureux, J. P.; Fernandez, C.; Frydman, L. *Chem. Phys. Lett.* **1996**, *259*, 347–355.

[236] Amoureux, J. P.; Fernandez, C.; Steuernagel, S. J. *J. Magn. Reson. A* **1996**, *123*, 116–118.

[237] Holzgrabe, U.; Deubner, R.; Schollmayer, C.; Waibel, B. *J. Pharm. Biomed. Anal.* **2005**, *38*, 806–812.

[238] Malz, F.; Jancke, H. *J. Pharm. Biomed. Anal.* **2005**, *38*, 813–823.

[239] Stephenson, G. A.; Forbes, R. A.; Reutzel-Edens, S. M. *Adv. Drug. Deliv. Rev.* **2001**, *48*, 67–90.

[240] Chopra, K. L.; Major, S.; Pandya, D. K. *Thin Solid Films* **1983**, *102*, 1–46.

[241] Ellmer, K.; Klein, A.; Rech, B. *Transparent Conductive Zinc Oxide*, Vol. 104; Springer Series in Materials Science, Berlin, 2008.

[242] Özgür, U.; Alivov, Y. I.; Liu, C.; Teke, A.; Reshchikov, M. A.; Doğan, S.; Avrutin, V.; Cho, S. J.; Morkoç, H. *J. Appl. Phys.* **2005**, *98*, 041301–p103.

[243] Gleiter, H. *Prog. Mater. Sci.* **1989**, *33*, 223–315.

[244] Siegel, R. W. *Physics of New Materials, edited by F. E. Fujita*, Vol. Chapter 4; Springer-Verlag, Berlin, 1994.

[245] Somorjai, G. A. *Pure & Appl. Chem.* **1978**, *50*, 963–969.

[246] Avadhut, Y. S. and. Weber, J.; Hammarberg, E.; Feldmann, C.; Schellenberg, I.; Pöttgen, R.; Schmedt auf der Günne, J. *Chem. Mater.* **2011**, *23*, 1526–1538.

[247] Heine, J.; Schmedt auf der Günne, J.; Dehnen, S. *J. Am. Chem. Soc.* **2011**, *133*, 10018–10021.

[248] Sedlmaier, S. J.; Döblinger, M.; Oeckler, O.; Weber, J.; Schmedt auf der Günne, J.; Schnick, W. *J. Am. Chem. Soc.* **2011**, *133*, 12069–12078.

[249] Haase, J.; Curro, N. J.; Slichter, C. P. *J. Magn. Reson.* **1998**, *135*, 273–279.

[250] Rossouw, J.and Jansen, E. *http://vipec.sourceforge.net/.* **2003**.